Magnetic Field Map for a Large TPC Prototype

Diplomarbeit

Institut für Experimentalphysik
Universität Hamburg

vorgelegt von

Christian Grefe

18. Juni 2008

Abstract

A new e^+e^- linear collider with an energy of up to 1000 GeV is currently being planned: the International Linear Collider (ILC). It will allow high precision measurements of the Higgs boson and physics beyond the Standard Model. In the Large Detector Concept (LDC) –which is one of the proposed detector concepts for the ILC– a Time Projection Chamber (TPC) is intended as the main tracking device.

Within the EUDET project a large TPC prototype is currently being built as an infrastructure to test different gas amplification and readout technologies. The prototype will be operated in a 1 T superconducting solenoid magnet –the PCMAG– at the DESY testbeam area. In order to reach the best possible track reconstruction the magnetic field has to be known very precisely throughout the TPC volume. The magnetic field of PCMAG has been measured in July 2007.

In this work the creation of a high precision field map from the measurements is presented. The magnet and modelling techniques for its magnetic field are described. A model of the magnet has been created as a best fit from the measurements and its limitations are investigated. The field map will be included in the reconstruction software for the TPC prototype.

Zusammenfassung

Ein neuer e^+e^--Linearbeschleuniger mit einer Schwerpunktsenergie von bis zu 1000 GeV befindet sich gerade in der Entwicklung: der International Linear Collider (ILC). Er wird sehr genaue Messungen des Higgs Bosons und von Physik jenseits des Standardmodells erlauben. Im Large Detector Concept (LDC) – einem der vorgeschlagenen Detektorkonzepte für den ILC – ist eine Zeit-Projektions-Kammer (TPC) als zentrale Spurkammer vorgesehen.

Im Rahmen des EUDET Projekts wird gerade ein großer TPC-Prototyp gebaut, der als Infrastruktur zum Test verschiedener Gasverstärkungs- und Auslesetechnologien genutzt werden wird. Der Prototyp wird in einem 1 T supraleitenden Solenoidmagneten – dem PCMAG – im DESY Teststrahlbereich betrieben werden. Um eine bestmögliche Spurrekonstruktion zu gewährleisten, muss das Magnetfeld im gesamten TPC-Volumen sehr genau bekannt sein. Das Magnetfeld wurde im Juli 2007 vermessen.

In dieser Arbeit wird die Erstellung einer sehr genauen Feldkarte aus den Messungen präsentiert. Der Magnet und Techniken um sein magnetisches Feld zu modellieren werden beschrieben. Es wurde ein Modell des Magneten anhand der gemessenen Daten erstellt und die Grenzen des Modells wurden untersucht. Die Feldkarte wird Teil der Rekonstruktionssoftware für den TPC Prototypen sein.

Contents

List of Figures

List of Tables

1 The International Linear Collider

1.1 Physics Motivation

1.1.1 The Standard Model of Particle Physics

Discoveries of the past century have led to a much deeper understanding of matter and the nature of the universe. It turned out that all experimental results could be reduced to the same principles. This is known today as the Standard Model of particle physics, which can in principle describe all known physics processes[1]. The great success of the Standard Model is not only based on its simple structure, but also on the fact that all its predictions have been verified until today.

In the Standard Model the basis of all matter are the fermions with a spin of 1/2 which are assumed to be elementary and thus pointlike particles without any structure. The fermions are the 6 quarks (u, d, c, s, t, b) and the 6 leptons (e^-, ν_e, μ^-, ν_μ, τ^-, ν_τ) and their respective antiparticles (see Table 1.1). They can be arranged in 3 families of quarks and leptons. The forces that connect the fermions are the electromagnetic, weak and strong forces, where the electromagnetic and weak forces can be described as one electroweak force. All these forces can be described with the same mathematical principles. They are all gauge theories and thus can be derived from simple symmetry assumptions which leave the action invariant. The mediators of these forces are bosons with a spin of 1: the photon (γ) for the electromagnetic force, the Z^0, W^+ and W^- for the weak force and 8 gluons (g) for the strong force.

The only particle of the Standard Model which has not been discovered yet is the Higgs boson with a spin of 0. The Higgs is giving mass to all particles in the Standard Model, which would be massless otherwise. Its mass is predicted to be between 115 GeV and about 160 GeV (see Figure 1.1), where the lower bound is based on exclusion from LEP (Large Electron Positron Collider) measurements and the upper bound is based on radiative corrections to the Z resonance peak.

The search for the Higgs is one of the main tasks of the Large Hadron Collider (LHC) which will start taking data in late 2008. With a center of mass energy of 14 TeV it will cover the complete energy scale of a possible Higgs. So if the standard model is correct the Higgs will be discovered at the LHC. The task for the ILC will then be the precise measurement of the Higgs mass.

Other important tasks for the ILC include the test of the SM and high precision measurements on SM parameters like the top mass or the running couplings for the different forces.

---

[1] Except gravitational effects, which are described by Einstein's theory of general relativity. These effects only become important at macroscopic scales.

Table 1.1: Particles and their masses in the Standard Model.

	generation			charge
	I	II	III	
quarks	**up**	**charm**	**top**	$2/3$
	($\sim 3\,\mathrm{MeV}$)	($\sim 1.2\,\mathrm{GeV}$)	($\sim 178\,\mathrm{GeV}$)	
	down	**strange**	**bottom**	$-1/3$
	($\sim 6\,\mathrm{MeV}$)	($\sim 0.1\,\mathrm{GeV}$)	($\sim 4.3\,\mathrm{GeV}$)	
leptons	electron (e^-)	muon (μ^-)	tau (τ^-)	-1
	($0.5110\,\mathrm{MeV}$)	($105.66\,\mathrm{MeV}$)	($1.777\,\mathrm{GeV}$)	
	e-neutrino (ν_e)	μ-neutrino (ν_μ)	τ-neutrino (ν_τ)	0
	($<3\,\mathrm{eV}$)	($<0.19\,\mathrm{MeV}$)	($<18\,\mathrm{MeV}$)	

1.1.2 Beyond the Standard Model

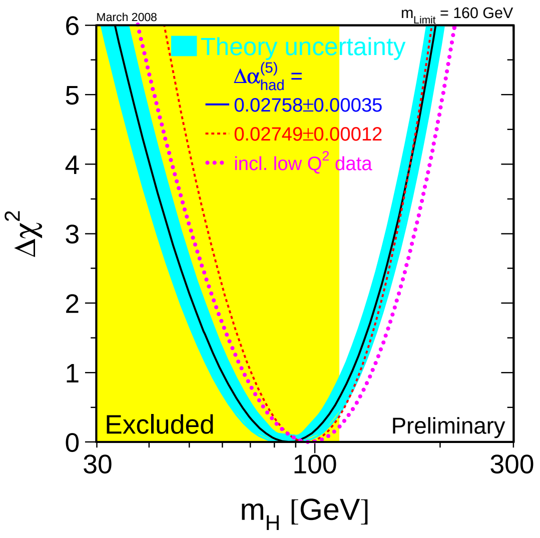

Figure 1.1: Constraints on the Standard Model Higgs mass from LEP experiments. Figure taken from [8].

Although the Standard Model is very successfull there are still some open questions and there is always room for additions to the model.

One prominent addition is supersymmetry (SUSY) (see for example [27]), which postulates a symmetry between bosons and fermions –the R-parity– and adds supersymmetric partners for all particles (so called sparticles). These sparticles would share all attributes of their Standard Model partners except for the spin and the mass. A higher mass is needed to explain the lack of observations of sparticles until today and has to be realized through a SUSY breaking mechanism. SUSY is able to solve three of the biggest problems of the Standard Model.

The main problem of the Standard Model is the hierarchy problem of the Higgs mass. The Higgs mass diverges quadratically due to radiative corrections from fermion loops. This requires an extreme fine tuning of parameters in order to prevent such divergence. In a SUSY model this problem would be non-existent, since the quadratic divergence due to fermions is canceled by their SUSY partners.

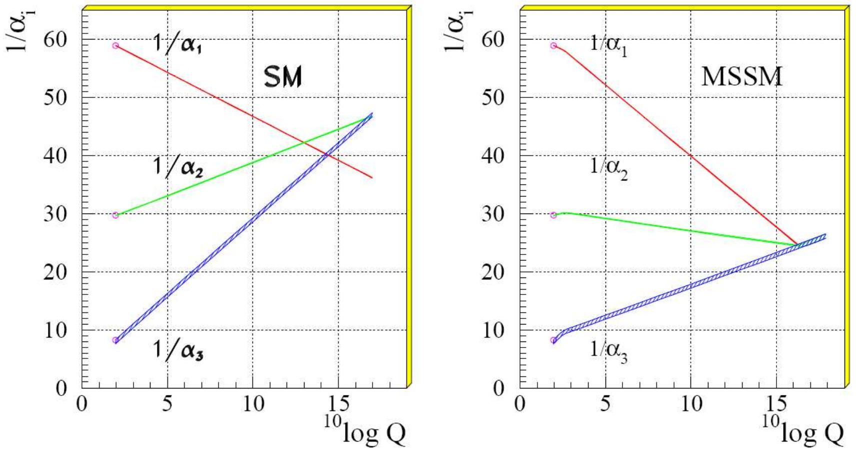

Figure 1.2: Evolution of the inverse of the three coupling constants in the Standard Model (left) and in the minimal supersymmetric extension of the Standard Model (MSSM)(right). Figure taken from [24].

Another one is the Grand Unification Theory (GUT) which aims at unifying the electroweak and strong forces to a single force. But this would require the running coupling constants of the three interactions to become one universal value at the GUT scale of about 10^{16} GeV. Extrapolation towards higher energies using the Standard model will not produce an universal value, but a SUSY model would produce such a value due to the extended particle content at the Terrascale (Figure 1.2).

The third problem comes from cosmological observations, which indicate that only 4% of our universe can be described as baryonic matter which obeys the Standard Model. 20% is dark matter, which only interacts gravitationally. Indirect evidence for this invisible mass are rotation curves of galaxies or the strength of gravitational lenses (see for example [14]). The missing 76% is dark energy (Λ) and has no gravitational effect due to its perfectly homogeneous distribution in the universe. The dark energy only contributes to the energy density (Ω) of the universe and its evidence comes from cosmic microwave background (CMB) and supernova (SN) observations. The combination of these observations favors a flat universe ($\Omega = 1$). The energy density from the observed baryonic and dark matter (Ω_M) is far to low to produce a flat universe (see Figure 1.3). In a SUSY model at least the dark matter could be explained as the lightest supersymmetric particle (LSP). The LSP is stable if R-parity is imposed. Only weak elastic scatterings or gravitational interaction are allowed with Standard Model matter.

All these problems make SUSY one of the favorite additions to the Standard Model and also one of the main discovery goals for LHC and ILC. Other possible discoveries could be large or compactified extra dimensions.

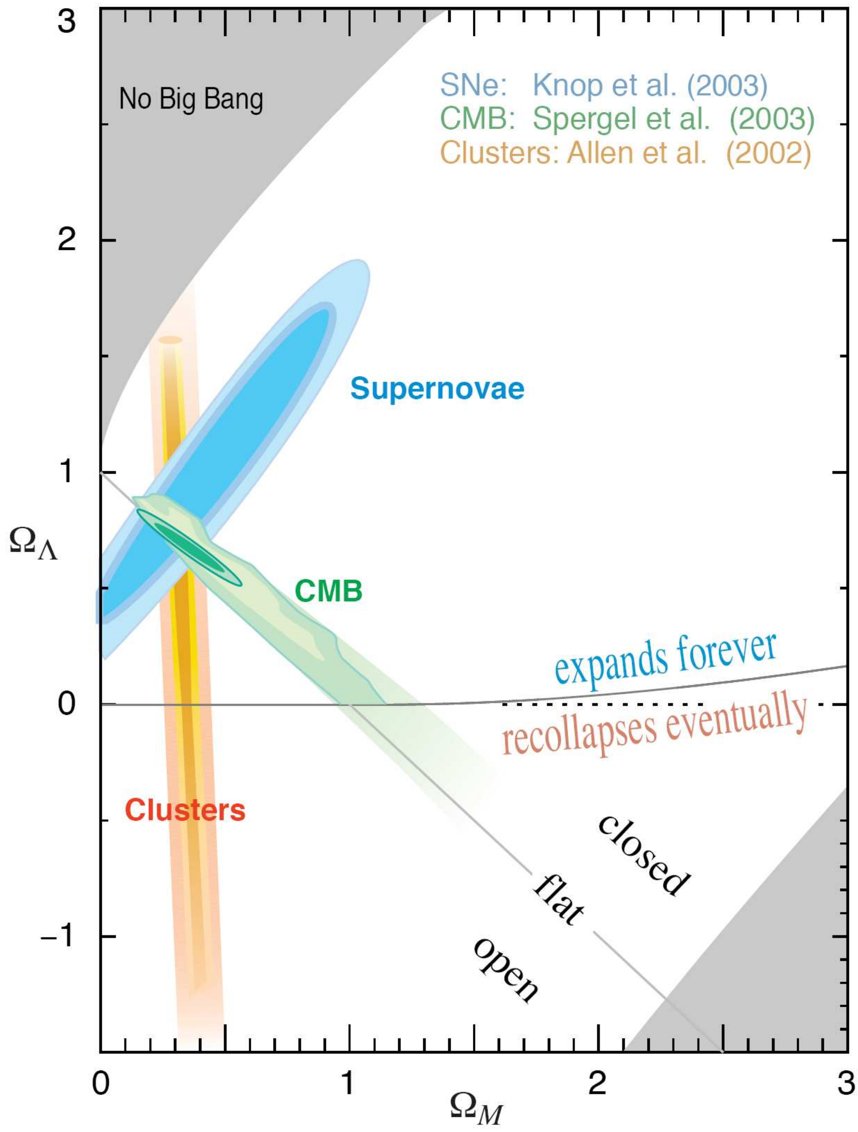

Figure 1.3: Preferred region in the Ω_M-Ω_Λ plane from complementary cosmological observations. Figure taken from [9].

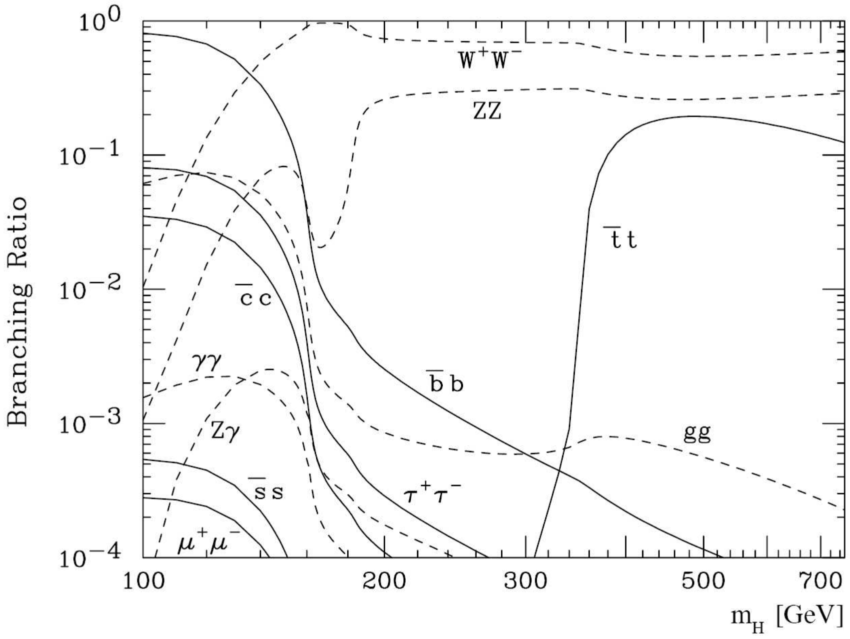

Figure 1.4: Branching ratio of the decay modes of the Standard Model Higgs. Figure taken from [18].

1.1.3 Requirements for the ILC

The LHC –which is about to start taking data– is a pp ring collider with a circumference of 27 km and a center of mass energy of 14 TeV. It will be able to discover the Higgs, SUSY or any other new physics scenarios in an unprecedented energy range. This high energy comes at the cost of precision, because of the proton structure which implies a not well defined inital state of the colliding particles. A pp collision also produces a huge QCD background. This makes a lepton collider necassary for high precision measurements.

The energy loss due to synchroton radiation during one cycle in a ring collider is given by

$$E_{\text{synchroton}} = \frac{1}{R}\left(\frac{E}{m}\right)^4, \tag{1.1}$$

where R is the radius, m is the particle mass and E the particle energy. Since electrons are about 2000 times lighter than protons, their energy loss is much higher in a ring collider. This excludes the option of a ring collider for the required center of mass energy and a linear collider is needed.

The International Linear Collider (ILC) is the concept for an e^+e^- linear collider with a center of mass energy of 500 GeV and a peak luminosity of $2 \times 10^{34}\,\text{cm}^{-2}\text{s}^{-1}$. A possible option of upgrading it to a center of mass energy of 1 TeV is being considered. Other possible options for the ILC include polarized beams as well as running as an e^-e^-, e^+e^+ or $\gamma\gamma$ collider. The project is currently still in the design phase and a final design is scheduled for 2011. Its necessity is to provide complemetary high precision measurements to the LHC measurements.

The physics processes at the ILC [20] push the requirements for the detector to an unprecedented level. Higgs or SUSY processes usually involve heavy quarks (t, b, c) due to their mass (see Figure 1.4). The low lifetime of heavy quarks requires an excellent vertex detection and the unambiguous identification of the different decay channels requires a very good jet energy resolution ($\Delta E_{\text{jet}}/E = 30\%/\sqrt{E}$), which is needed for the "particle flow" concept (see below). This concept is the basis of the different possible detector designs. The need of identifying missing energy as in SUSY processes also requires a nearly hermetic detector design.

1.2 Accelerator

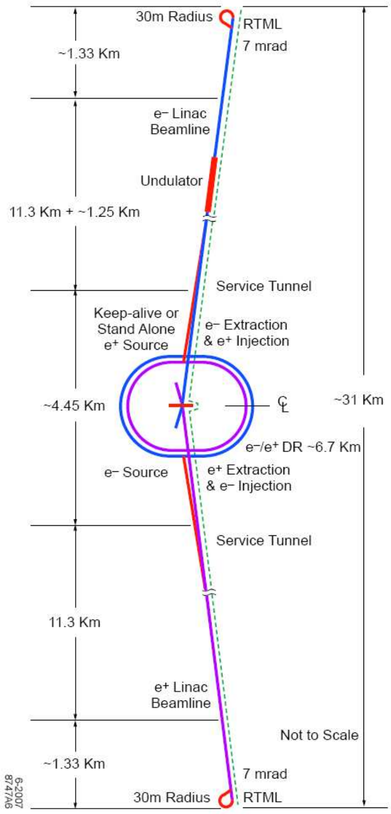

Figure 1.5: Schematic layout of the ILC for a center of mass energy of 500 GeV. Figure taken from [16].

The total length of the ILC will be about 31 km and the layout can be seen in Figure 1.5. It mainly consists of two linear accelerators (linac) of 11 km length each [28]. The 1.3 GHz superconducting radio frequency (SCRF) cavities used for the acceleration of the electrons and positrons are based on the cavities designed for TESLA [17] and they will operate at an average gradient of 31.5 MV/m.

The positron source consists of an electron beam which is used to produce a high energy photon beam in an undulator. After that the photon beam hits a metal target and produces positrons which are then captured and accelerated.

Both, the electrons and the positrons are pre accelerated to 5 GeV and then stored in two damping rings from where they are extracted and delivered to the main linacs.

The main linacs accelerate the beams to up to 500 GeV in the central interaction region where the two beams collide under a small crossing angle of 14 mrad. The crossing angle requires additional magnets in the interaction region to suppress the machine induced background for the detector. A Detector Integrated Dipole (DID) is used to perturb the detector solenoid field, such that the field points towards the outgoing beam (a DID pointing towards the outgoing beam is called anti-DID for historical reasons).

The beam will not be delivered as a continuous beam. Instead it will consist of pulses with a rate of 5 Hz. Each pulse will contain 2625 bunches with about 2×10^{10} particles per bunch. Every bunch will have a length of about $300\,\mu$m and the time between two successive bunches will be 369 ns. Note that these parameters might still change during the design process.

1.3 Detector

The interaction region of the ILC will be covered with an omni purpose detector which will be exchangeable with a second detector for redundant measurements and reduction of down time due to detector maintenance ("push-pull"). Currently several design concepts for the ILC detector are being considered [11].

- The Silicon Detector (SiD) Concept
- The Large Detector Concept (LDC)
- The GLD Concept
- The 4^{th} Concept Detector

All these are different approaches to achieve the requirements for a high precision machine like the ILC. These requirements include high jet resolution and jet mass resolution, excellent electron and muon identification and very good vertex detection. They all share a nearly hermetic tracking system and the "particle flow" concept. This concept aims at identifying every particle on its path through the different detector components. The charged particles are identified in the inner tracker and every hit can be identified with the corresponding hits in the calorimeter system. A high granularity calorimeters allows then the identification of neutral particles by excluding the hits from the charged particles. From these neutral hits the photons are identified in the electromagnetic calorimeter (ECAL) while the neutral hadrons are detected in the hadronic calorimeter (HCAL). Therefore, an identification of nearly every particle is achieved. This is important for processes like SUSY decays that include missing energy.

Currently the LDC and GLD are being merged because they share a lot of their main features. As an example the LDC will be described in more detail since the large TPC prototype is the prototype of the LDC inner tracker.

1.3.1 The Large Detector Concept

The LDC can be seen in Figure 1.6. It will have a height of about 14 m and a length of 20 m and it will feature a total of 10^9 readout channels. The different subsystems are arranged as in most collider experiment detectors.

The interaction region is surrounded by a pixel-vertex detector which consists of 5 concentric CCD layers with radii between 1.5 cm and 6 cm. It provides excellent resolution and allows the identification of primary and secondary vertices. Two layers of Si-strip detectors provide additional track points before the particles enter the main tracker.

A large volume time projection chamber (TPC) of about 1.5 m radius is used as the main tracking device providing up to 200 points per measured track. Compared to a

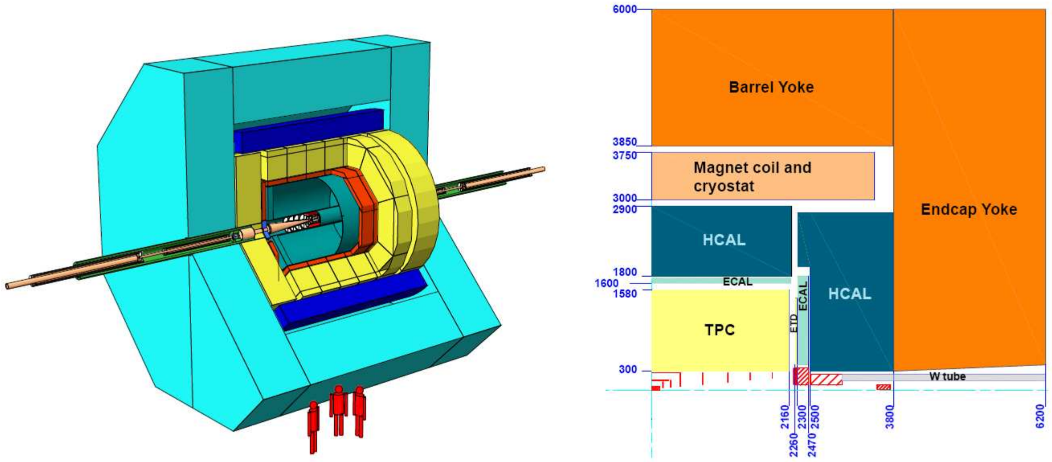

Figure 1.6: View of the LDC, as simulated with the MOKKA simulation package (left) and 1/4 view of the LDC (right). Figure taken from [16].

Si tracker the TPC has a low point resolution of about $100\,\mu$m but has the advantage of many points per track and very few material in the volume. It also allows for better particle identification through dE/dx measurements. The chamber will be read out on the endplates using gas amplification systems like a Gas Electron Multiplier (GEM) or a Micro Mesh Gaseous Detector (Micromegas). Another layer of Si-strip detectors on the outside of the TPC provides the link to the calorimeter system.

The electromagnetic calorimeter (ECAL) will provide 30 samples and uses tungsten as absorber material. The detector layers consist of Si-diodes with $5.5 \times 5.5\,\mathrm{mm}^2$ readout cells. The hadronic calorimeter (HCAL) consists of $3{\times}3\,\mathrm{cm}^2$ scintillator cells, but gaseous $1 \times 1\,\mathrm{cm}^2$ cells are considered as an alternative. Both calorimeters are designed for the "particle flow" concept and provide high granularity to distinguish energy depositions from neutral and charged particles. They are both placed inside the coil to avoid energy loss in the coil system.

A large superconducting coil of about 3 m radius provides a 4 T field for the tracking of charged particles. The magnetic field will eventually be disturbed by additional DID or anti-DID fields and thus requires a high precision field map.

The outermost part of the LDC is the muon system which uses the iron of the magnet flux return yoke as absorber with detectors in-between the iron slabs. The detector technology has not yet been decided on. The system will also feature a tail catcher placed right outside the coil to identify high energetic showers that penetrate the calorimeter system.

2 Time Projection Chamber

2.1 Concept of a TPC

A time projection chamber (TPC) is a three dimensional tracking device. It usually consists of a cylindrical gas filled volume and a homogeneous electric field parallel to its axis, with the cathode dividing the chamber at the center and two anodes at the endplates of the cylinder (see Figure 2.1). An additional magnetic field, parallel to the electric field, is usually provided by a solenoid magnet. Any particle with mass m and the charge q in an electric field $\vec{E}$ or magnetic field $\vec{B}$ is influenced by the Lorentz force:

$$\vec{F}_L = m\frac{d\vec{v}}{dt} = q\vec{E} + q\left(\vec{v} \times \vec{B}\right). \tag{2.1}$$

Particles moving perpendicular to a magnetic field are thus forced on a circular track with the radius being dependent on the particle charge, mass and momentum as well as the magnetic field strength. For high energetic particles, like those produced in particle collisions, $q\vec{E}$ is negligible. This fact is used in tracking detectors for the identification of charged particles.

A charged particle going through the chamber will ionize the gas along its track by exchanging a virtual photon with the detector gas. The number of ionized detector gas molecules is dependent on the energy deposition in the gas along the particle track (dE/dx). This energy deposition is characteristic for different particles and thus also allows particle identification. For a detailed review of energy deposition in matter see [32, Chapter 27: Passage of Particles through matter].

The energy of these primary electrons is often high enough to ionize further molecules of the detector gas and produce secondary electrons. Therefore, the electrons are usually produced in clusters.

2.1.1 Particle Drift and Diffusion

The produced free electrons from the ionization will drift towards the anode while the ions will drift towards the cathode. A readout plane placed at the anode detects the electrons and produces a projection of the track in the r-ϕ plane. The z coordinate of each track point can be reconstructed from the drift time, which requires of course a good understanding of the drift motion.

The movement of the drift electrons is described by equation (2.1) modified by a friction term to represent collisions with gas molecules. Such a differential equation is called a Langevin equation. Assuming that the fields vary only slowly over the free path length of the electrons between two collisions the equation can be solved by averaging over a

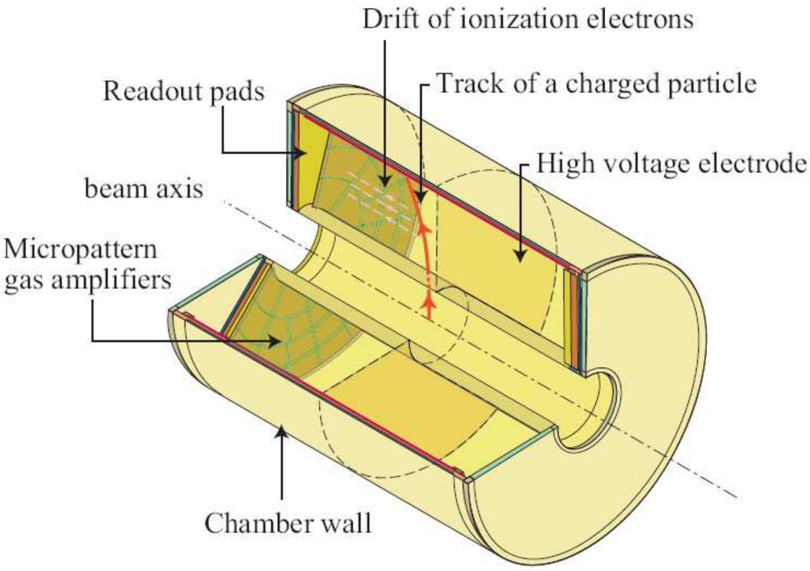

Figure 2.1: Schematic layout of a TPC. Figure taken from [11].

long time t compared to the mean time between two collisions τ. For the drift speed $\vec{v}_d$ one finds the stationary solution

$$m\frac{d\vec{v}_d}{dt} = 0 = q\vec{E} + q\left(\vec{v}_d \times \vec{B}\right) - \frac{m}{\tau}\vec{v}_d. \tag{2.2}$$

Introducing the particle mobility $\mu = \frac{q}{m}\tau$ and the Cyclotron frequency $\vec{\omega} = \frac{q}{m}\vec{B}$ the equation can be transformed into

$$\vec{v}_d = \mu\vec{E} + \tau\left(\vec{v}_d \times \vec{\omega}\right). \tag{2.3}$$

The solution for the drift speed is thus

$$\vec{v}_d = \frac{\mu E}{1+\omega^2\tau^2}\left[\hat{E} + \vec{\omega}\tau\left(\hat{E}\times\hat{B}\right) + \omega^2\tau^2\left(\hat{E}\cdot\hat{B}\right)\hat{B}\right], \tag{2.4}$$

with the unit vectors $\hat{E} = \vec{E}/E$ and $\hat{B} = \vec{B}/B$. The parameters τ and μ dependend on the gas used in the TPC. Using the relation $\mu\vec{B} = \tau\vec{\omega}$ the drift speed can be expressed only in terms of the field strengths and the particle mobility

$$\vec{v}_d = \frac{\mu E}{1+\mu^2B^2}\left[\hat{E} + \mu\vec{B}\left(\hat{E}\times\hat{B}\right) + \mu^2B^2\left(\hat{E}\cdot\hat{B}\right)\hat{B}\right]. \tag{2.5}$$

In a TPC with a perfectly aligned electric and magnetic field the magnetic field would not contribute to the drift speed.

The ILC will have an inhomogeneous magnetic field due to an anti-DID field as described in Chapter 1. That is why $\vec{E} \times \vec{B}$ effects have to be considered. This makes a high precision magnetic field map even more important for a TPC based detector concept. This is, because the magnetic field not only affects the bending of particle tracks but also the track reconstruction itself. For the large TPC prototype and the PCMAG the needed accuracy of the magnetic field in order to provide a good track reconstruction was estimated to a few Gauss, which is a relative error of about 10^{-4}.

In addition to the drift motion the electrons are affected by diffusion which leads to errors in the track reconstruction. The choice of the gas has a huge impact on the diffusion. In Argon, which is a typical TPC gas, the longitudinal movement is dominated by the electric field at a moderate field strength. In other gases like CO_2 the thermal movement is dominant up to much higher field strengths. According to equation (2.5) the transverse diffusion is damped by the magnetic field. A transverse moving electron is forced on a curled track and thus its transverse diffusion is smaller than without a magnetic field.

2.1.2 Gas Amplification and Readout System

The number of electrons produced through primary and secondary ionization is far to low to be detected in the readout plane. Therefore, an amplification system is needed to produce a signal which is large enough to be detected. The amplification is usually achieved by strong local electric fields, which cause ionization avalanches when a charged particle passes the field. The problem with the gas amplification is that ions are produced proportional to the gain. These ions drift back into the TPC volume and create local perturbations in the electric field and thus affect the drift behavior of electrons from a later track. The TPC for the ILC will have about one hundred bunch crossings while one track is being read out, so the ion feedback problem has to be solved. One solution is to indroduce a gating mechanism in-between the drift volume and the amplification system.

The classical readout system for gaseous detectors are multiwire proportional chambers (MWPC) [19]. They basically consist of a set of parallel anode wires in a plane. These wires lie at a higher potential than the local drift field and thus create a gas amplification. The electrons are then either detected in the wires or in a clustered pad plane behind the wires. The resolution of this setup is limited by the distance between two neighboring wires. An additional plane of shielding wires in front of the anode wires is used to straighten the field lines in the drift volume. A third plane of gating wires between the shielding and the drift volume is used to absorb the ions produced in the gas amplification. This gate has to be activated through some trigger mechanism, which disqualifies MWPCs in an ILC detector due to the low time between two bunch crossings. Also the low track resolution is a problem for the needed ILC detector requirements.

An alternative are micropattern gas amplifiers like Gas Electron Multipliers (GEM) [15] or Micro Mesh Gaseous Detectors (Micromegas) [21]. They provide a much better track resolution because of the much smaller structures compared to an MWPC and an intrinsic ion feedback suppression. These are the most likely candidates for the readout

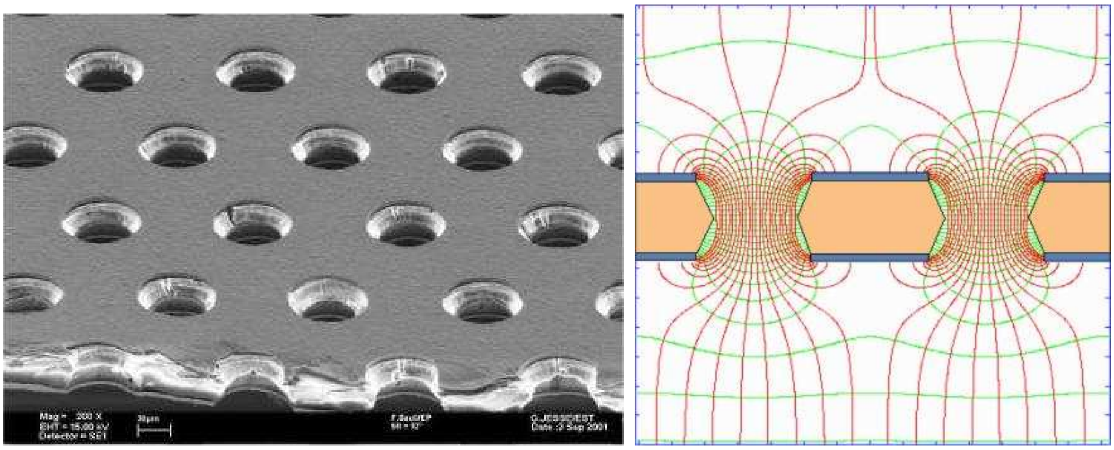

Figure 2.2: Picture of a GEM foil taken with an electron microscope (left) and schematic of the electron field lines in a GEM from the drift volume in the top to the transfer volume in the bottom (right). Figures taken from [3].

system of an ILC detector TPC and they are issue of various R&D efforts. As an example for these kind of detectors the GEM is described below.

A GEM consists of a Kapton foil ($\sim 50\,\mu$m) with a thin copper coating ($\sim 5\,\mu$m) on both sides. A hexagonal pattern of holes is edged into the foil. These holes have diameter of about $70\,\mu$m and a pitch of about $140\,\mu$m. Because of the edging process the hole shape is usually double conical (see Figure 2.2). The values and the materials quoted above are those of the GEMs developed by CERN, but different layouts are available as well.

A voltage of 100 V in-between the copper layers is enough to produce a field of several 10 kV/cm in the GEM holes which is needed for the gas amplification. For an even higher gain GEMs can be arranged in a stacked setup. This way the GEMs can be operated at a high gain without the need of high voltages in the different GEMs. From Figure 2.2 can be seen that many field lines near the holes end on the GEM surface. During the amplification avalanche the slow ions are drawn to the surface of the GEM, while the lighter electrons are extracted because of the higher field in the transfer volume compared to the drift volume. A magnetic field perpendicular to the GEM foil increases the fraction of extracted electrons from the holes. This intrinsic ion feedback suppression is even better in a multi GEM setup.

The electrons are then detected in a clustered pad plane. The pad structure has to be significantly smaller compared to an MWPC in order to account for the smaller amplification structures. A readout system based on a Si-pixel detector like the Timepix chip [25] is considered as well.

2.2 The Large TPC Prototype

The Large TPC Prototype (LP) (see Figure 2.4) is the next big step towards the design of the LDC main tracker with a diameter of about 75 cm and a length of 60 cm. It will be placed in the PCMAG superconducting solenoid with a maximum field of about 1.25 T (see Chapter 3) and will be operated at the DESY testbeam area with an electron beam of up to 6 GeV. The components for the LP are currently being produced by various groups worldwide and the first testbeam activities are scheduled for late 2008.

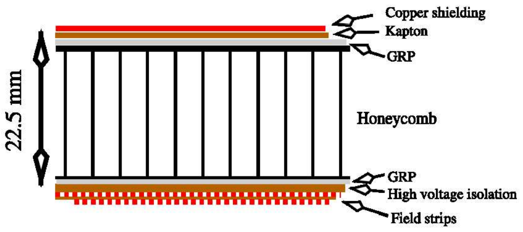

Figure 2.3: Schematic view of the field cage wall structure. Figure taken from [12].

The prototype is designed to test all necessary subsystems of a TPC for the LDC and allows the testing of different gas mixtures, gas amplification systems, readout electronics and data aquisition systems (DAQ). It will be movable within the magnet to allow the operation at various levels of magnetic field homogeneity to simulate the effects of field inhomogeneity by an anti-DID. To achieve this a dedicated mounting structure for the TPC is being developed by the DESY FLC group. The complete setup of magnet and TPC will be movable with respect to the testbeam and thus allows for testbeam tracks through every part of the TPC volume. Si-strip detectors placed between the the TPC and the magnet will provide reference measurements for the track and additional Si detectors on the top and bottom of the chamber allow for tests with cosmic particles.

The main barrel or field cage [12] is being built by the DESY FLC group and is a compromise of stability and lightweight design to provide a minimum of material in the particle path. A cross section of the field cage wall can be seen in Figure 2.3. It consists of two layers of Glass Reinforced Plastic (GRP) with a honeycomb structure of aramid in-between. A copper covered Kapton layer on the outside and another Kapton layer on the inside provide the electrical shielding of the volume. The innermost layer is a foil of field strips which are needed to provide the needed relative field homogeneity of 10^{-4}. The field strips are a set of parallel rings lying at different potentials. The potential reaches from ground potential at the anode to more than 20 kV at the cathode. Another set of field strips, so called mirror strips, are needed to close the gaps between the field strips and to avoid field inhomogenieties near the walls of the TPC.

The anode endplate has a modular design to allow for easy installation and exchange of the gas amplification and readout system. Currently several modules with different systems are being built. These include different GEM and Micromegas systems with pad readout as well as a GEM system with a pixel readout system.

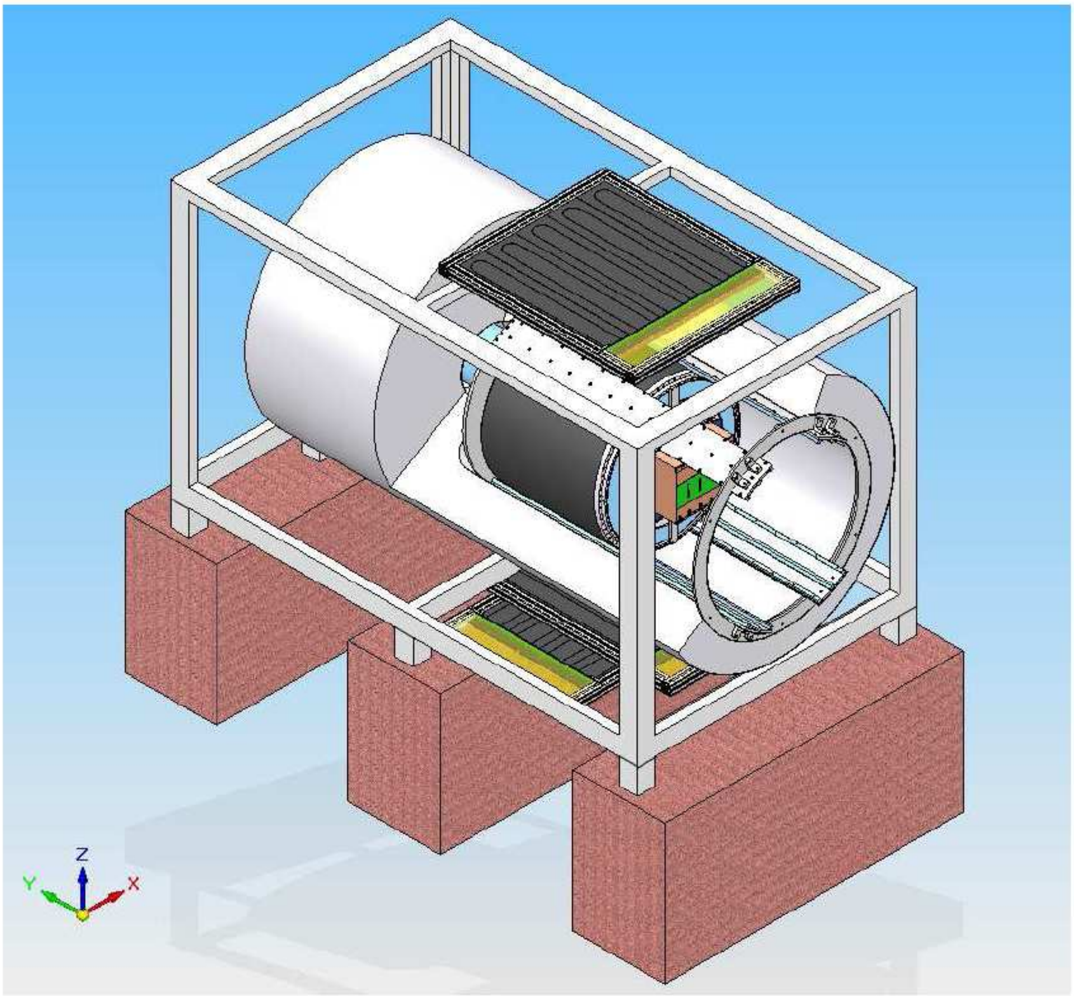

Figure 2.4: Schematic view of the LP in the PCMAG.

3 Magnet

3.1 The PCMAG

The PCMAG is a superconducting large bore solenoid magnet with a radius of 86 cm and an active length of about 1 m. The maximum magnetic field is about 1.2 T at a current of 520 A. For the LP the magnet will be operated at 430 A with a maximum magnetic field of 1 T. The PCMAG is part of the EUDET infrastructure for detector development towards an international linear collider and is placed at the DESY testbeam area since 2006.

The magnet was designed and previously used for the Japanese-American Collaborative Emulsion Experiment (JACEE) [4]. There it was used in balloon experiments in the Antarctica together with a lead-emulsion chamber to directly measure the primary composition and spectra of cosmic rays at energies in the region of 1-1000 TeV. This results in a lightweight design and a total weight of the magnet of less than 500 kg.

The inner volume of PCMAG has a bottleneck shape because of the liquid He (LHe) tank in the small end (see Figure 3.1). This tank has a volume of 260 l and, once cooled, keeps the coil at LHe temperature for about one week. The coil itself is a closed circuit and has to be excited and deexcited through a secondary circuit. This means that in an emergency case the current can not be extracted faster than within a few minutes without quenching and thus destroying the coil.

The coil consists of 3342 windings in 4 layers over the full length and additional 4 layers at the ends. It has no flux return yoke. The additional layers at the ends are needed to provide a higher field homogeneity in the center of the coil, but they also lead to higher field gradients at the ends of the coil. The overall low field homogeniety will be exploited to test the LP at different levels of field homogeniety, in order to simulate the effects of an anti-DID (see Chapter 1).

3.2 Magnetic Field Models

In order to create a map of the magnetic field, it was measured throughout the volume of PCMAG (see Chapter 4). A simple field map can be interpolated directly from the measured data, but in order to understand the data and to be able to correct for any systematic effects during the measurement one has to compare the data with a model of the magnetic field. This model can be fitted to the data and will be the source of the final field map after all corrections have been applied. Two completely different ways to model the field where chosen and in the end a combination of both was used to create the final field map.

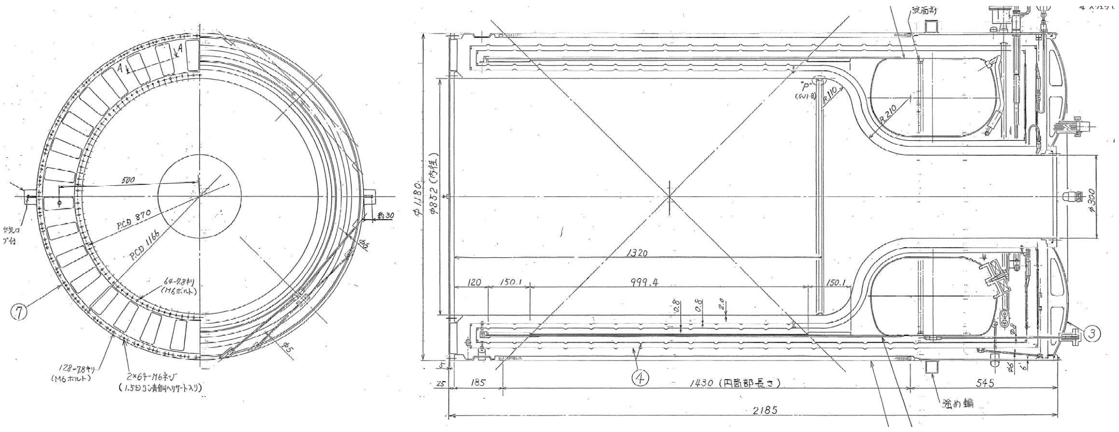

Figure 3.1: Front view (left) and side view (right) of PCMAG. All technical drawings of PCMAG can be found at [2].

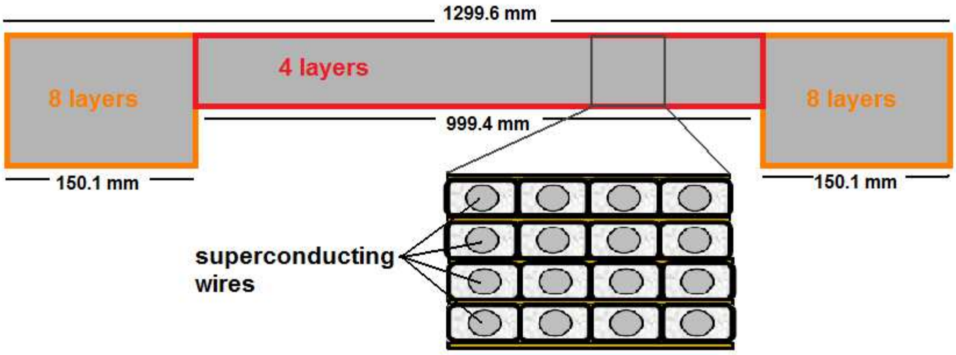

Figure 3.2: Schematic view of the PCMAG coil.

All the field models share a cylindrical coordinate system with the z-axis being alligned with the coil axis and the origin being placed at the center of the coil. To be consistent with the measurement coordinate system z increases towards the back of the coil and $\phi = 0°$ is pointing to the left when looking from the front.

3.2.1 Coil Model

The first approach to model the magnetic field of PCMAG was to represent the coil as a set of closed current loops and evaluate the magnetic field as a superposition of all loops.

The magnetic field of a single closed current loop in cylindrical coordinates is given by [23]

$$B_z(r,\phi,z) = \frac{\mu_0 I}{\pi}\frac{1}{2\alpha^2\beta}\left(\left(R^2-\rho^2\right)\mathrm{E}(k)+\alpha^2\mathrm{K}(k)\right) \tag{3.1}$$

$$B_r(r,\phi,z) = \frac{\mu_0 I}{\pi}\frac{z}{2\alpha^2\beta r}\left(\left(R^2+\rho^2\right)\mathrm{E}(k)-\alpha^2\mathrm{K}(k)\right) \tag{3.2}$$

$$B_\phi(r,\phi,z) = 0, \tag{3.3}$$

where R is the radius of the loop, I is the current, K and E are the complete elliptic integrals of the first and second kind respectively, $\rho^2 = r^2 + z^2$, $\alpha^2 = R^2 + \rho^2 - 2Rr$, $\beta^2 = R^2 + \rho^2 + 2Rr$ and $k^2 = 1 - \frac{\alpha^2}{\beta^2}$.

For the complete coil the magnetic field was calculated as the sum of the field of 3344 closed current loops. These loops where placed according to the drawings of the magnet (see Figure 3.2) at 680 different z-positions with 8 different radii to represent the coil with its 8 layers of windings. The first and last 78 z positions have 8 layers and the central part has 4 layers. The real coil has only 3342 windings which is most likely due to the need of transitions from the 8 layer to the 4 layer part, but this could not be reconstructed from the drawings. Another issue is that a real coil has no closed loops, but some small tiltings in the current instead. This effect was assumed to be negligible since the coil windings go into one direction for one layer and into the other direction for the next layer. So there is no effective current flow into one direction and no influence on the magnetic field at distances from the windings which are large compared to the pitch between the layers (~1 mm).

The number of windings is fixed, as well as their relative position. The pitches between the windings are always the same. This leaves the model with only four free parameters.

- The length, which is equivalent to the pitch in z direction.
- The radius of the innermost layer.
- The pitch between the different layers.
- The current.

The advantage of this model is, although it makes some simplifications, that all parameters are directly connected to known attributes of the coils and can be compared directly to the values given in the magnet's drawings.

The drawback of this model is the huge amount of computing needed to calculate the magnetic field at a given coordinate. To speed up the fitting process the numerical algorithms to calculate the elliptic integrals $\mathrm{K}(k)$ and $\mathrm{E}(k)$ were changed to a lookup table of precalculated values for different k. For further speed improvement the number of windings was reduced. Four layers and two adjacent windings were combined to one winding and thus the total number of windings and also the computing time was reduced by a factor of 8, while the quality of the field map was still acceptable.

The fits were done with both coil models, the full model consisting of 3444 windings and the simplified model consisting of 418 windings. The fit of the full model was only done with a reduced set of data in order to reduce the computing time.

3.2.2 Maxwell's Equations

A more general approach to model the field is to use Maxwell's equations. This method was inspired by [10, 22, 31] and will be further referred to as Fourier-Bessel (FB) model, due to its mathematical structure.

The inner volume of PCMAG contains no currents and no magnetic materials, so the magnetic field $\vec{B}$ satisfies the equation

$$\vec{\nabla}\vec{B} = 0 \tag{3.4}$$

and $\vec{B}$ can be expressed in terms of the magnetic scalar potential Φ

$$\vec{B} = -\vec{\nabla}\Phi, \tag{3.5}$$

where Φ satisfies Laplace's equation

$$\vec{\nabla}^2\Phi = 0. \tag{3.6}$$

A solution to Laplace's equation in cylindrical coordinates can be found by separation of variables:

$$\Phi(r, \phi, z) = R(r)P(\phi)Z(z). \tag{3.7}$$

The axial and radial factors take three different forms:

$$\begin{aligned} Z(z) &= A\sin(\lambda z) + B\cos(\lambda z) \\ R(r) &= C\mathrm{I}_n(\lambda r) \end{aligned} \tag{3.8}$$

$$\begin{aligned} Z(z) &= A\sinh(\lambda z) + B\cosh(\lambda z) \\ R(r) &= C\mathrm{J}_n(\lambda r) \end{aligned} \tag{3.9}$$

$$\begin{aligned} Z(z) &= Az + B \\ R(r) &= Cr^n, \end{aligned} \tag{3.10}$$

where $\mathrm{J}_n(\lambda r)$ and $\mathrm{I}_n(\lambda r)$ are Bessel and modified Bessel functions of order n respectively, $\lambda > 0$, $n = 0, 1, 2, ...$ and A, B and C are arbitrary constants. The azimuthal factor takes always the form

$$P(\phi) = A\sin(n\phi) + B\cos(n\phi).$$

The general solution for Φ can be expressed as an infinite sum over these terms.

The fact that $\Phi(r, \phi, z)$ satisfies Laplace's equation (3.6) allows the magnetic field within a given volume to be reconstructed from the magnetic field on the surface of the volume. This can be used to calculate the magnetic field within the entire cylindrical volume of PCMAG only from the measurements at the outermost radii ($r = r_{\text{max}}$) and on the end surfaces ($z = \pm z_{\text{max}}$), with z_{max} being half the length of the cylindrical volume. Using Equation (3.5) the solution for $\vec{B}$ in cylindrical coordinates can be written as:

$$\begin{aligned}
B_z(r,\phi,z) =& \sum_{n=0}^{\infty}\sum_{l=1}^{\infty} A_{nl}\mathrm{I}_n\left(\frac{l\pi}{z_{\text{max}}}r\right)\cos\left(n\phi+\alpha_{nl}\right)\cos\left(\frac{l\pi}{z_{\text{max}}}z\right)\\
&-\sum_{n=0}^{\infty}\sum_{l=1}^{\infty} B_{nl}\mathrm{I}_n\left(\frac{l\pi}{z_{\text{max}}}r\right)\cos\left(n\phi+\beta_{nl}\right)\sin\left(\frac{l\pi}{z_{\text{max}}}z\right)\\
&+\sum_{n=0}^{\infty} A_{n0}r^n\cos\left(n\phi+\alpha_{n0}\right)\\
&+\sum_{n=0}^{\infty}\sum_{m=1}^{\infty} C_{nm}\mathrm{J}_n\left(\frac{\zeta_{nm}}{r_{\text{max}}}r\right)\cos\left(n\phi+\gamma_{nm}\right)\cosh\left(\frac{\zeta_{nm}}{r_{\text{max}}}z\right)\\
&+\sum_{n=0}^{\infty}\sum_{m=1}^{\infty} D_{nm}\mathrm{J}_n\left(\frac{\zeta_{nm}}{r_{\text{max}}}r\right)\cos\left(n\phi+\delta_{nm}\right)\sinh\left(\frac{\zeta_{nm}}{r_{\text{max}}}z\right)
\end{aligned}\tag{3.11}$$

$$\begin{aligned}
B_r(r,\phi,z) =& \sum_{n=0}^{\infty}\sum_{l=1}^{\infty} A_{nl}\mathrm{I}'_n\left(\frac{l\pi}{z_{\text{max}}}r\right)\cos\left(n\phi+\alpha_{nl}\right)\sin\left(\frac{l\pi}{z_{\text{max}}}z\right)\\
&+\sum_{n=0}^{\infty}\sum_{l=1}^{\infty} B_{nl}\mathrm{I}'_n\left(\frac{l\pi}{z_{\text{max}}}r\right)\cos\left(n\phi+\beta_{nl}\right)\cos\left(\frac{l\pi}{z_{\text{max}}}z\right)\\
&+\sum_{n=0}^{\infty} A_{n0}nr^{n-1}\cos\left(n\phi+\alpha_{n0}\right)z\\
&+\sum_{n=0}^{\infty}\sum_{m=1}^{\infty} C_{nm}\mathrm{J}'_n\left(\frac{\zeta_{nm}}{r_{\text{max}}}r\right)\cos\left(n\phi+\gamma_{nm}\right)\sinh\left(\frac{\zeta_{nm}}{r_{\text{max}}}z\right)\\
&+\sum_{n=0}^{\infty}\sum_{m=1}^{\infty} D_{nm}\mathrm{J}'_n\left(\frac{\zeta_{nm}}{r_{\text{max}}}r\right)\cos\left(n\phi+\delta_{nm}\right)\cosh\left(\frac{\zeta_{nm}}{r_{\text{max}}}z\right)\\
&+\sum_{n=0}^{\infty} E_{n0}nr^{n-1}\cos\left(n\phi+\epsilon_n\right)
\end{aligned}\tag{3.12}$$

$$
\begin{aligned}
B_\phi(r,\phi,z) = &-\sum_{n=0}^{\infty}\sum_{l=1}^{\infty} A_{nl}\frac{z_{\max}}{l\pi r}\mathrm{I}_n\left(\frac{l\pi}{z_{\max}}r\right)\sin\left(n\phi+\alpha_{nl}\right)\sin\left(\frac{l\pi}{z_{\max}}z\right)\\
&-\sum_{n=0}^{\infty}\sum_{l=1}^{\infty} B_{nl}\frac{z_{max}}{l\pi r}\mathrm{I}_n\left(\frac{l\pi}{z_{\max}}r\right)\sin\left(n\phi+\beta_{nl}\right)\cos\left(\frac{l\pi}{z_{\max}}z\right)\\
&-\sum_{n=0}^{\infty} A_{n0}nr^{n-1}\sin\left(n\phi+\alpha_{n0}\right)z\\
&-\sum_{n=0}^{\infty}\sum_{m=1}^{\infty} C_{nm}\frac{z_{max}}{\zeta_{nm}r}\mathrm{J}_n\left(\frac{\zeta_{nm}}{r_{\max}}r\right)\sin\left(n\phi+\gamma_{nm}\right)\sinh\left(\frac{\zeta_{nm}}{r_{\max}}z\right)\\
&-\sum_{n=0}^{\infty}\sum_{m=1}^{\infty} D_{nm}\frac{z_{max}}{\zeta_{nm}r}\mathrm{J}_n\left(\frac{\zeta_{nm}}{r_{\max}}r\right)\sin\left(n\phi+\delta_{nm}\right)\cosh\left(\frac{\zeta_{nm}}{r_{\max}}z\right)\\
&-\sum_{n=0}^{\infty} E_{n0}nr^{n-1}\sin\left(n\phi+\epsilon_n\right),
\end{aligned}
\tag{3.13}
$$

where I'_n and J'_n are the first derivatives of I_n and J_n respectively, A_{nl}, B_{nl}, C_{nm}, D_{nm} and E_n are arbitrary constants, $\alpha_{nl}, \beta_{nl}, \gamma_{nm}, \delta_{nm}$ and ϵ_n are arbitrary phases and ζ_{nm} are the mth roots of the Bessel functions J_n.

The terms in equations (3.11), (3.12) and (3.13) can be divided into three different classes. The first three lines are always a double Fourier expansion in z and ϕ. They are the dominant terms in a solenoid field and the coefficients A_{nl} and B_{nl} can be determined from the measured field on the curved surface of the cylinder. The expansion in z gives a $2z_{\max}$-periodic model. If $2z_{\max}$ would be equal to the length in z over which the magnetic field was measured this would lead to discontinuities at both ends of the cylinder. This effect can be avoided by expanding the model and choosing a slightly larger $z_{\max}$ and moving the discontinuity outside the volume of interest.

The fourth and fifth line in equations (3.11), (3.12) and (3.13) are a double Fourier expansion in r and ϕ which disappears on the curved surface for $r = r_{\max}$. The corresponding coefficients C_{nm} and D_{nm} can be found from the field measured at the ends of the cylinder.

The last line in equations (3.12) and (3.13) with the coefficients E_n are multipole terms that are independent of z and make no contribution to B_z.

All these series have to be truncated for the fitting procedure. While a large number of terms is desirable in order to provide the best description of the magnetic field, the number of terms also has to be smaller then the number of measured points in the respective direction to avoid oscillating behavior of the model.

The advantage of this model is that it does not need any geometrical information of the current distribution causing the magnetic field inside the volume of interest. All information comes from the strong constraints implied by Maxwell's equations and the measured field on the surface of the volume. But this is also its disadvantage. The parameters have no direct physical meaning and so there is no way to extrapolate the field outside of the measured volume.

For this field map the parameters were obtained using a minimization method but since the equations (3.11), (3.12) and (3.13) are basically double Fourier series the different parameters may also be obtained through numerical integration over parts of the measured data. Although this method was not used, the solutions for the different coefficients are given in Appendix B for completeness.

The reason for not using the integration method is, that it requires the data to be available on an equally spaced grid on the two hyperplanes for $r = r_{\text{max}}$ and $z = z_{\text{max}}$. This was not true, mostly due to the different mearurement positions for the different components. Interpolating in-between the measurement positions in order to produce such a grid was depricated because of the inhomogeneity of the magnetic field.

With a different Hall sensor card layout or for a higher number of parameters the integration method should definately be preferred over the minimization method.

For the field map a compromise of the two models described above is chosen. The measured field and the model of the closed current loops obey Maxwell's equations, so the difference of both also has to obey them. The FB model is then used to describe this difference and thus only contributes small corrections to the final field map. The overall shape of the field is given by the coil model.

4 Magnetic Field Measurements

4.1 Hall Sensor Cards

The magnetic field of PCMAG was measured by 24 Hall sensor cards which where developed at CERN. Each of these cards holds three individual Hall sensors, one for each field component. Those sensors are placed at one edge of the card with only a few mm distance from each other (see Figure 4.1).

The sensor cards where calibrated at CERN in a homogeneous 2 T magnetic field using a special technique where the card holding the three sensors is rotated in the magnetic field. Afterwards the three field components are reconstructed using a series of spherical harmonics. This way the calibration is extremely precise, also taking into account higher order effects like the planar Hall effect. It also eliminates the effect of small misalignments of the three sensors, since all these effects are included in the calibration and the orientation of the three sensors is fixed with respect to the sensor card. A detailed description of the calibration method can be found in [13].

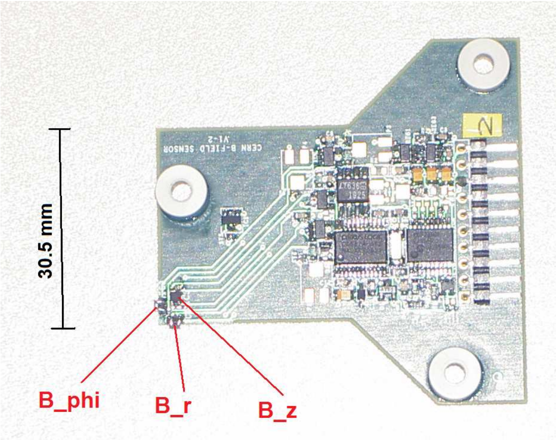

Figure 4.1: One of the Hall sensor cards used during the field mapping.

The disadvantage of this calibration method is that it does not take into account the slightly different position of each individual sensor (see Table 4.2), which has no effect within a homogeneous field. It turned out that the high inhomogeneity of the field of PCMAG made this effect non-negligible. A better design of the cards might have been a six sensor setup with two sensor for each field component and all six sensors at the same distance from the effective measurement point. The average of the two measured field values for each field component would be the magnetic field at the same position for all three components and thus eliminates the need for further corrections.

4.2 Measurement Bench

In order to measure the magnetic field of PCMAG a special measurement setup was built by CERN. This system consisted of a rail which was aligned with the magnet axis and

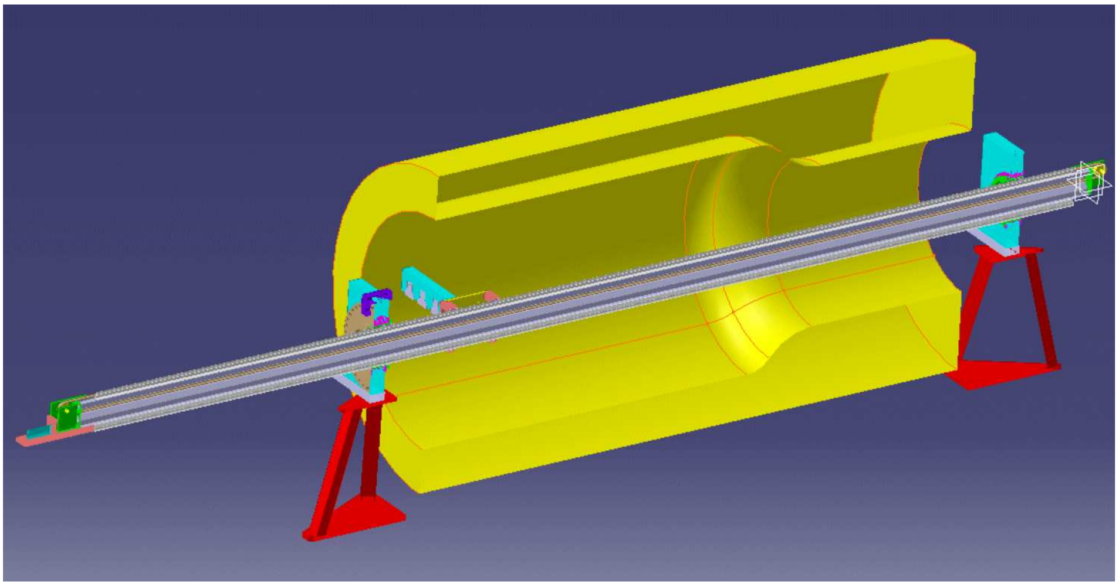

Figure 4.2: Schematic view of the measurement setup in the PCMAG. Original image by P. A. Giudici.

two arms with 12 Hall sensor cards each. The arms were attached rectangular to the rail in order to cover the inner diameter of PCMAG and could be moved along the bench by a step motor with a precision of 0.2 mm. They could be rotated manually in steps of 2.5°. This way the magnetic field could be measured at equally distant points everywhere within the volume of PCMAG (see Figure 4.2).

The 12 sensor cards per arm where mounted at 12 different radii so that the center of mass of the three individual sensors where perfectly aligned. Six cards where mounted on the front and another six cards on the back of the arm with the front and back positions being the opposite for the left and the right arm. This way the front probes of the left arm measured the field at the same radii as the back probes of the right arm and vice versa (see Table 4.1). Taking into account the distance between front and back probes of 56 mm this was used for redundant measurements.

The probes 1 to 6 were mounted on the front of the left arm, 7 to 12 on the front of the right arm, 13 to 18 on the back of the right arm and 19 to 24 on the back of the left arm. An image of one of the arms together with the mounted Hall sensor cards can be seen in Figure 4.3.

The coordinate system is a cylindrical system with the z-axis being aligned with the rail and the origin being placed at the first measurement position and z increasing with the measurement position. $\phi = 0°$ is pointing to the left when looking from the front. This corresponds to a right handed Cartesian coordinate system with x pointing to the left and y to the top when looking from the front.

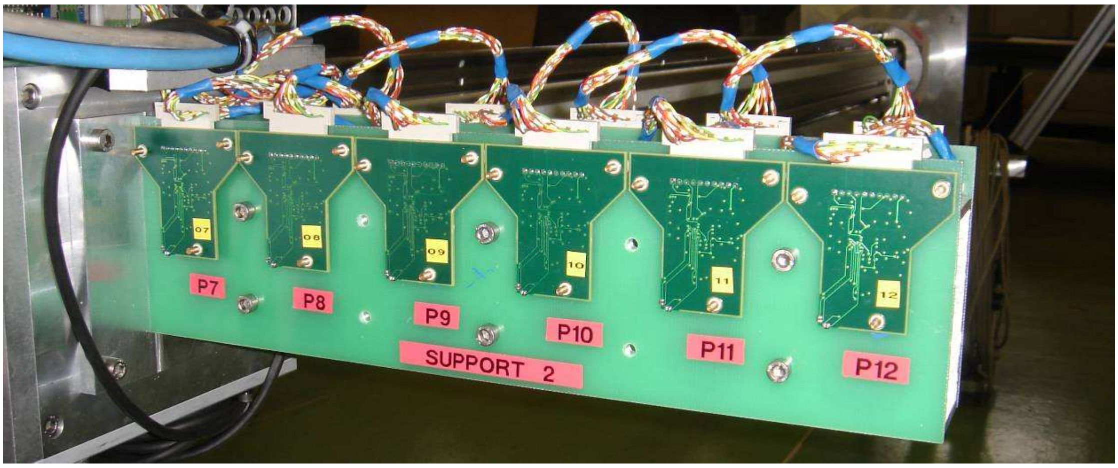

Figure 4.3: One measurement arm together with the mounted Hall sensor cards.

Table 4.1: Radial positions of the 24 Hall sensor triplets.

probe	r-position (mm)	probe	r-position (mm)
1	115.1	13	-115.1
2	172.6	14	-172.6
3	230.1	15	-230.1
4	287.6	16	-287.6
5	345.1	17	-345.1
6	402.6	18	-402.6
7	-89.4	19	-89.4
8	-146.9	20	146.9
9	-204.4	21	204.4
10	-261.9	22	261.9
11	-319.4	23	319.4
12	-376.9	24	376.9

Table 4.2: Offsets for individual probes from Hall sensor triplet position.

probe	x (mm)	y (mm)	z (mm)
B_r	2.54	0.91	-0.75
B_ϕ	-0.61	-1.78	-0.75
B_z	-1.88	1.04	0.15

4.3 Measurement Campaign

The whole field mapping campaign at DESY in July 2007 took four days plus one week of preparations, including the setup of the measurement system and the cooling of the magnet. The measurement rail was alligned with the magnets axis using a laser position measurement system. The same system was used to measure the position of the probes with respect to the magnet and the testbeam area. In order to define a reference coordinate system permanent marks have been placed on the magnets hull and the walls of the testbeam area. For the field mapping the magnet was only operated at 430 A with a nominal maximum field of 1 T because this will be the only field strength at which the magnet will be operated during TPC operation.

For reference measurements a Nuclear Magnetic Resonance (NMR) probe was used. These kind of probes are extremely precise (10^{-6} T). The probe was placed inside the rail at the center of the rail. Two additional Hall sensor cards of the same type as used on the measurement arms were mounted permanently at PCMAG. One on the front face of the magnet and one in the bottle neck volume at the back. Those cards were meant to be used as reference during later magnet operations, but a check of the cards which were mounted on the arms a few month after the measurement campaign showed that the calibration of the Hall probes was not stable over time. This makes these cards useless for long term reference measurements and an alternative reference measurement method has to be provided until TPC operation in late 2008.

The magnetic field of PCMAG was excited twice to the nominal 1T during those four days. One time as a test and a second time for the actual field mapping. The measured field by the NMR probe was only 3 G lower during the first excitation, which shows the high reproducability of the magnetic field. Since both excitations were done during one cooling of the magnet any effects of the shrinking of the coil on reproducability can not be excluded. Once excited the magnetic field is extremely stable, which can be seen from the NMR data in Figure 4.4. All points in the left plot where taken when the arms were in their homing position at the front of the magnet. The right plot in Figure 4.4 shows that the position of the measurement arms on the rail has a non-negligible effect. The small deviation of a few Gauss is either caused by some magnetizable components in the z-decoder, which moves together with the arms or small bending effects caused by the weight of the arms. During analysis this very local effect has been taken into account for by only using the outer radii measurements and extrapolating towards the inner radii.

The measurement was always done in z-scans at a constant angle of the arms, since the movement along the rail was automatic while the rotation had to be done manually. A stepping of 14 mm in z-direction and 5° in ϕ-direction between 0° and 180° was chosen. From 180° to 360° a stepping of 15° was chosen since these points were redundant measurements due to the layout of the arms. In total the data taken contains 49 z-scans of 89 z-positions for each of the 24 probe cards, which results in more than 100000 B-field triplets at 1 T. The measured Hall voltages were converted into magnetic fields according to the calibration right after the measurement, so the analysis was done only with the converted magnetic field values.

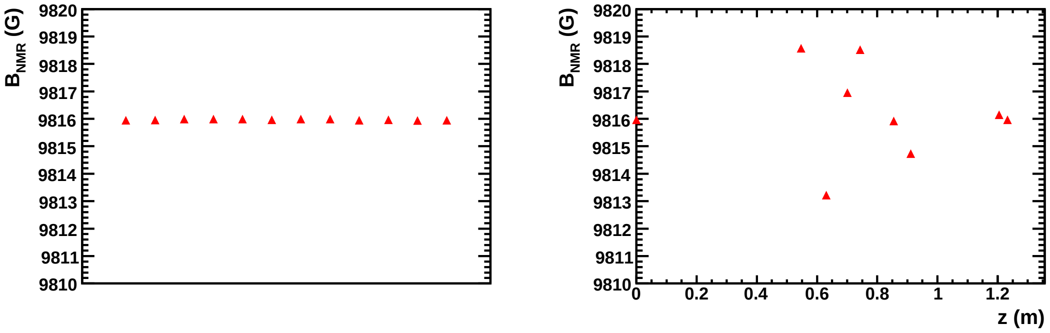

Figure 4.4: NMR reference measurements taken over 3 days at constant z (left) and during one z-scan (right).

4.3.1 Probe Offset Measurements

Two additional z-scans were done at 0 T in order to check for any offsets in the calibration of the sensors. These were done only one hour after the deexcitation of the magnet, so the presence of remnant currents can not be excluded, since the magnet was still cold. For that reason measurements before the magnets excitation would have been the better choice.

The results of the two z-scans, one at $\phi = 0°$ and one at $\phi = 90°$, can be found in Appendix C. From these plots it can be seen that the measurements for all 3×24 individual probes are nearly constant over z. The probes should measure the same mean value for both ϕ-positions, which is also true for most probes. The mean value from all measurements for each probe are given in Table 4.3. For the calculation of the mean value single points to far from the mean value were removed from the data set. The measurement for B_r-90°, which was obviously false, was removed as well. The mean values are subtracted from the field mapping data as probe offsets.

The distribution of the σ for all probes is shown in Figure 4.5. It shows that the mean σ for all probes is about 1.7 Gauss. This is the uncertainty for a single measurement point.

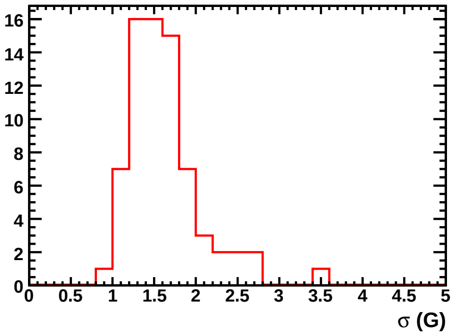

Figure 4.5: Distribution of σ for all 3×24 Hall probes.

Table 4.3: Mean values and σ from the offset measurements.

probe	B_r		B_ϕ		B_z	
	mean (G)	σ (G)	mean (G)	σ (G)	mean (G)	σ (G)
1	4.7	2.0	-0.8	1.5	1.7	1.8
2	2.3	1.6	-3.4	1.7	1.5	1.4
3	2.5	1.6	-2.1	1.8	2.1	1.6
4	3.2	1.7	-2.1	1.7	1.9	1.3
5	2.0	2.4	-2.5	1.4	3.2	1.9
6	3.4	3.0	-1.9	1.7	3.7	1.8
7	2.3	2.2	-2.2	2.1	0.1	3.6
8	1.0	1.9	-0.2	1.4	3.6	1.8
9	2.5	2.0	-3.8	1.8	2.1	1.8
10	1.6	1.7	-2.7	1.4	3.8	1.4
11	2.2	2.3	-2.6	1.8	5.3	1.7
12	0.5	1.7	-0.7	1.4	2.3	1.2
13	0.7	2.0	-1.1	2.7	-1.0	2.0
14	3.4	1.4	-2.7	1.9	-4.5	1.5
15	2.3	2.3	-0.4	1.9	-2.0	1.4
16	1.5	3.0	-2.1	1.6	-4.2	1.3
17	1.3	1.9	-0.8	1.4	-2.9	1.4
18	2.3	1.6	-2.3	1.5	-0.4	1.7
19	1.6	2.0	-3.2	2.3	-2.9	2.1
20	3.8	2.2	-2.2	1.6	-2.3	2.0
21	1.7	1.5	-1.8	1.9	-0.6	1.5
22	-0.8	2.6	-2.1	1.6	-3.2	2.4
23	2.1	1.9	-2.2	2.0	-5.2	2.1
24	2.7	1.8	-1.2	1.5	-2.4	1.4

5 Fitting Process

The aim of the fitting is to minimize the difference between the measured data and the model in order to provide a well understood field map. This was done using a least-squares-fit and the programme MINUIT [1]. The expression minimized in the fit is

$$\chi^2 = \sum_{i,c} \left(\frac{B_{i,c}^{\text{data}} - B_c^{\text{mod}}(\vec{r}_i)}{3\,\text{G}} \right)^2 , \tag{5.1}$$

where c can be r, ϕ or z, $B^{\text{mod}}(\vec{r}_i)$ is the predicted field of the model at the coordinates $\vec{r}_i$ of the measured point B_i^{data} and i runs over all or a subset of the measured points. The error estimation of 3 Gauss was only used to normalize the function to a reasonable value for MINUIT.

Whenever reasonable only the set of the B_z data was used because these measurements have the smallest relative error. In addition most of the parameters introduced by the models in Chapter 3.2 can be calculated only from the knowledge of B_z.

5.1 Coordinate Systems

In order to get the correct residuals the position and orientation of measured and modelled value have to be the same. This requires a transformation of the measurement coordinate system to the model coordinate system and introduces possible additional free parameters. The measurement setup was assumed to be rigid and the two arms to be perfectly perpendicular to the rail. So there is no need for changing coordinate systems depending on the measurement position and only global parameters are introduced. For convenience the transformation of the coordinate systems has been done in Cartesian coordinates.

First of all the offset in space has to be applied, which are three parameters. Additionally a possible tilt of the measurement system with respect to the magnet axis has to be taken into account. These rotations can be described by three angles. Since the magnetic field is highly symmetric in ϕ-direction this angle was excluded from the fitting, so we have two additional parameters from the tilt. Finally the possible tilt of each of the 24 sensor cards introduces another three angles per card. These are negligible for the position but have a huge effect on the measured values of B_r and especially B_ϕ.

Since the three components of every B-triplet were measured at slightly different positions they where treated as three individual measurement points. This is because a correct rotation can only be done if the three components are known simultaneously. So every measurement point consists of three coordinates and one field value pointing in r,

ϕ or z-direction. The transformed measurement position is

$$\begin{aligned} \vec{r}' =& \vec{r}_{\text{offset}} + \mathrm{R}(\phi_{\text{bench}}, \psi_{\text{bench}}, \theta_{\text{bench}}) \cdot \\ & [\vec{r}_{\text{arm}} + \mathrm{R}(\phi_{\text{arm}}, 0, 0) \cdot [\vec{r}_{\text{card}} + \mathrm{R}(\phi_{\text{card}}, \psi_{\text{card}}, \theta_{\text{card}}) \cdot \vec{r}_{\text{sensor}}]] \,, \end{aligned} \tag{5.2}$$

where $\vec{r}_{\text{offset}}$ is the offset between the two coordinate systems, $\vec{r}_{\text{arm}} = (0, 0, z)$ is the z-position of the arm, $\vec{r}_{\text{card}} = (r, 0, 0)$ is the nominal radial position of the sensors and $\vec{r}_{\text{sensor}}$ is the offset for the three individual Hall sensors. The rotation matrices R are defined by Euler angles using the "z y x" convention (see Appendix A). ϕ_{bench}, ψ_{bench} and θ_{bench} are the possible rotations of the rail, ϕ_{arm} is the angular position of the arm and ϕ_{card}, ψ_{card} and θ_{card} are the possible tilt of the different sensor cards.

The transformation for the magnetic field values is the same transformation using only the rotations

$$\vec{B}'_c = \mathrm{R}(\phi_{\text{bench}}, \psi_{\text{bench}}, \theta_{\text{bench}}) \cdot \mathrm{R}(\phi_{\text{arm}}, 0, 0) \cdot \mathrm{R}(\phi_{\text{card}}, \psi_{\text{card}}, \theta_{\text{card}}) \cdot \vec{B}_c. \tag{5.3}$$

The resulting vector $\vec{B}'$ points into the measured direction for the component c in the model coordinate system. This can be any direction and the model field value has to be projected onto this direction in order to calculate the residual. For that reason $\Delta = B^{\text{data}}_{c,i} - B^{\text{mod}}_{c,i}$ in equation (5.1) is replaced by

$$\Delta = \frac{B^{\text{data}}_c}{|B^{\text{data}}_c|} \left(|\vec{B}^{\text{data}}| - \frac{\vec{B}^{\text{mod}} \cdot \vec{B}^{\text{data}}}{|\vec{B}^{\text{data}}|} \right). \tag{5.4}$$

The first factor is added to keep the orientation of the residual and has no effect on the fit since it is squared. The second factor is the actual residual.

5.2 Coil Model and Global Parameters

The global parameters $r_{\text{offset},x}$, $r_{\text{offset},y}$, $r_{\text{offset},z}$, ψ_{bench} and θ_{bench} were fitted together with the coil model described in chapter 3.2.1 and its parameters: the coil length L_{coil}, the inner coil radius R_{coil}, the pitch between the coil layers P_{coil} and the current I_{coil}. The fit was done using only B_z and the data from the high radii probes 5, 6, 11, 12, 17, 18, 23 and 24 and was applied to the full coil model and also to simplified coil model. The resulting best fit values for the geometric parameters can be found in Table 5.1 and the best fit values for both coil models can be found in Table 5.2. Note that there are less windings in the simplified model which results in a four times larger radial pitch and an eight times larger current. The length is shorter than expected which can be explained by the shrinking of the coil during cooling. It is expected that the coil length is reduced by about 0.4% which is about 5 mm and thus agrees better with the fitted values. All other parameters are not affected by the cooling process.

Afterwards the fits of the three angles per Hall sensor card were done using the data from one probe at a time and all three components B_r, B_ϕ and B_z. These rotations have a big effect on B_r and B_ϕ and the plots show a huge improvement in the residuals for these

Table 5.1: Fit results for the global geometric parameters.

	$r_{\text{off},x}$ (mm)	$r_{\text{off},y}$ (mm)	$r_{\text{off},z}$ (mm)	ψ_{bench} (°)	θ_{bench} (°)
full coil model	2.4 ± 1.1	-0.4 ± 1.4	-790.3 ± 1.3	-0.08 ± 0.07	-0.07 ± 0.07
simp. coil model	2.4 ± 8.6	-0.4 ± 0.2	-790.1 ± 0.3	-0.08 ± 0.1	-0.07 ± 0.05

Table 5.2: Fit results for the coil model parameters together with the values from the drawings.

	L_{coil} (mm)	R_{coil} (mm)	P_{coil} (mm)	I_{coil} (A)
drawings	1299.6	490.0	1.5	430.0
full coil model	1290.6 ± 1.9	487.7 ± 0.8	1.7 ± 0.4	422.8 ± 0.3
simplified coil model	1290.2 ± 0.5	490.3 ± 0.3	6.5 ± 0.9	3379.9 ± 0.1

components. See Appendix D.1 for the full coil model residuals and see Appendix D.2 for the residuals of the full coil model together with sensor card rotations. The size of the angles of a few milliradians (see Table 5.3) is consistent with the estimated precision for the mounting of the probe cards.

During the measurements probe 4 was found to be poorly mounted. This can also be seen from the large residuals for this probe. Therefore, the residuals from probe 4 were excluded from the RMS calculation.

From Table 5.4 it can be seen that there are only small differences between the full coil model and the simplified coil model. The differences between the two models are the different current densities, which leads to different fields close to the coil windings. At larger distances the differences vanish and there is no real drawback by the use of the simplified coil model.

5.3 Fourier Bessel Model

Since the coil model gives already a pretty good description of the magnetic field with only a few parameters it is used as a basis for all further calculations (in fact the simplified coil model was used). The residual field from the coil model obeys the Maxwell equations and thus can be described by a Fourier-Bessel model as shown in Chapter 3.2.2.

The FB model can be divided into three parts which have to be fitted consecutively. The sine and cosine terms in equations (3.11) to (3.13) were fitted to B_z of the high radii probes 5, 6, 11, 12, 17, 18, 23 and 24. The number of terms were set to three in ϕ-direction because of the high symmetry in ϕ, and 20 in z-direction.

The hyperbolic terms in equations (3.11) to (3.13) were fitted to all three components and all probes at the z-positions 0 and 88, which corresponds to the end surfaces of the

Table 5.3: Fit results for the three angles per Hall sensor cards.

probe	ϕ_{card} (°)	ψ_{card} (°)	θ_{card} (°)
1	-1.99 ± 0.01	-0.14 ± 0.02	0.46 ± 0.02
2	1.17 ± 0.01	-0.047 ± 0.003	0.096 ± 0.001
3	-0.84 ± 0.12	0.10 ± 0.02	0.08 ± 0.02
4	-0.78 ± 0.04	-0.016 ± 0.004	-0.83 ± 0.02
5	-0.58 ± 0.10	-0.18 ± 0.01	0.15 ± 0.02
6	-0.51 ± 0.23	-0.12 ± 0.02	0.26 ± 0.02
7	1.50 ± 0.02	-0.08 ± 0.03	0.43 ± 0.01
8	0.86 ± 0.08	0.048 ± 0.005	0.43 ± 0.02
9	0.61 ± 0.14	-0.16 ± 0.09	0.36 ± 0.02
10	0.53 ± 0.22	-0.12 ± 0.04	0.35 ± 0.04
11	0.44 ± 0.15	-0.055 ± 0.002	0.35 ± 0.019
12	0.36 ± 0.18	-0.42 ± 0.02	0.54 ± 0.03
13	1.59 ± 0.03	-0.25 ± 0.01	0.08 ± 0.02
14	1.03 ± 0.67	-0.10 ± 0.02	0.08 ± 0.09
15	0.82 ± 0.19	-0.12 ± 0.02	0.27 ± 0.02
16	0.55 ± 0.02	-0.098 ± 0.005	0.256 ± 0.008
17	0.47 ± 0.13	-0.24 ± 0.15	0.12 ± 0.02
18	0.35 ± 0.21	-0.01 ± 0.02	0.19 ± 0.02
19	-1.42 ± 0.03	0.096 ± 0.006	0.23 ± 0.02
20	-0.85 ± 0.23	-0.35 ± 0.02	0.09 ± 0.02
21	-0.65 ± 0.01	-0.035 ± 0.001	0.052 ± 0.014
22	-0.52 ± 0.25	-0.20 ± 0.03	0.12 ± 0.03
23	-0.51 ± 0.22	-0.10 ± 0.02	0.18 ± 0.02
24	-0.44 ± 0.28	-0.06 ± 0.02	0.15 ± 0.03

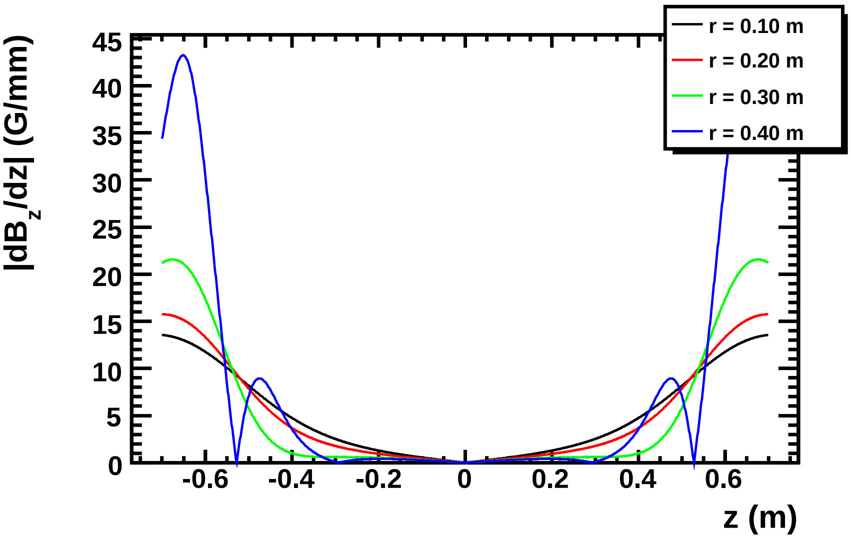

Figure 5.1: Field gradient $|dB_z/dz|$ of PCMAG. Calculated with the coil model.

measurement volume. The number of terms was set to six in r-direction and three in ϕ-direction.

The multipole terms in equations (3.12) and (3.13) were fitted to B_r of the high radii probes 5, 6, 11, 12, 17, 18, 23 and 24, which corresponds to the curved surface of a cylinder. There are three such terms because they consist only of a series in ϕ-direction.

Note that all these fields have to be added together, so in the end the residual is calculated from the sum of the coil model and the three parts of the FB model. This is achieved by the substitution $\vec{B}^{\text{mod}} = \vec{B}^{CM} + \vec{B}^{FB1} + \vec{B}^{FB2} + \vec{B}^{FB3}$ in equation (5.4). The parameters to define the volume of interest were set to $z_{\text{max}} = 900\,\text{mm}$ and $r_{\text{max}} = 450\,\text{mm}$

The residuals of the final model can be found in Appendix D.3. From these plots it can be seen that there are huge improvements on the overall shape of the residuals, especially for B_z in the inner parts of the coil. Since the field has to obey Maxwell's equations all remaining residual fields are either due to truncation effects or due to uncertainties in the probe positions. Calculating the field at a wrong position leads of course to a non-Maxwellian field. This effect is the dominant error in the high gradient parts of the PCMAG volume: $z < -0.4\,\text{m}$ and $0.4\,\text{m} < z$ (see Figure 5.1).

For the B_z it can also be seen that the residuals are worse for the lower radii probes, which is most likely due to effects seen from the NMR reference measurements and explained in Chapter 4.3.

Table 5.4: Quality indicators of the residuals for the different fits.

	RMS_{inner} (G)			RMS_{outer} (G)			RMS_{total} (G)		
	B_r	B_{phi}	B_z	B_r	B_{phi}	B_z	B_r	B_{phi}	B_z
full CM	27.8	47.2	7.3	29.1	34.3	17.8	28.3	43.0	12.2
full CM + rot	9.8	6.6	7.3	14.2	11.5	16.9	11.6	8.7	11.7
simp. CM	27.8	47.2	7.6	29.2	34.3	17.1	28.3	43.0	12.0
simp. CM + rot	11.1	6.2	7.6	13.6	9.4	15.6	12.1	7.5	11.1
CM + FB	10.5	6.1	5.7	11.6	8.8	14.7	10.9	7.2	9.9

5.4 Fit Quality Estimations

The errors for the different parameters given by MINUIT is the range in which the χ^2 changes by a value of 1. They are only quoted for completeness but have no practical use. Especially because the normalization for the χ^2 is just an estimation. They have no direct implications for the quality of the field map. Instead an estimation of the error of the field map is given by the root mean square (RMS) of the residuals. Note that the fits are mostly done on subsets of the data, while the given RMS always refers to the residuals of the complete set of data (except probe 4, see above).

In addition to the RMS from the complete set of data two additional RMS values are given: one for the inner part of the coil ($-0.4\,\mathrm{m} < z < 0.4\,\mathrm{m}$) and one for the complementary outer part of the coil ($z < -0.4\,\mathrm{m}$ and $0.4\,\mathrm{m} < z$). This was done to underline the effects of the high field gradients in the outer part of the coil.

The accuracy of the probe positions is limited for mechanical reasons. Using the strong constraints imposed by Maxwell's equations it might be possible to reconstruct the probe position from the measured field data itself to a higher precision. This would allow for lower residuals also in the high gradient parts of the coil. This will require some further studies.

An important test for the field map is to see if the value for $B_z(0,0,0)$ from the field map is the same as the value from the NMR reference measurements taken at the center of the coil (see Figure 4.4). The field map value of $B_z(0,0,0) = 9816\,\mathrm{Gauss}$ agrees perfectly with the average NMR value over the whole measurement campaign of 9815.97 Gauss. This shows that the model behaves as expected when extrapolating towards lower radii while all the parameters where obtained using measured data from the higher radii probes.

6 Final Field Map

The final field map consists of the coil models given in chapter 3.2 with the parameters set to fit the measured magnetic field best. This analytic field map can be used to calculate the magnetic field at every given point. While the coil model can be used also to calculate the field outside of PCMAG, the additions from Fourier-Bessel model are limited to the volume of PCMAG due to the nature of Laplace's equation (3.6).

The shape of the magnetic field can be seen in Figures (6.1) and (6.2) and an extrapolation of the model to the outside of PCMAG can be seen in Figure (6.3).

The error of the field map can be estimated from the RMS of the residuals and can be seen in Table 5.4. It is obvious that the uncertainty in the measurement position is the limiting factor for further improvements of the residuals in the high gradient part of the volume (see Figure 5.1).

For the use together with the TPC prototype the coordinate system of the field map has to be converted into the coordinate system of the TPC. The coordinate system of the field map is defined through a reference coordinate system which was defined during the measurement campaign at DESY by reference marks permanently installed on the hull of PCMAG. The transformations include a spatial offset as well as possible rotations, depending on the TPC position.

The field map will be provided within the analysis framework of MarlinTPC [7] and allows thus for easy access to the magnetic field values. It follows the convention of Cartesian coordinates within MarlinTPC. The field map itself is a Linear Collider Input/Output (LCIO) [6] object and thus can be saved as Linear Collider Conditions Data (LCCD) [5]. This allows saving different versions of the field map based on the validity time.

For the track reconstruction speed is usually an issue. Therefoe, an interpolation of a previously calculated field map is mostly preferred over a direct calculation most of the time. That inspired the design of the field map implementation in MarlinTPC. Four new classes are added to MarlinTPC for the magnetic field map.

MagneticField MagneticField is an interface class which provides the most important method `getMagneticField`, which takes an array of three doubles as the position in Cartesian coordinates. It returns a `BField` which is a struct of three doubles, the magnetic field values B_x, B_y and B_z. It also provides the methods to set the TPC position with respect to the reference coordinate system as well as a scale factor for the field which will come from the reference probes installed at PCMAG.

AnalyticMagneticField This class is an LCIO object and is derived from MagneticField. It provides methods to calculate the magnetic field from either the coil model or the combined final model. It also provides access to all model parameters.

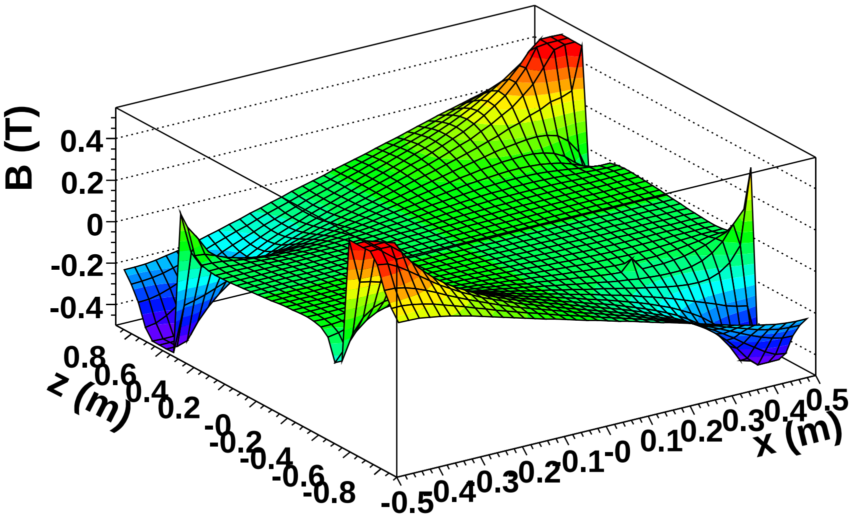

Figure 6.1: B_r field of PCMAG from the final field map.

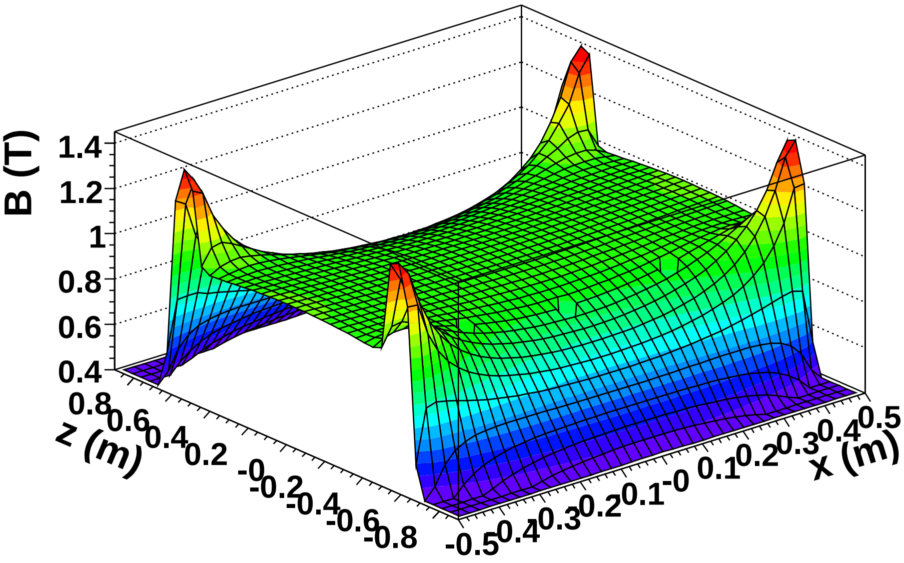

Figure 6.2: B_z field of PCMAG from the final field map.

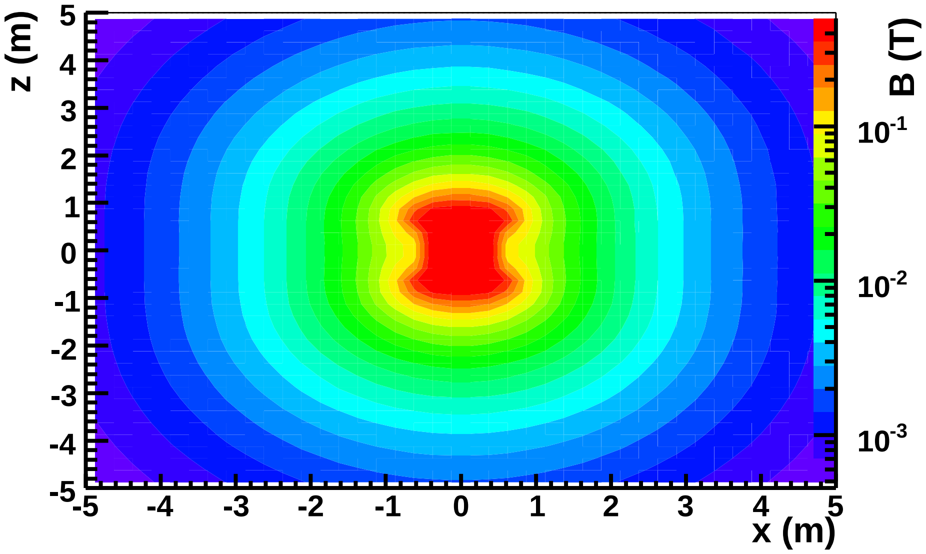

Figure 6.3: $|\vec{B}|$ outside of PCMAG from the final field map.

BinnedVectorField This class is a container class and is an LCIO object as well. It provides a three dimensional binning and stores three doubles per bin. The binning is variable and it also takes a position for the bin (0,0,0) and a length for all three directions to define the volume which is covered by the vector field. The access to the stored values can be either through the bin numbers or through a position within the defined volume. The returned value is then a linear interpolation between the eight nearest bins.

BinnedMagneticField The BinnedMagneticField class is derived from MagneticField and BinnedVectorField. The bins are filled using the methods from AnalyticMagneticField.

This structure allows for flexible use by the user. The binning can be adapted to the needed precision and the field can be calculated directly from the model as well.

7 Conclusion and Outlook

A magnetic field map for the PCMAG superconducting solenoid has been created and a model of the magnetic field is used to calculate the magnetic field at any given point. The model is based on data from a field mapping campaign and thus allows for the best possible description of the field. The error of the field map is around 5 to 10 Gauss in most parts of the magnet and thus slightly worse than expected. For the most important component, B_z, the error is 5.7 Gauss in the inner part of the coil which is still at the order of magnitude of $\sim 10^{-4}\,\mathrm{T}$.

The design of the Hall sensor cards used for the field mapping campaign was not optimal for the use in inhomogeneous fields and created the need of a lot of corrections during the analysis of the data. A cubic placement of six Hall sensors instead of three will effectively measure the magnetic field of all three components in one place. This removes the need of the individual treatment of each measured field component and will simplify the process a lot.

It turned out, that the description of the highly inhomogeneous parts of the magnet are limited by the precision of the magnetic field measurement positions. Exploiting the constraints from Maxwell's equations it might be possible to increase the accuracy of the measurement positions from the measured field data itself. Additionally high field gradients do not only require high accuracy of the measurement positions, but also high accuracy of the TPC position within the magnet. Otherwise the track reconstruction will not be correct.

The field map has been implemented into the TPC software MarlinTPC and provides the magnetic field values for the track reconstruction. The magnetic field can be calculated from the two different models introduced in this work and also allows for scaling of the field according to the measurements from reference probes installed at PCMAG. The software provides direct field calculations as well as interpolation from a pre-calculated field map in order to save time.

Dedicated drift simulation studies using the MarlinTPC software are needed in order to determine the effects of the uncertainty in the magnetic field on the accuracy of the track reconstruction. This is needed for successful testbeam activities with the large TPC prototype in late 2008.

A Euler Angles

The rotations of coordinate systems where done using euler angles in "$z\ y\ x$" convention.

$$\mathrm{X}(\theta) = \begin{pmatrix} 1 & 0 & 0 \\ 0 & \cos\theta & -\sin\theta \\ 0 & \sin\theta & \cos\theta \end{pmatrix} \tag{A.1}$$

$$\mathrm{Y}(\psi) = \begin{pmatrix} \cos\psi & 0 & \sin\psi \\ 0 & 1 & 0 \\ -\sin\psi & 0 & \cos\psi \end{pmatrix} \tag{A.2}$$

$$\mathrm{Z}(\phi) = \begin{pmatrix} \cos\phi & -\sin\phi & 0 \\ \sin\phi & \cos\phi & 0 \\ 0 & 0 & 1 \end{pmatrix} \tag{A.3}$$

$$\begin{aligned} \mathrm{R}(\phi,\psi,\theta) &= \mathrm{Z}(\phi)\mathrm{Y}(\psi)\mathrm{X}(\theta) \\ &= \begin{pmatrix} \cos\psi\cos\phi & \cos\theta\sin\psi\cos\phi - \sin\theta\sin\phi & \sin\theta\sin\phi + \cos\theta\sin\psi\cos\phi \\ \cos\psi\sin\phi & \cos\theta\cos\phi + \sin\theta\sin\psi\sin\phi & \cos\theta\sin\psi\sin\phi - \sin\theta\cos\phi \\ -\sin\psi & \sin\theta\cos\psi & \cos\theta\cos\psi \end{pmatrix} \end{aligned} \tag{A.4}$$

B Double Fourier Series

These solutions are based on [31].

B.1 Double Fourier Series

For $r = r_{\text{max}}$ and using the relation

$$\cos(\alpha + \beta) = \sin(\alpha)\sin(\beta) - \sin(\alpha)\sin(\beta) \tag{B.1}$$

the first three lines of equations (3.11), (3.12) and (3.13) can be written as a double Fourier series expansion of period 2π in ϕ-direction and $2z_{\text{max}}$ in z-direction:

$$\begin{aligned} f(\phi, z) = &\sum_{n=0}^{\infty}\sum_{l=1}^{\infty} \left[a_{nl}\cos(n\phi) + b_{nl}\sin(n\phi)\right]\cos\left(\frac{l\pi z}{z_{\text{max}}}\right) \\ &+ \sum_{n=0}^{\infty}\sum_{l=1}^{\infty} \left[c_{nl}\cos(n\phi) + d_{n,l}\sin(n\phi)\right]\sin\left(\frac{l\pi z}{z_{\text{max}}}\right) \\ &+ \sum_{n=0}^{\infty} \left[a_{n0}\cos(n\phi) + b_{n0}\sin(n\phi)\right]. \end{aligned} \tag{B.2}$$

The coefficients a_{nl} in such an expansion are given by

$$a_{00} = \frac{1}{4\pi z_{\text{max}}}\int_0^{2\pi} d\phi \int_{-2z_{\text{max}}}^{2z_{\text{max}}} f(\phi, z) dz, \tag{B.3}$$

$$a_{0l} = \frac{1}{2\pi z_{\text{max}}}\int_0^{2\pi} d\phi \int_{-2z_{\text{max}}}^{2z_{\text{max}}} f(\phi, z)\cos\left(\frac{l\pi z}{z_{\text{max}}}\right) dz, \qquad l > 0, \tag{B.4}$$

$$a_{n0} = \frac{1}{2\pi z_{\text{max}}}\int_0^{2\pi} d\phi \int_{-2z_{\text{max}}}^{2z_{\text{max}}} f(\phi, z)\cos(n\phi)\, dz, \qquad n > 0, \tag{B.5}$$

$$a_{nl} = \frac{1}{2\pi z_{\text{max}}}\int_0^{2\pi} d\phi \int_{-2z_{\text{max}}}^{2z_{\text{max}}} f(\phi, z)\cos\left(\frac{l\pi z}{z_{\text{max}}}\right)\cos(n\phi)\, dz, \qquad n, l > 0, \tag{B.6}$$

with similar expressions for the coefficients b_{nl}, c_{nl} and d_{nl} and the sine and cosine terms replaced by the according sine and cosine combination from equation (B.2).

The coefficients can then be calculated by replacing $f(\phi, z)$ with the measured field values and then using numerical integration.

B.2 Double Fourier-Bessel Series

For $z = z_{\max}$ and using again equation (B.1) the fourth and fifth line in equations (3.11), (3.12) and (3.13) can be written as

$$\begin{aligned} f(r,\phi) =& \sum_{n=1}^{\infty}\sum_{m=1}^{\infty} a_{nm}\mathrm{J}_n\left(\frac{\zeta_{nm}r}{r_{\max}}\right)\cos(n\phi) \\ &+\sum_{n=1}^{\infty}\sum_{m=1}^{\infty} b_{nm}\mathrm{J}_n\left(\frac{\zeta_{nm}r}{r_{\max}}\right)\sin(n\phi) \\ &+\sum_{m=1}^{\infty} a_{0m}\mathrm{J}_0\left(\frac{\zeta_{0m}r}{r_{\max}}\right)\cos(n\phi)\,. \end{aligned} \tag{B.7}$$

The coefficients a_{nm} and b_{nm} of such an Fourier-Bessel series expansion are given by

$$a_{nm} =\frac{2}{r_{\max}^2\mathrm{J}_{n+1}^2\left(\zeta_{nm}\right)\pi}\int_0^{r_{\max}} dr\int_0^{2\pi} d\phi r f(\phi,z)\cos(n\phi)\,\mathrm{J}_n^2\left(\frac{\zeta_{nm}r}{r_{\max}}\right),\quad n>0, \tag{B.8}$$

$$b_{nm} =\frac{2}{r_{\max}^2\mathrm{J}_{n+1}^2\left(\zeta_{nm}\right)\pi}\int_0^{r_{\max}} dr\int_0^{2\pi} d\phi r f(\phi,z)\sin(n\phi)\,\mathrm{J}_n^2\left(\frac{\zeta_{nm}r}{r_{\max}}\right),\quad n>0, \tag{B.9}$$

$$a_{nm} =\frac{2}{r_{\max}^2\mathrm{J}_1^2\left(\zeta_{0m}\right)\pi}\int_0^{r_{\max}} dr\int_0^{2\pi} d\phi r f(\phi,z)\mathrm{J}_0^2\left(\frac{\zeta_{nm}r}{r_{\max}}\right). \tag{B.10}$$

Again the coefficients can be calculated by integrating over the respective hyperplane and by replacing $f(r,\phi)$ with the measured field values.

Note that all ϕ-independent parts of $f(r,\phi)$ are removed through integration around ϕ.

C Offset Measurement Plots

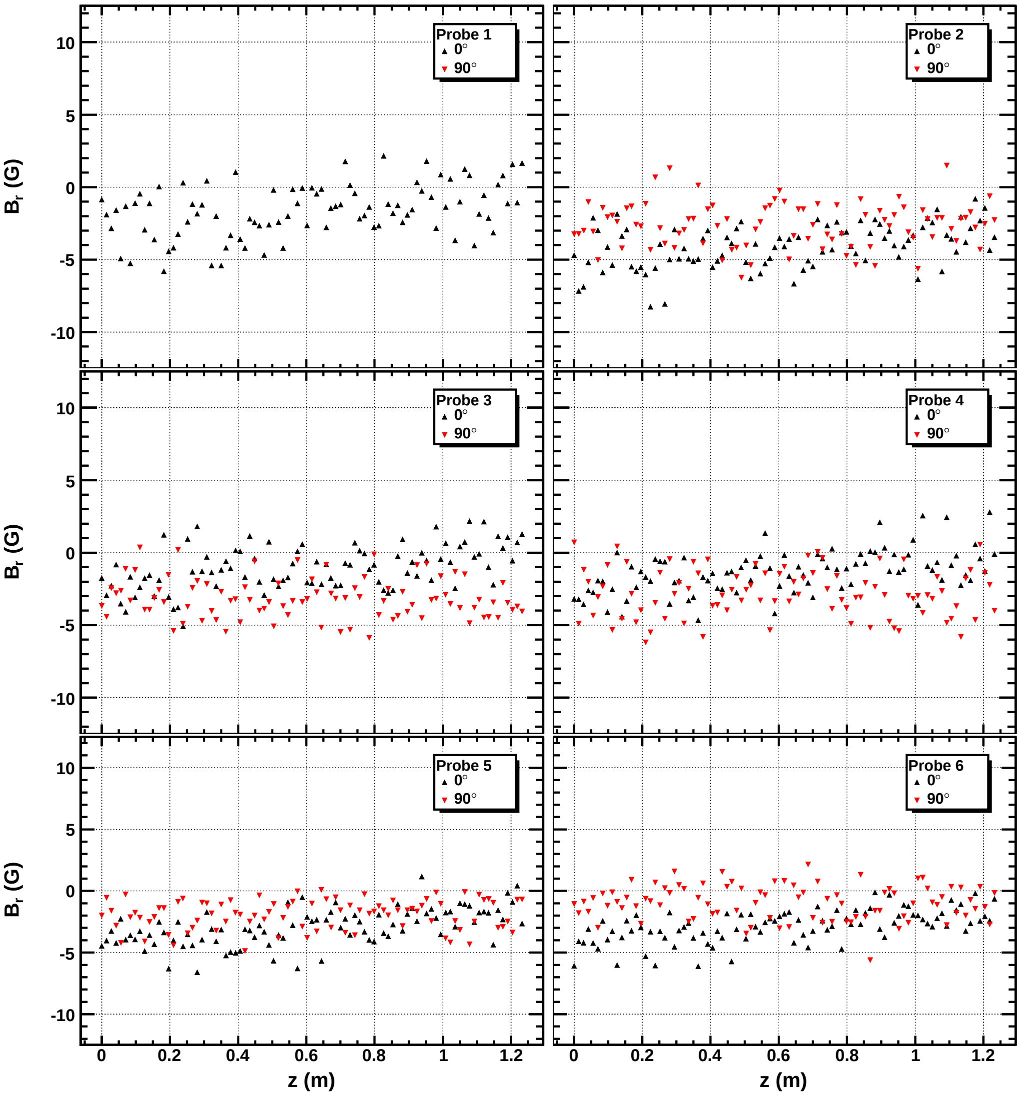

Figure C.1: Offset measurements for B_r probes 1-6.

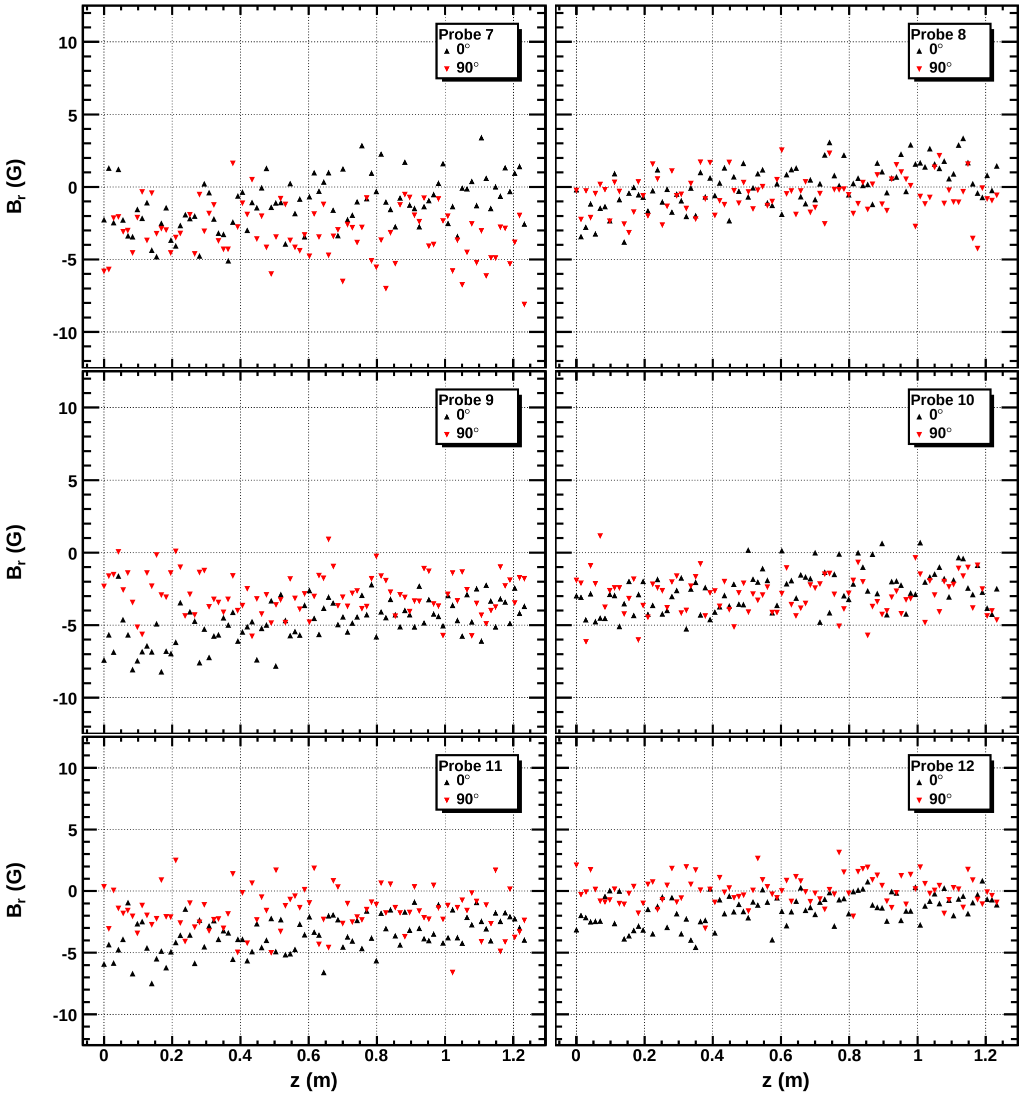

Figure C.2: Offset measurements for B_r probes 7-12.

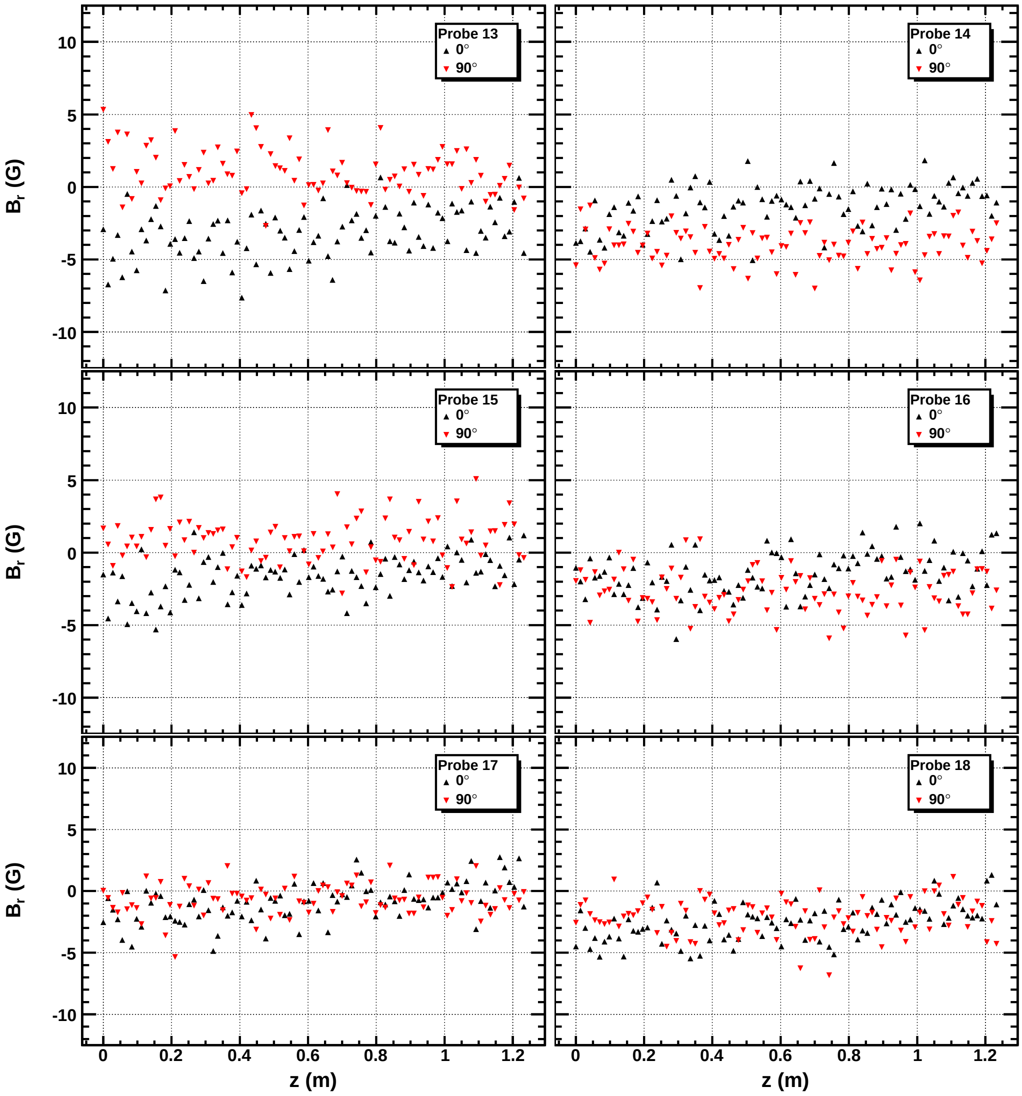

Figure C.3: Offset measurements for B_r probes 13-18.

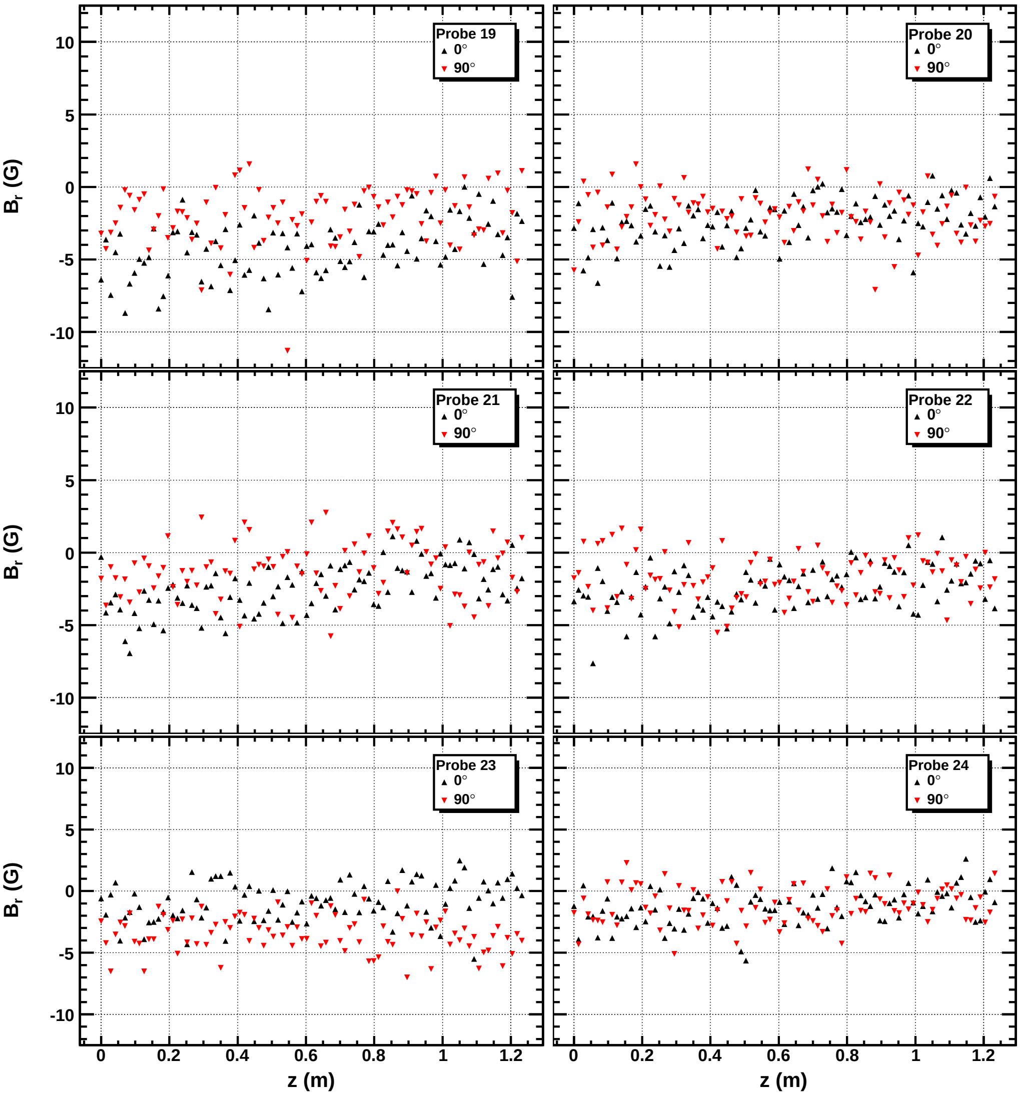

Figure C.4: Offset measurements for B_r probes 19-24.

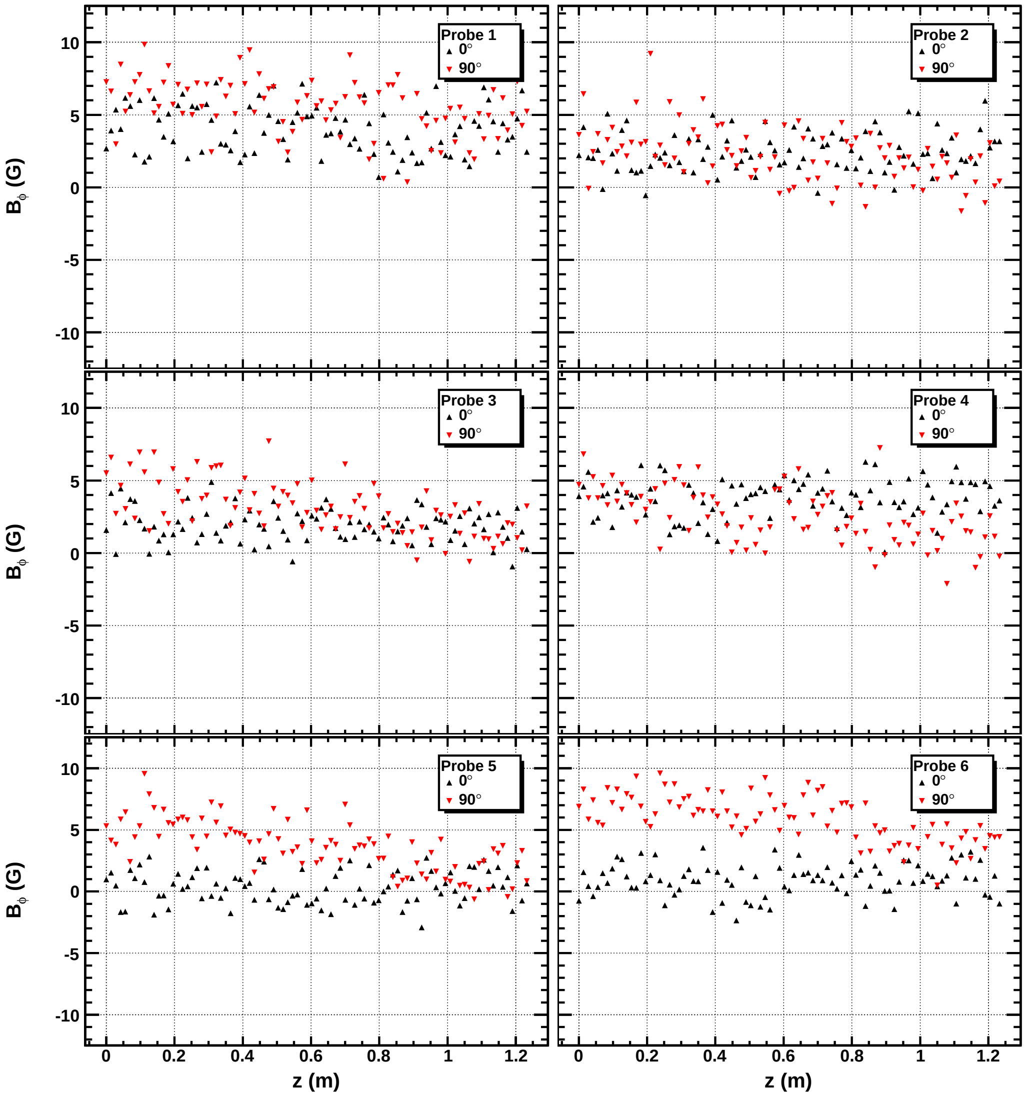

Figure C.5: Offset measurements for B_ϕ probes 1-6.

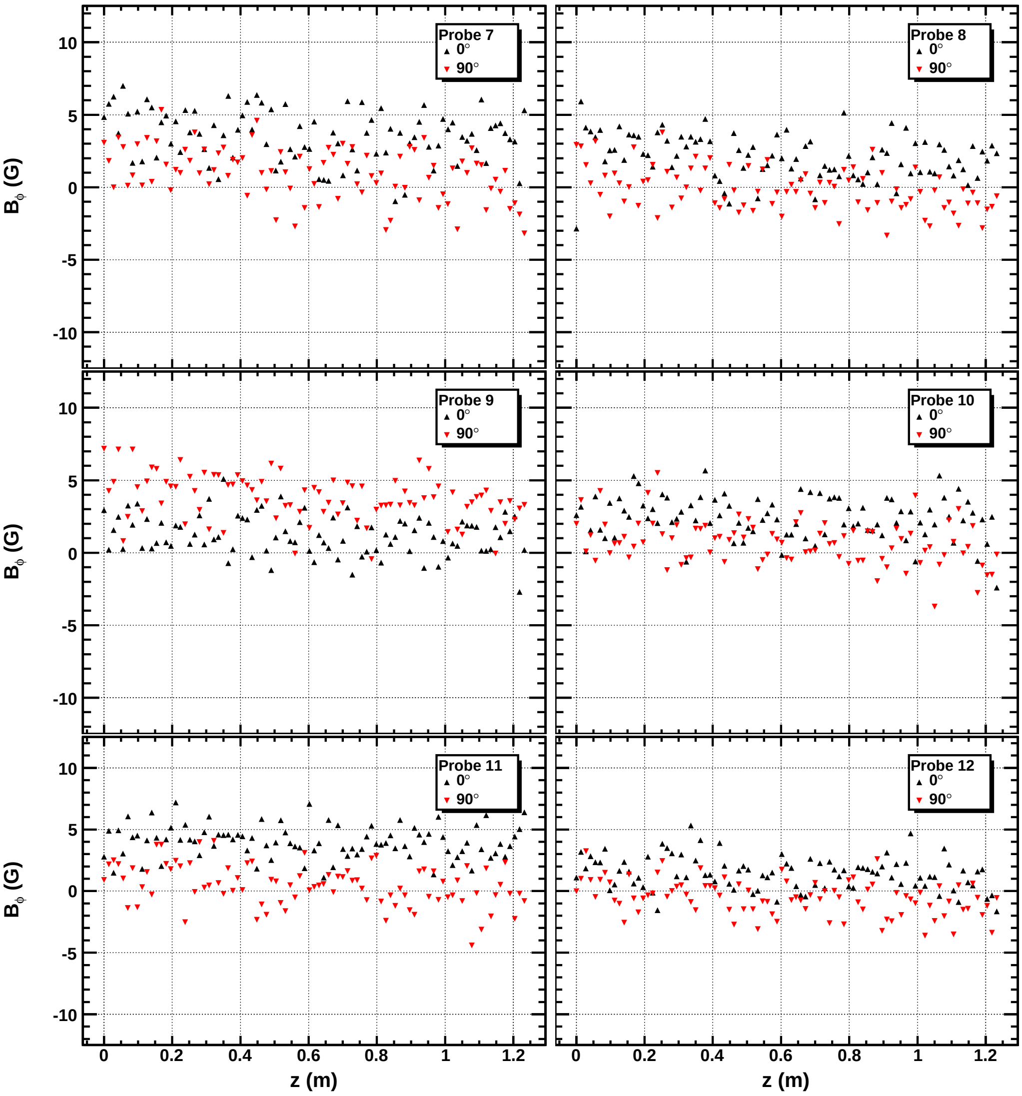

Figure C.6: Offset measurements for B_ϕ probes 7-12.

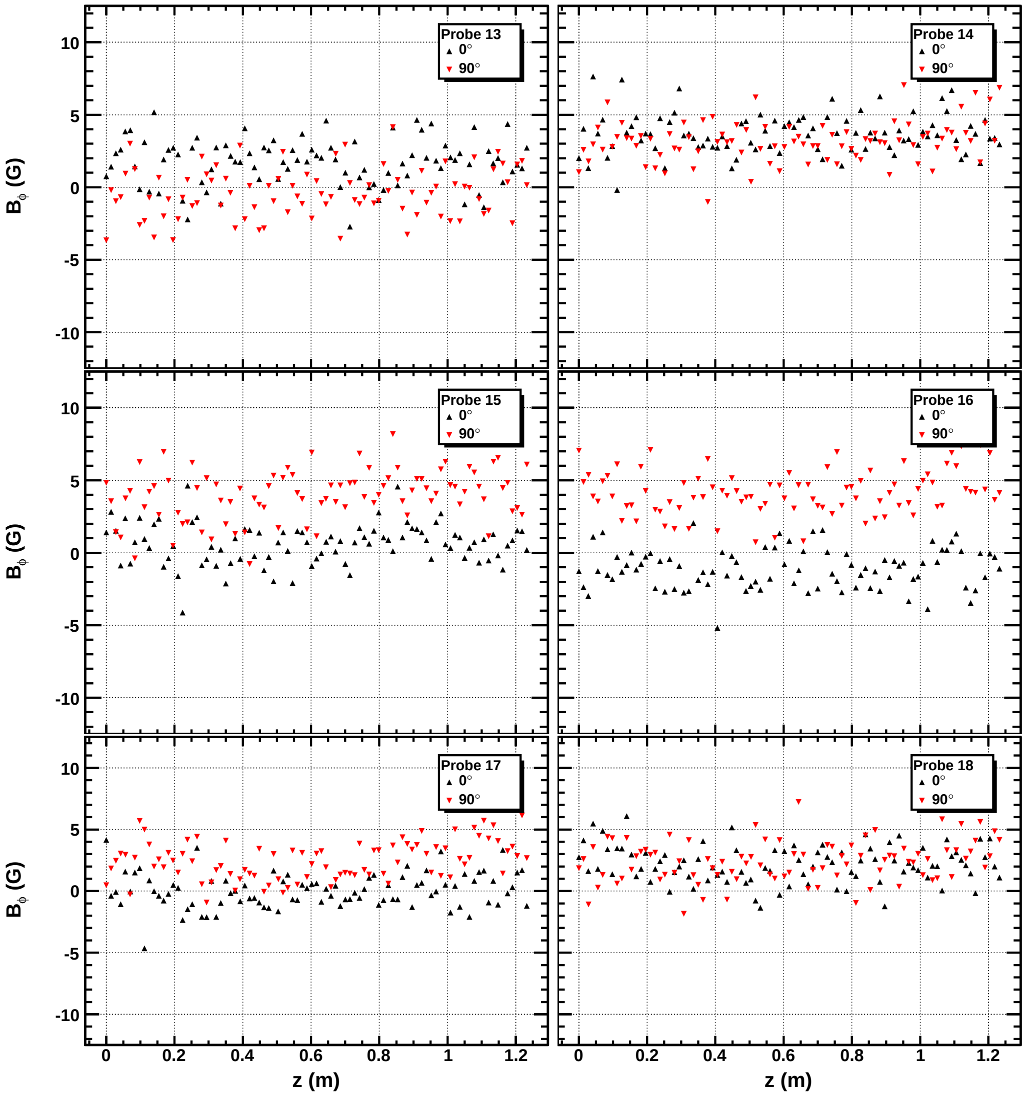

Figure C.7: Offset measurements for B_ϕ probes 13-18.

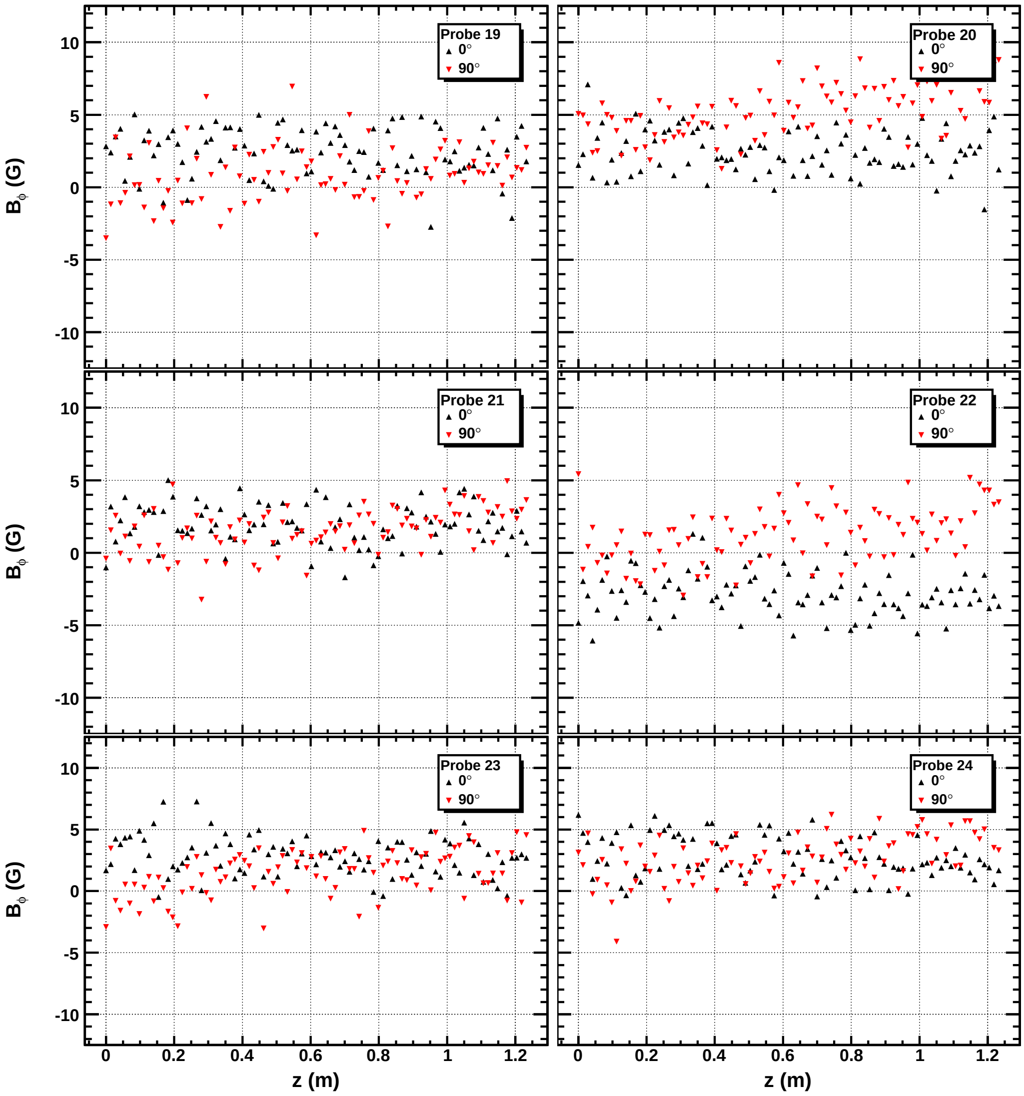

Figure C.8: Offset measurements for B_ϕ probes 19-24.

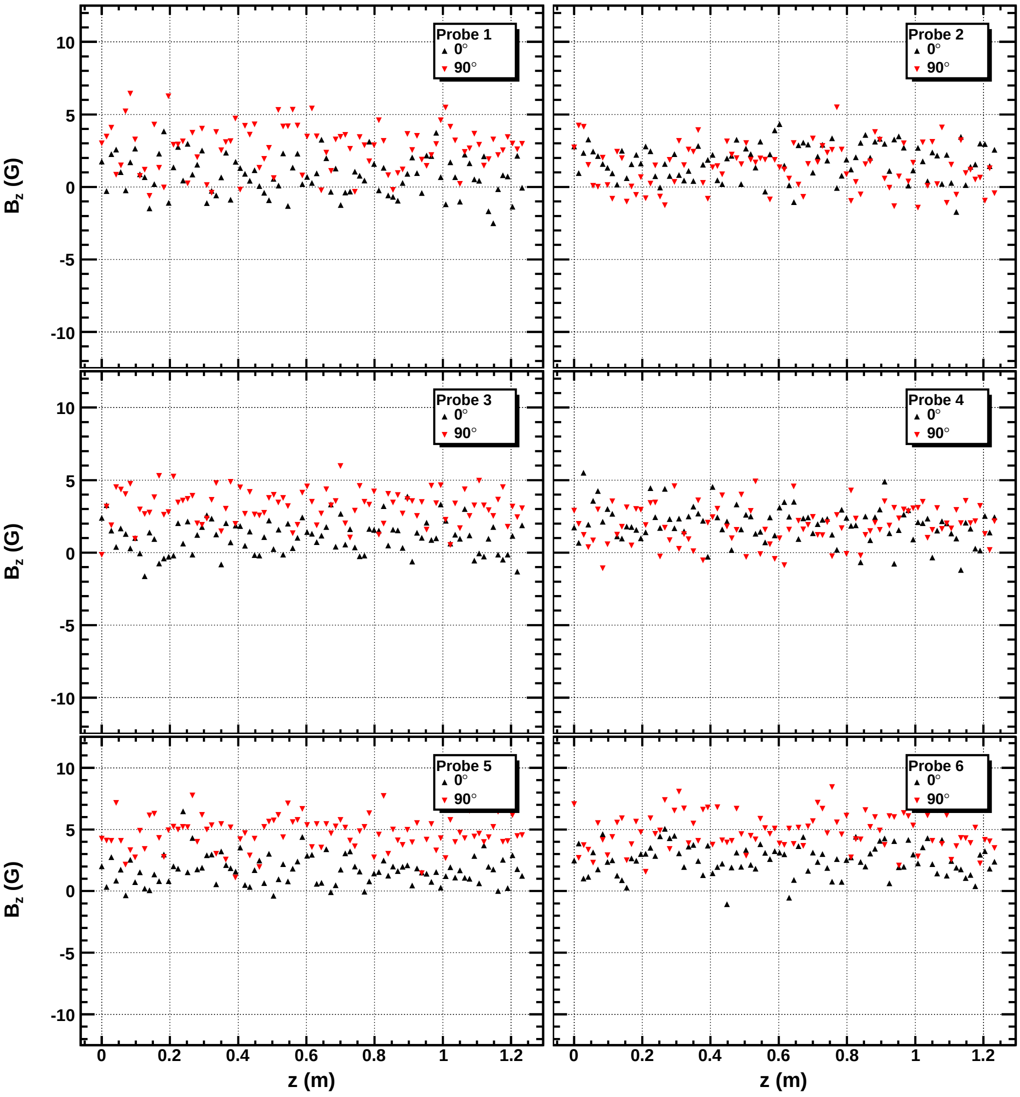

Figure C.9: Offset measurements for B_z probes 1-6.

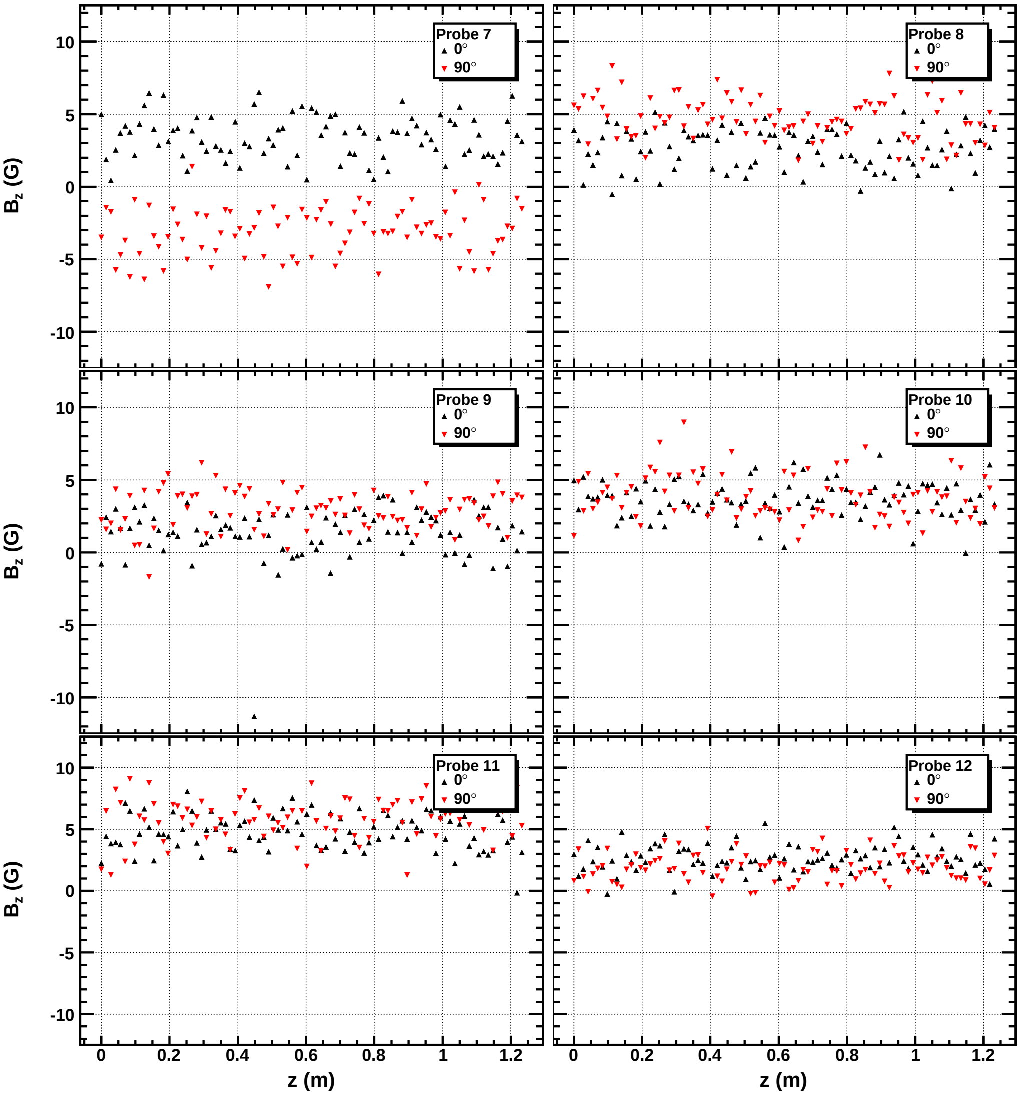

Figure C.10: Offset measurements for B_z probes 7-12.

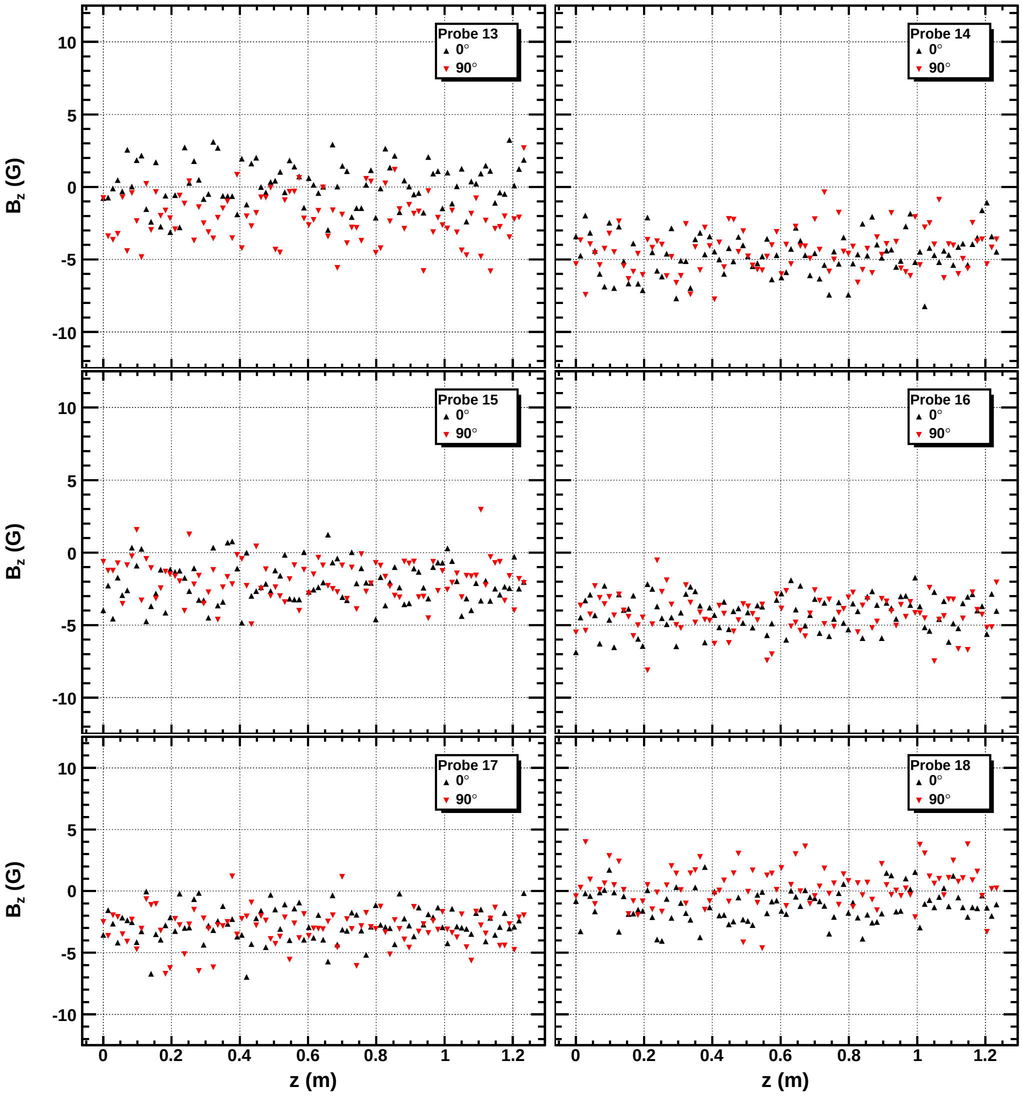

Figure C.11: Offset measurements for B_z probes 13-18.

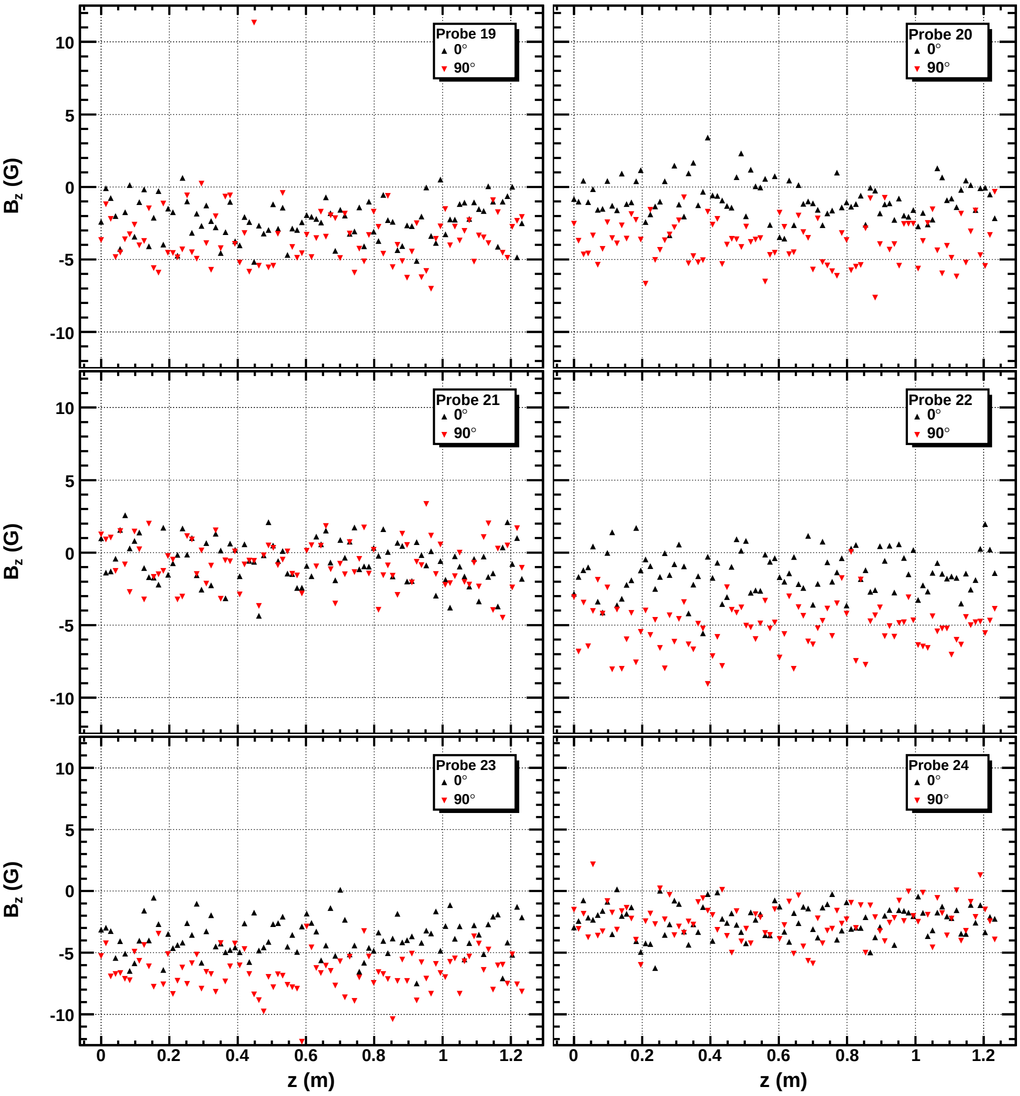

Figure C.12: Offset measurements for B_z probes 19-24.

D Residual Plots

D.1 Full Coil Model

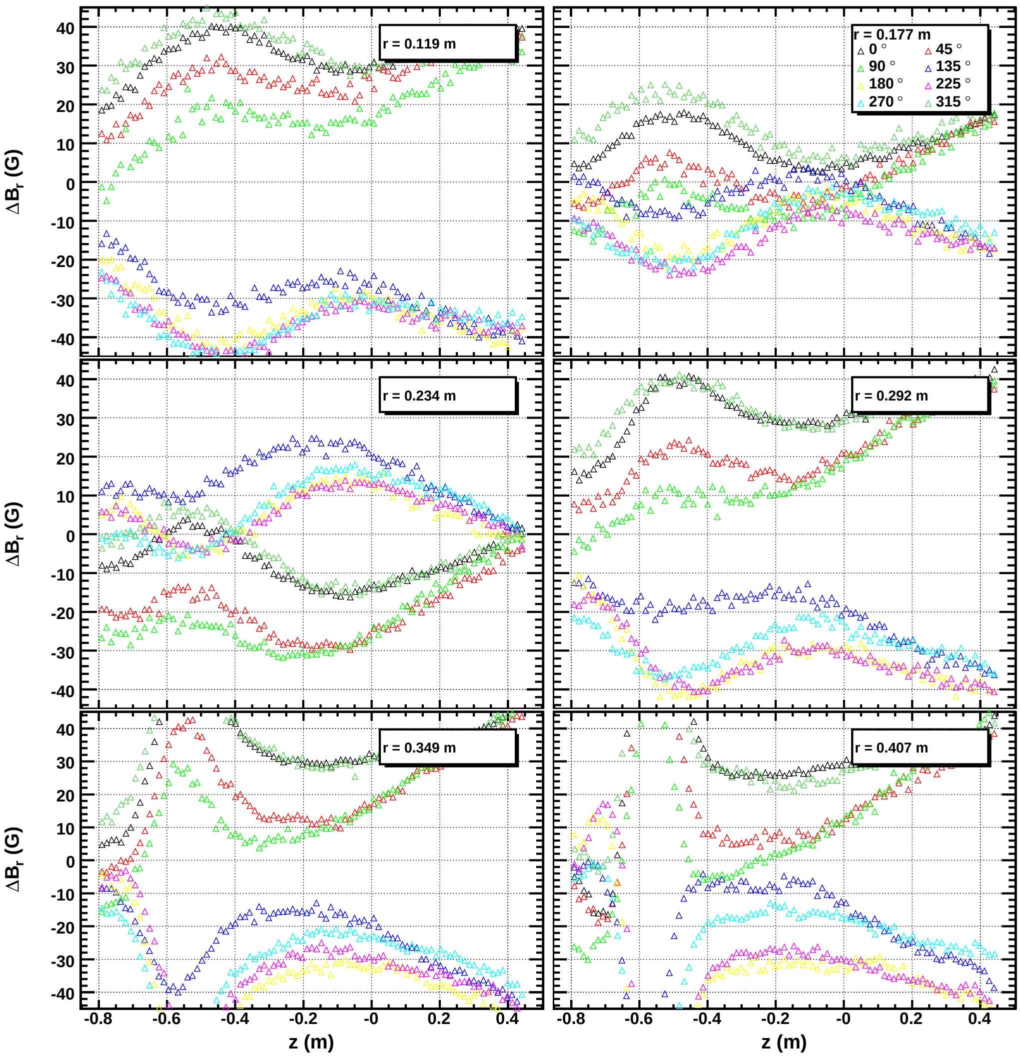

Figure D.1: Residuals for B_r probes 1-6 and full coil model.

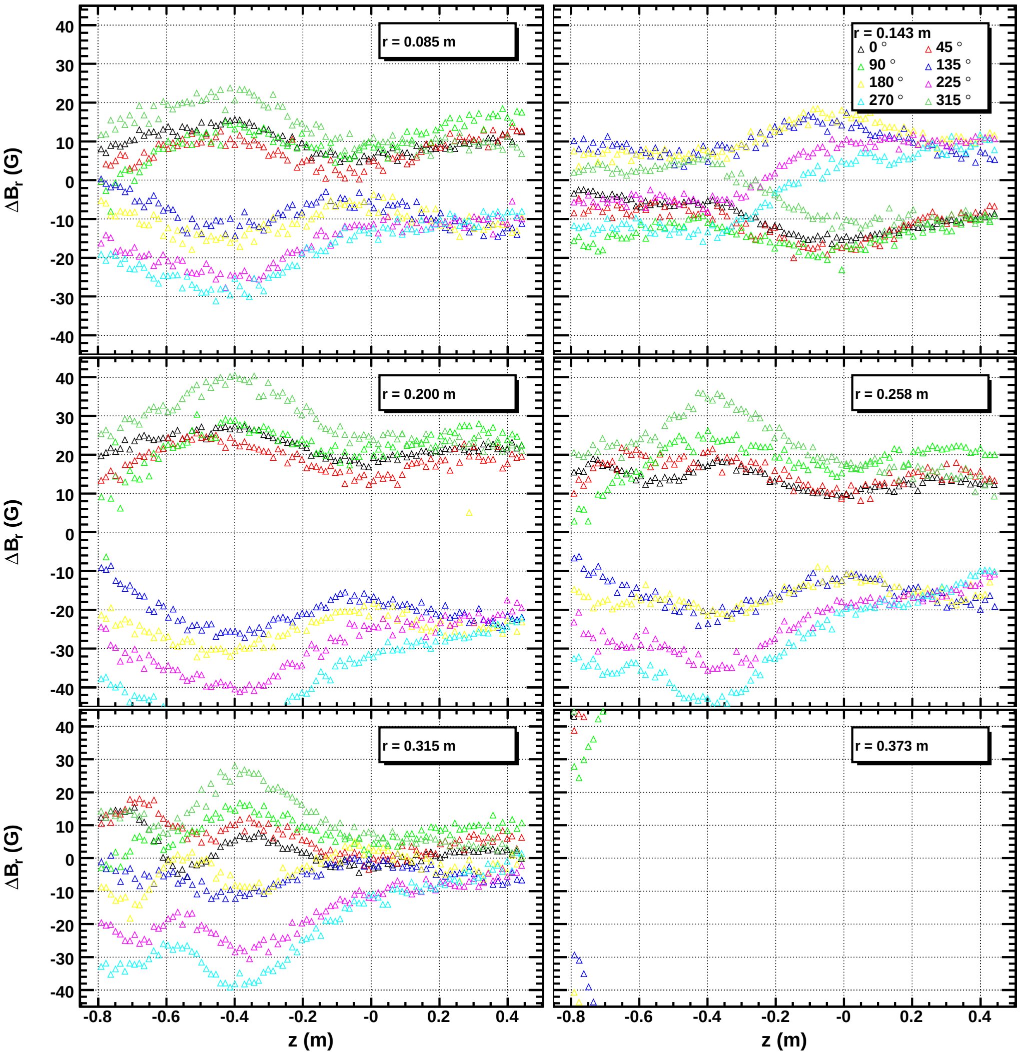

Figure D.2: Residuals for B_r probes 7-12 and full coil model.

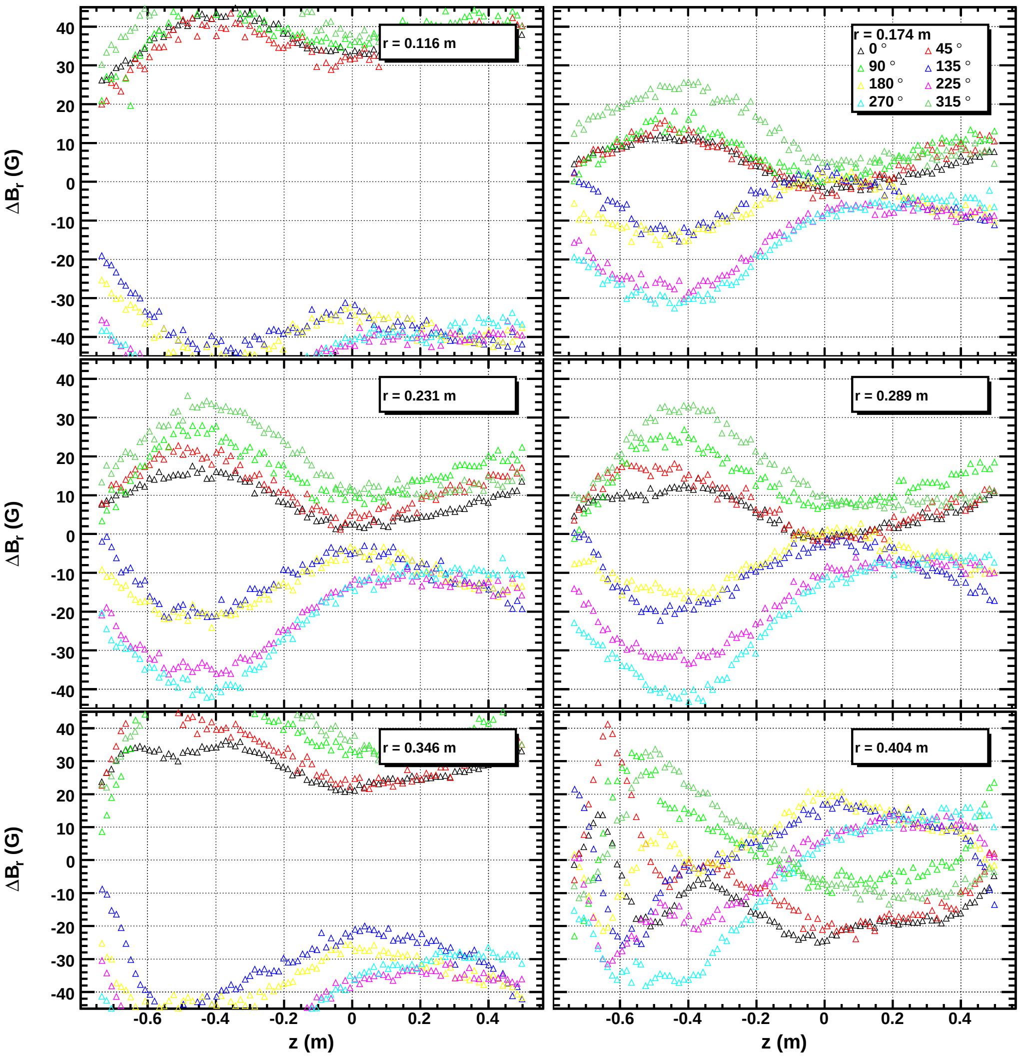

Figure D.3: Residuals for B_r probes 13-18 and full coil model.

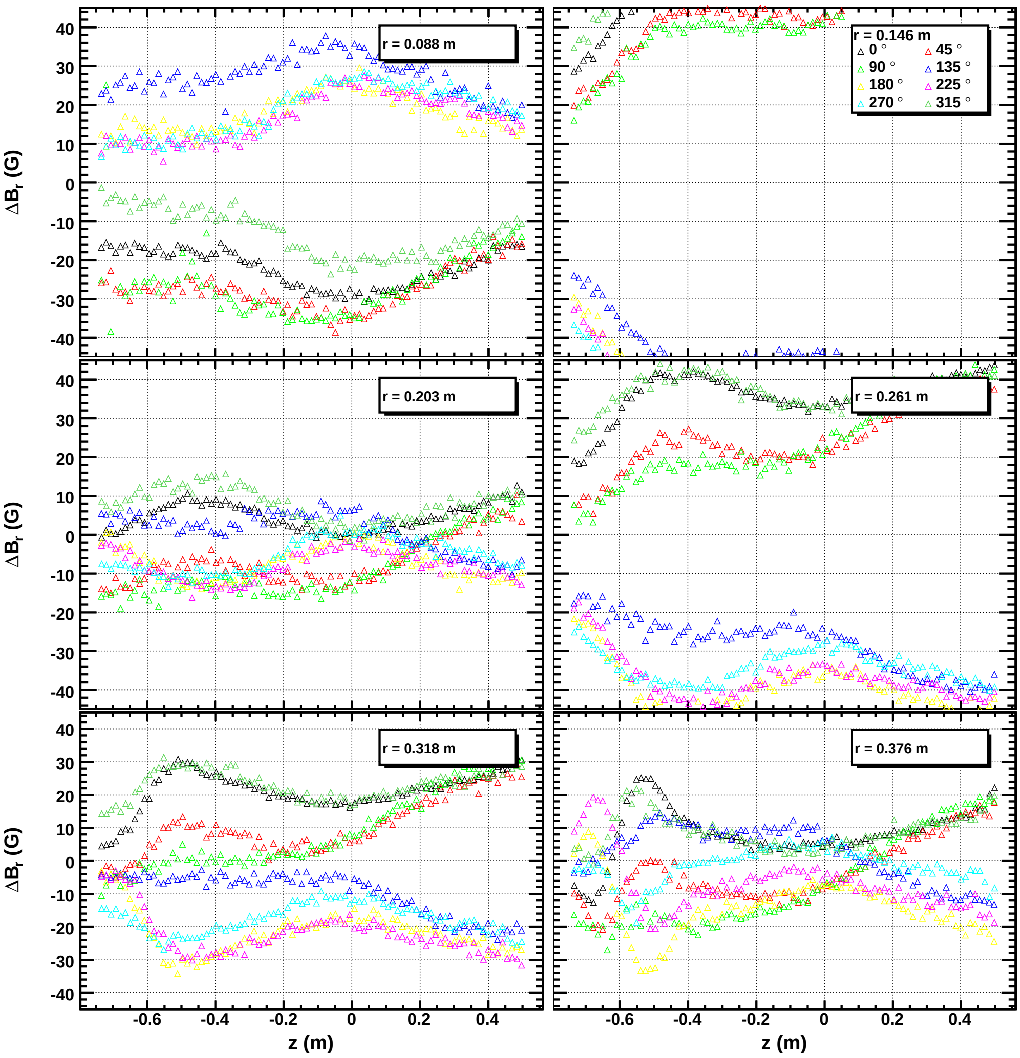

Figure D.4: Residuals for B_r probes 19-24 and full coil model.

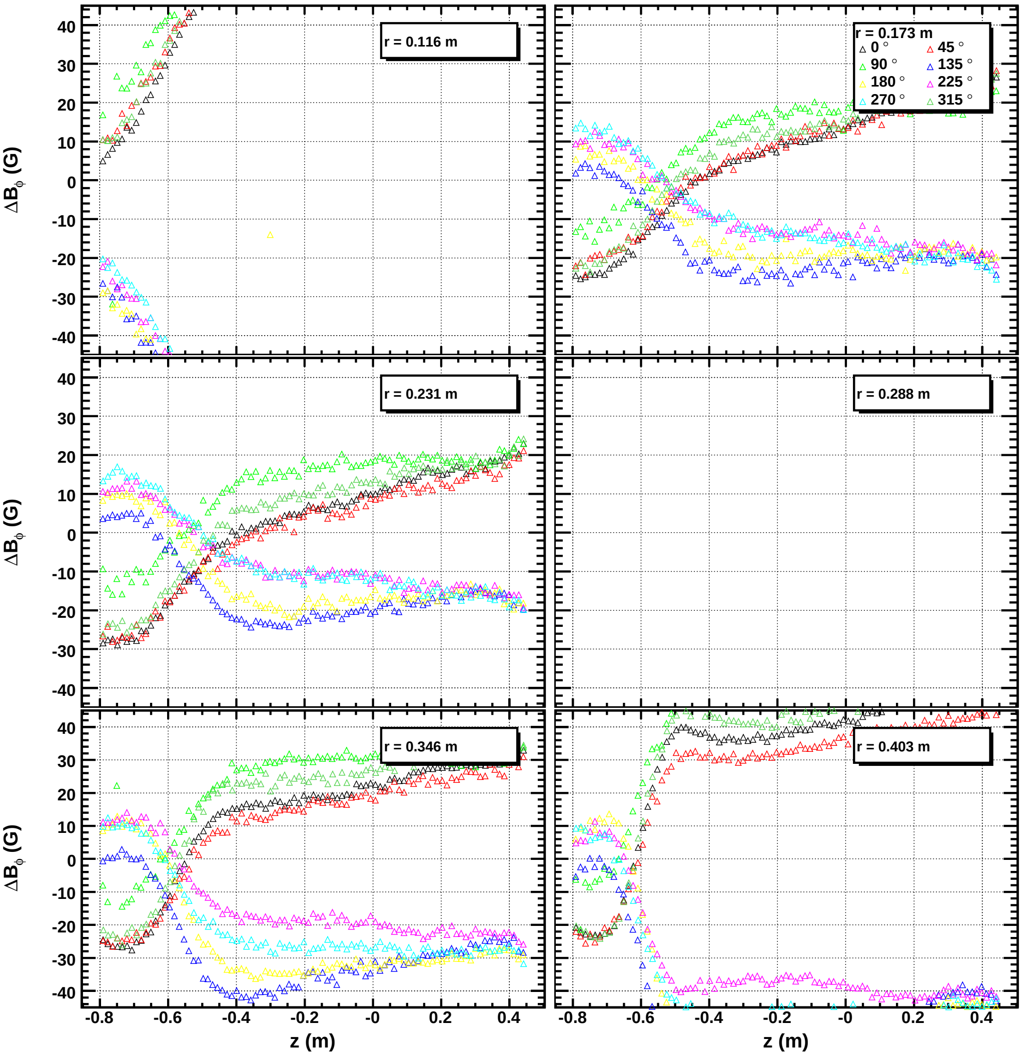

Figure D.5: Residuals for B_ϕ probes 1-6 and full coil model.

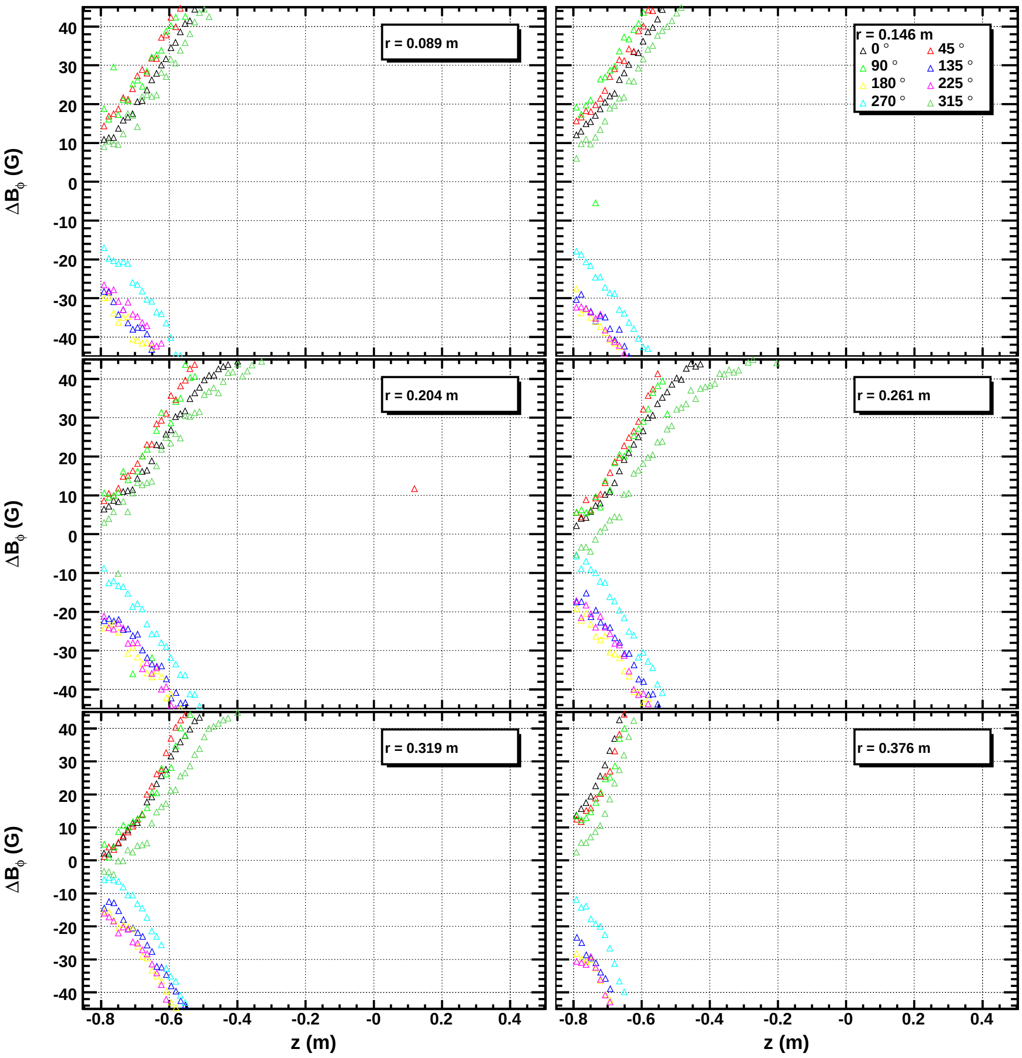

Figure D.6: Residuals for B_ϕ probes 7-12 and full coil model.

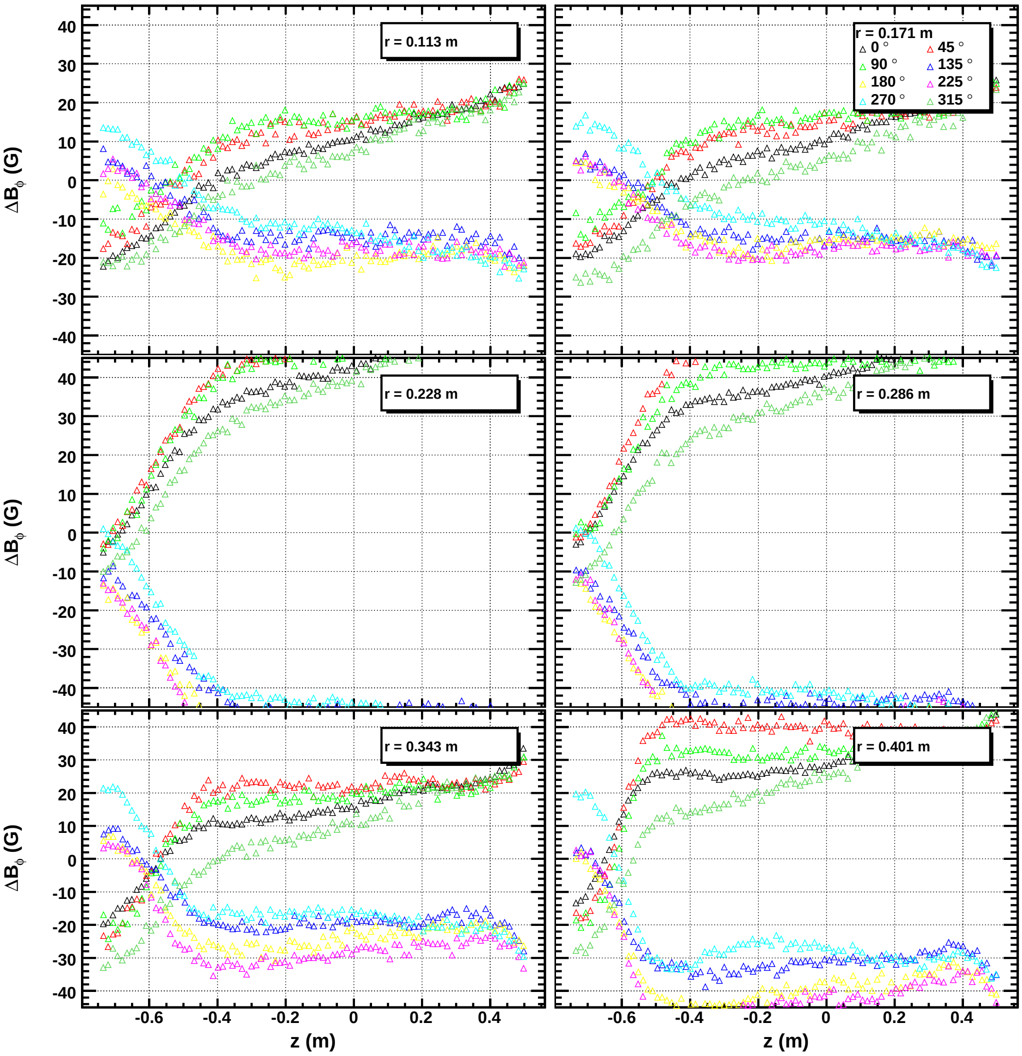

Figure D.7: Residuals for B_ϕ probes 13-18 and full coil model.

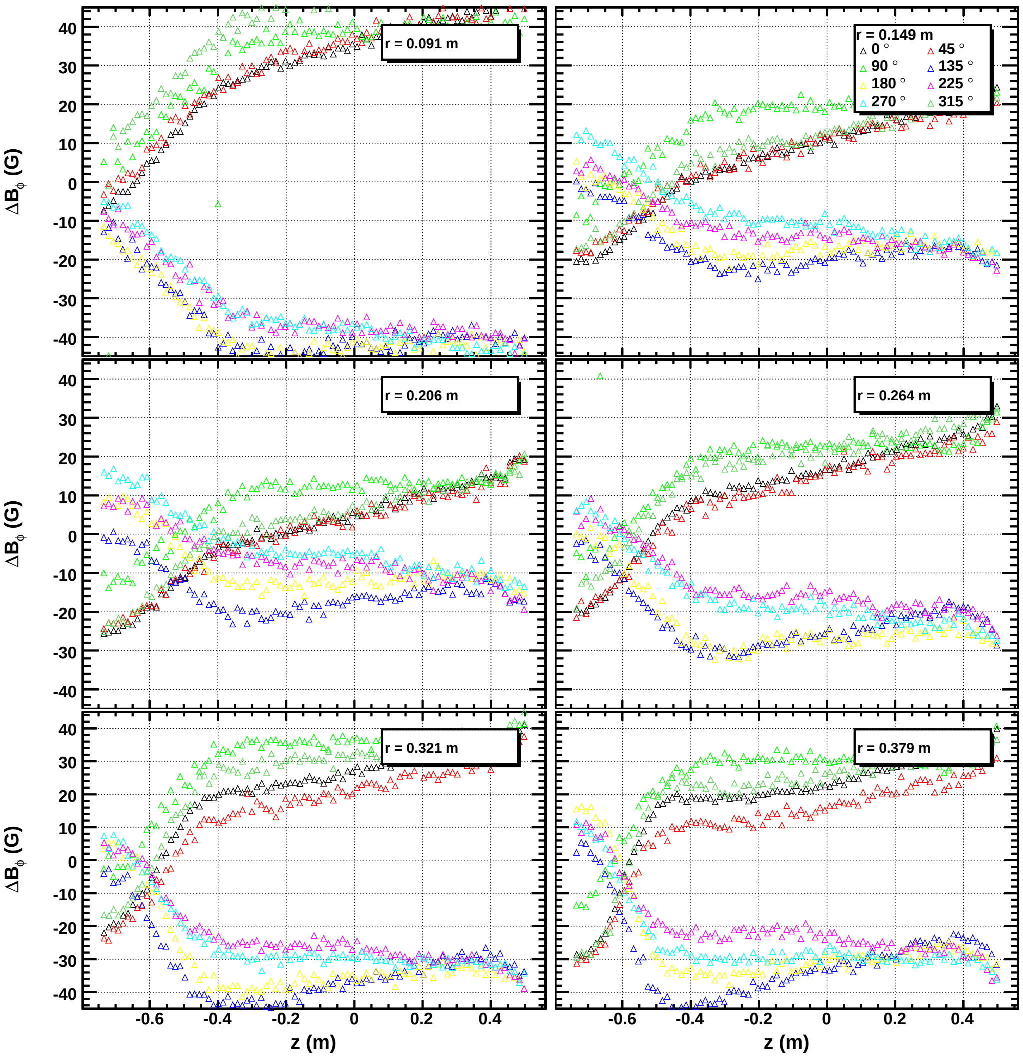

Figure D.8: Residuals for B_ϕ probes 19-24 and full coil model.

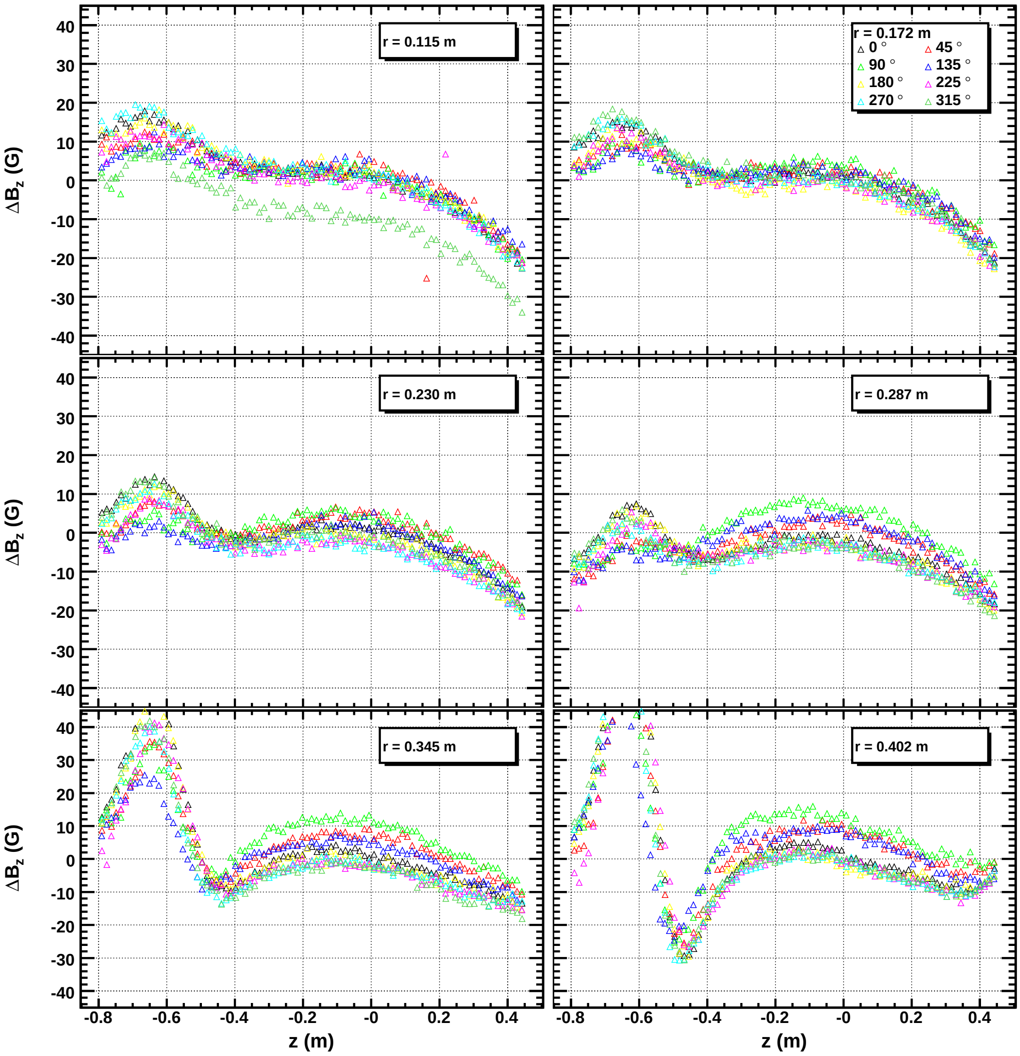

Figure D.9: Residuals for B_z probes 1-6 and full coil model.

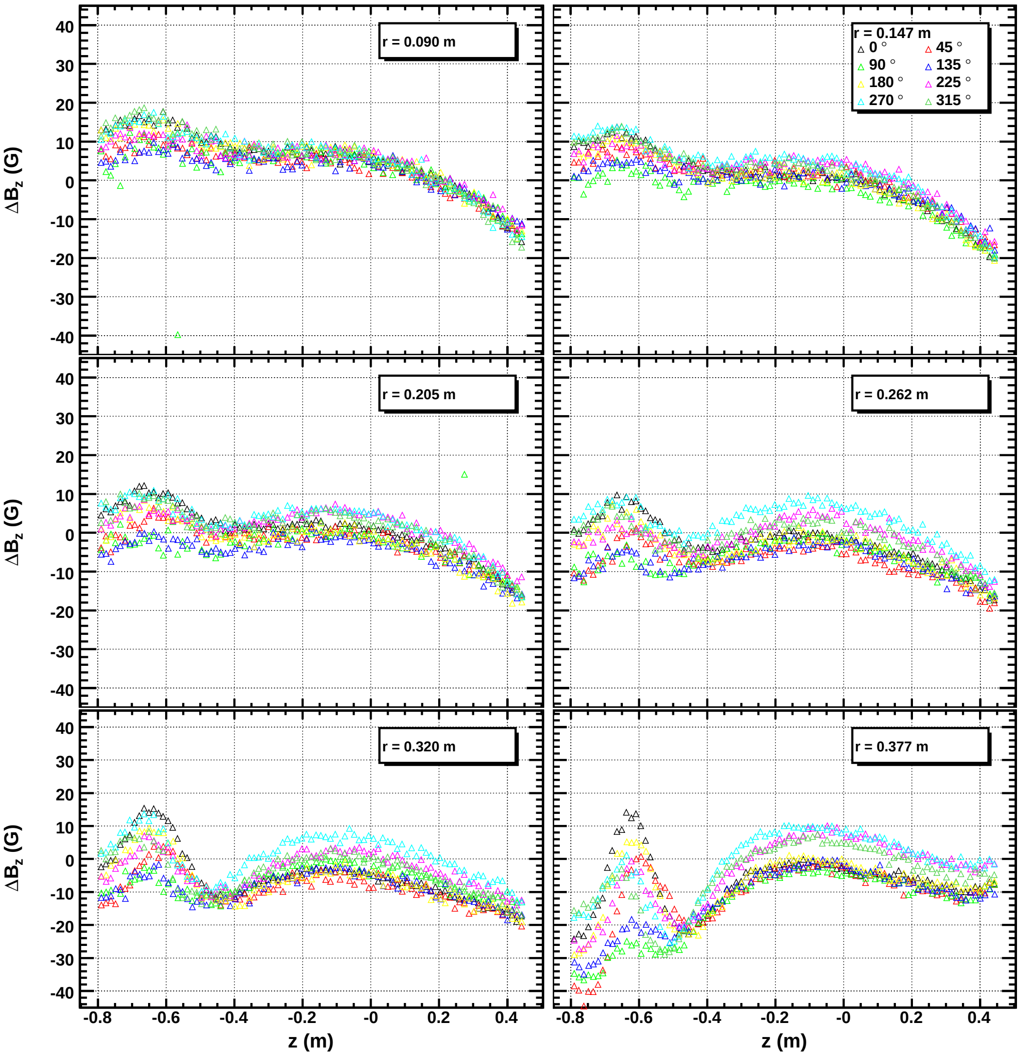

Figure D.10: Residuals for B_z probes 7-12 and full coil model.

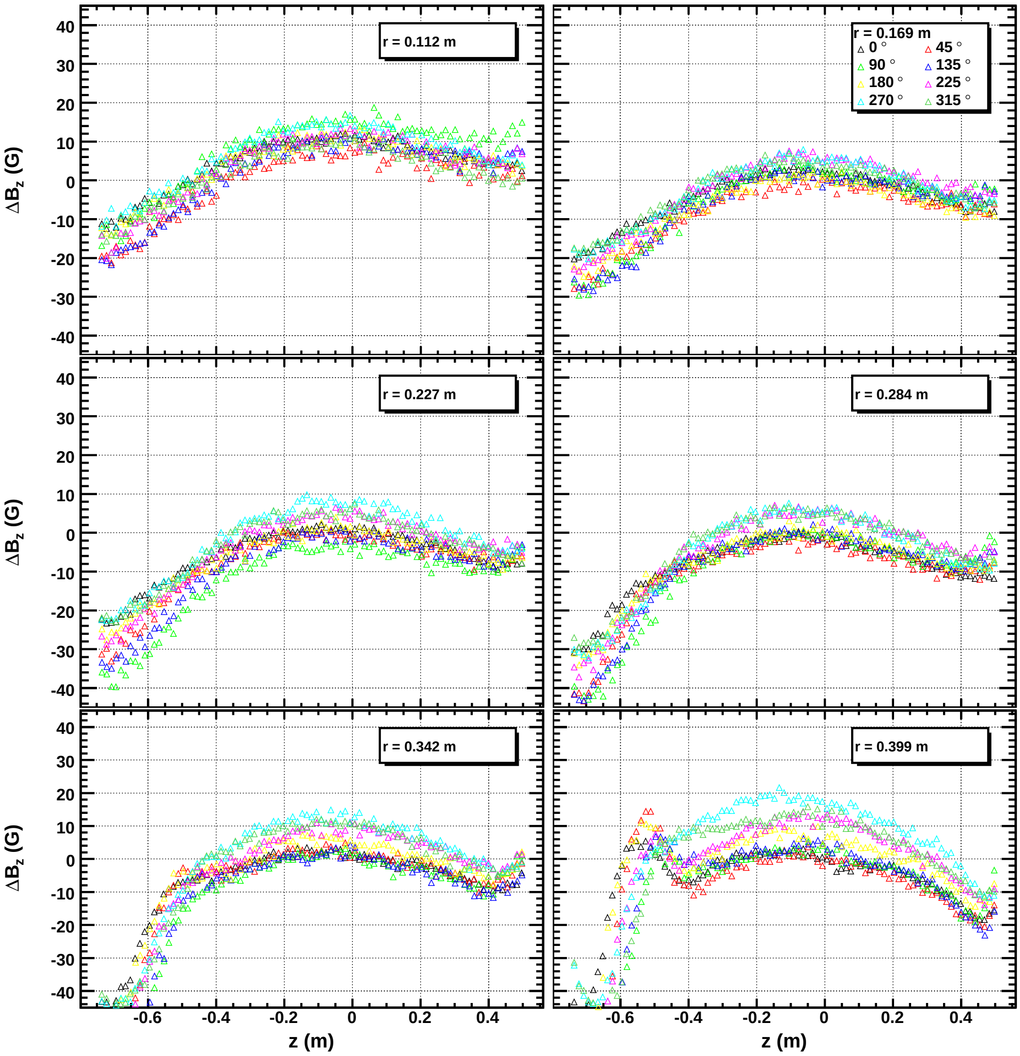

Figure D.11: Residuals for B_z probes 13-18 and full coil model.

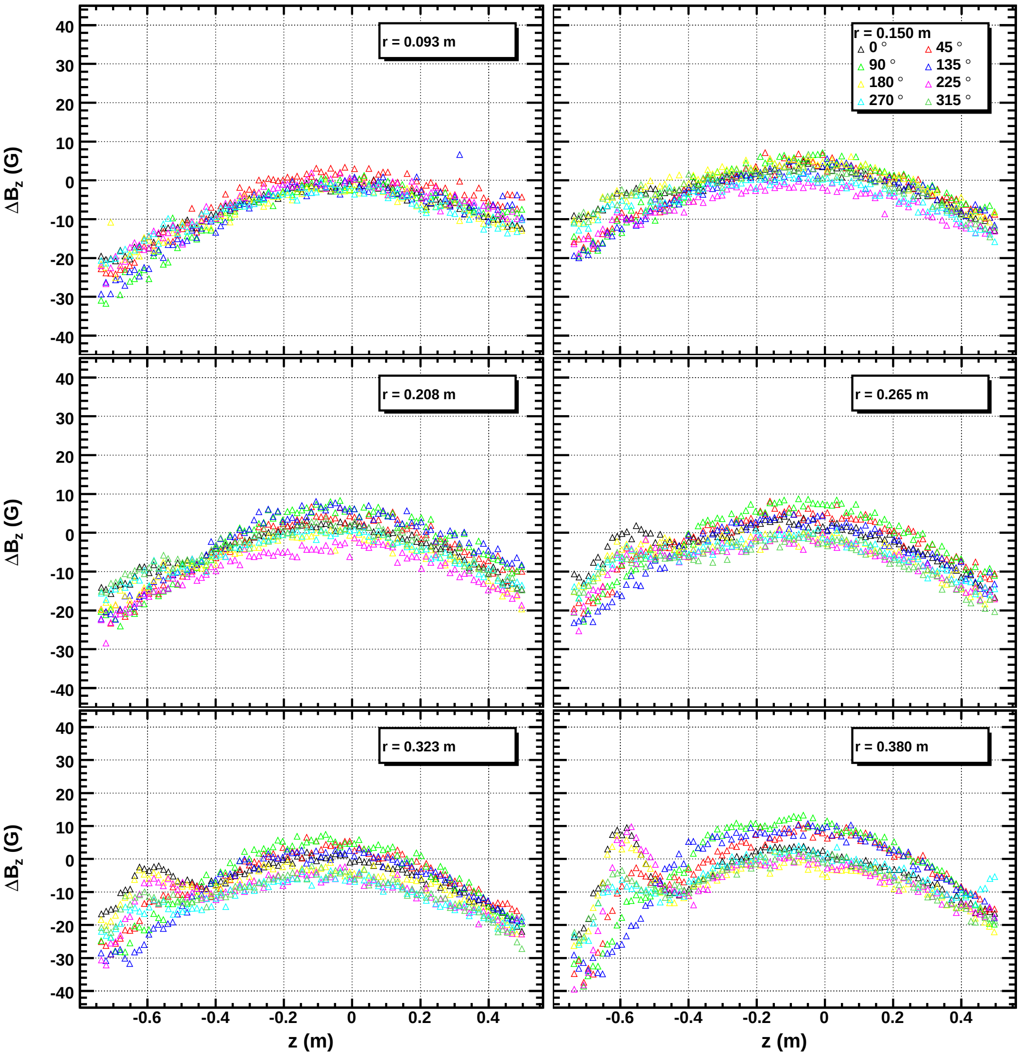

Figure D.12: Residuals for B_z probes 19-24 and full coil model.

D.2 Full Coil Model with Sensor Card Rotations

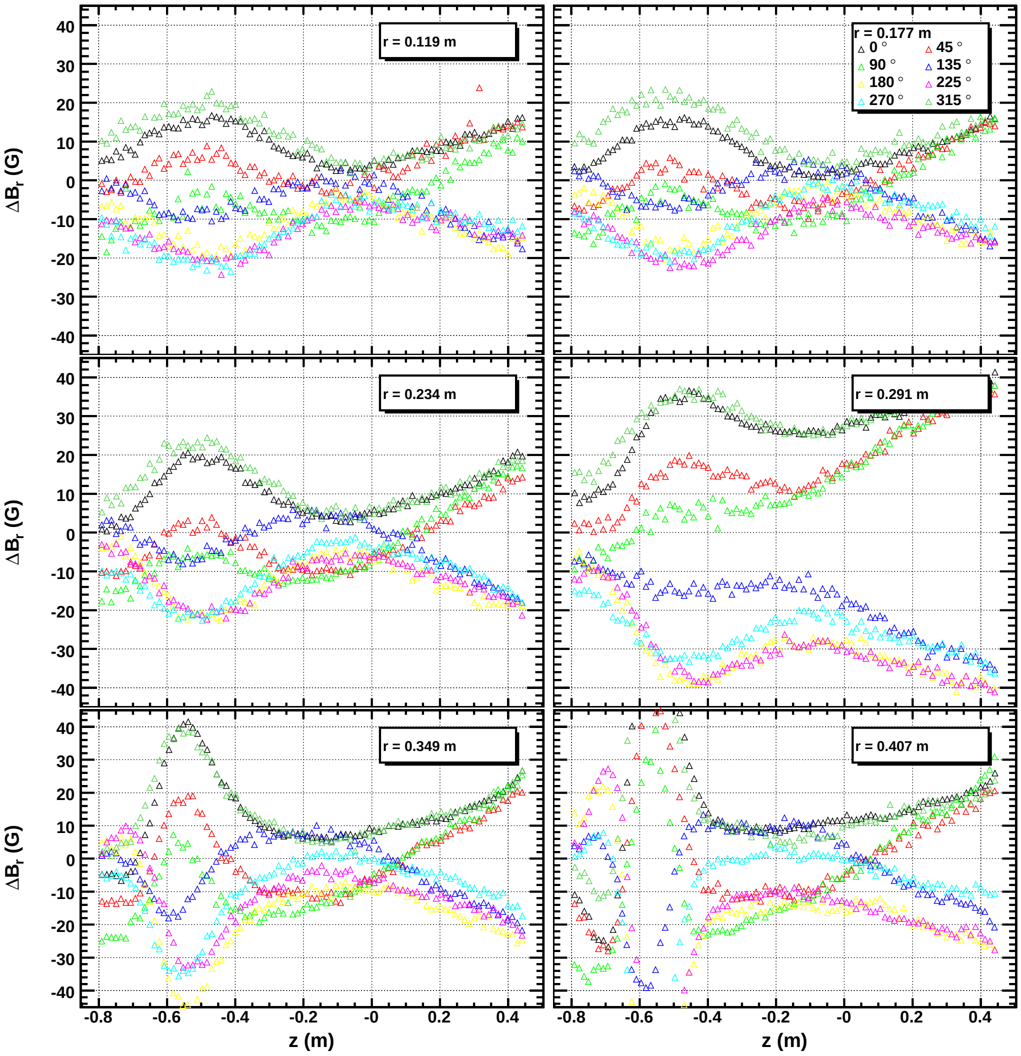

Figure D.13: Residuals for B_r probes 1-6 and full coil model together with Hall sensor card rotations.

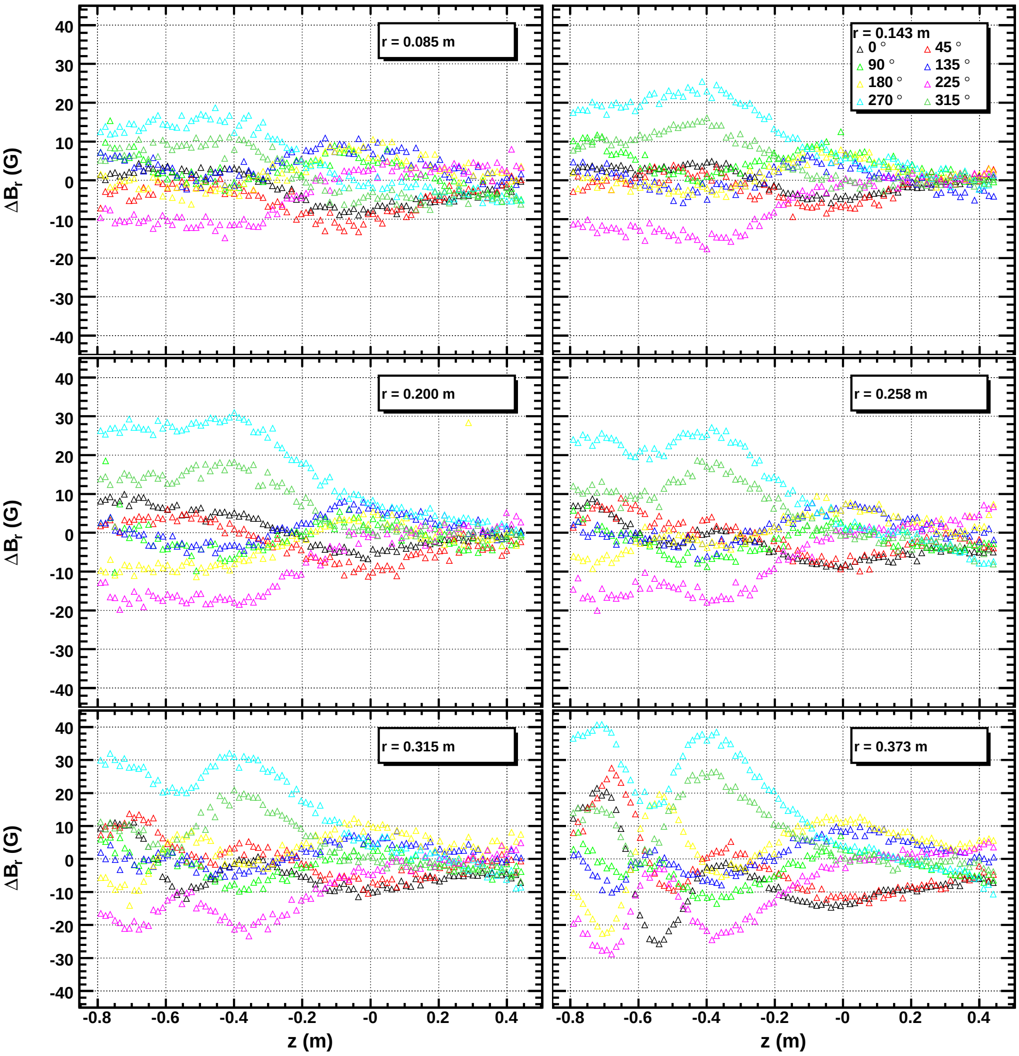

Figure D.14: Residuals for B_r probes 7-12 and full coil model together with Hall sensor card rotations.

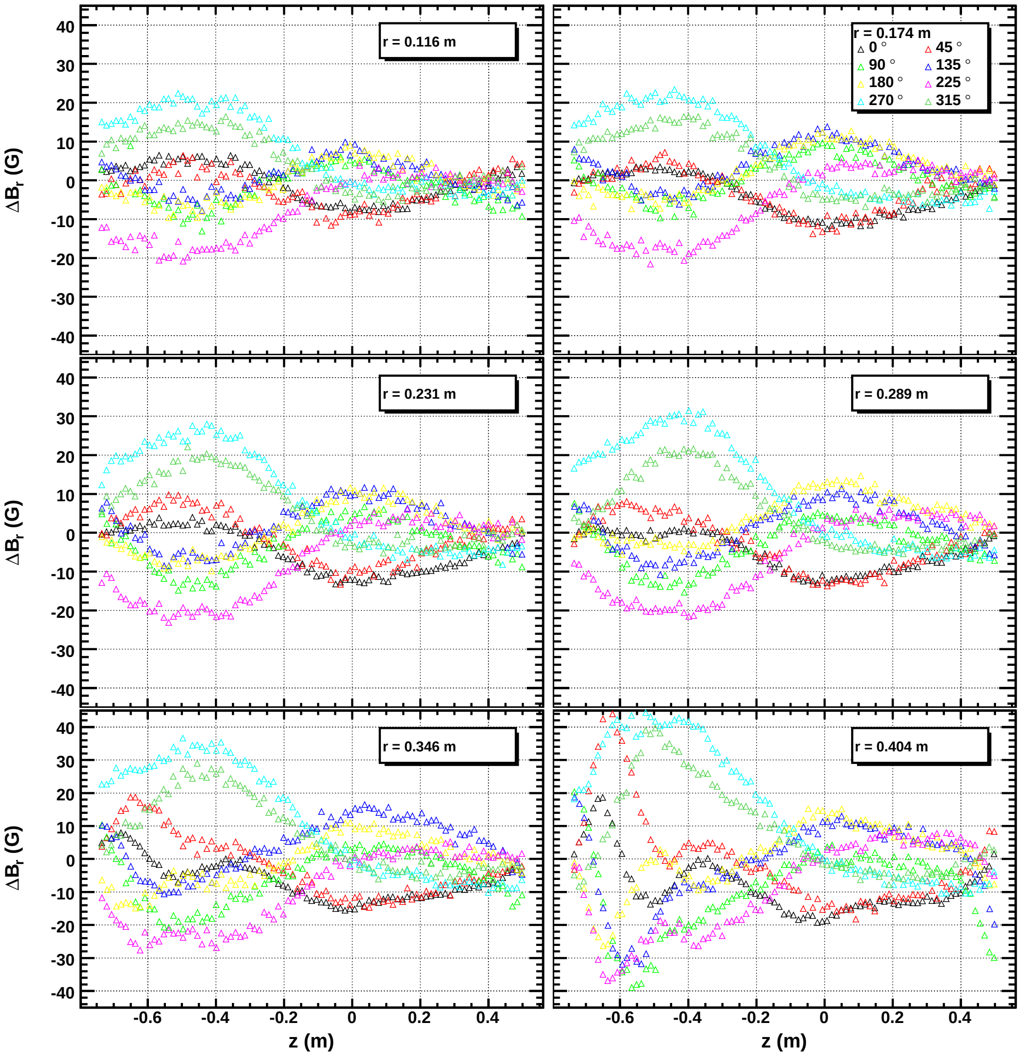

Figure D.15: Residuals for B_r probes 13-18 and full coil model together with Hall sensor card rotations.

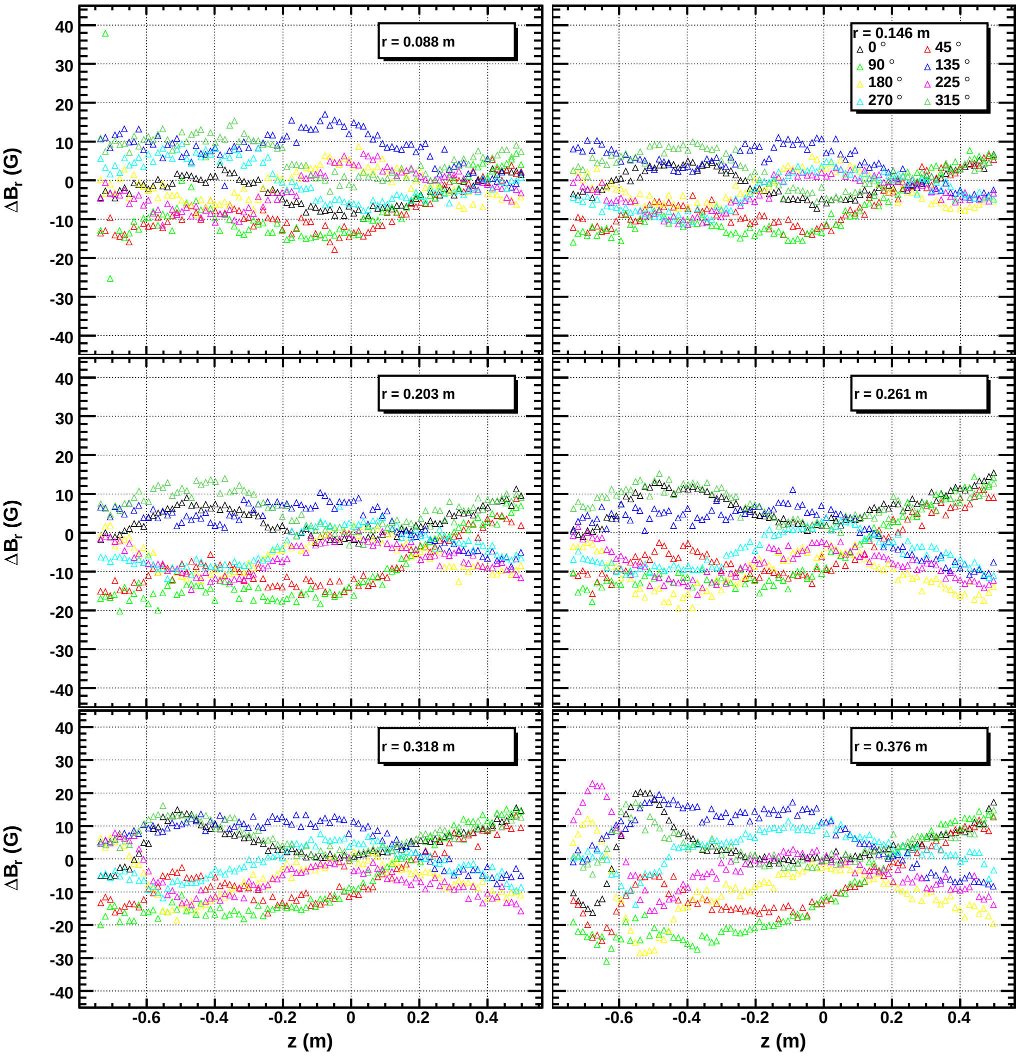

Figure D.16: Residuals for B_r probes 19-24 and full coil model together with Hall sensor card rotations.

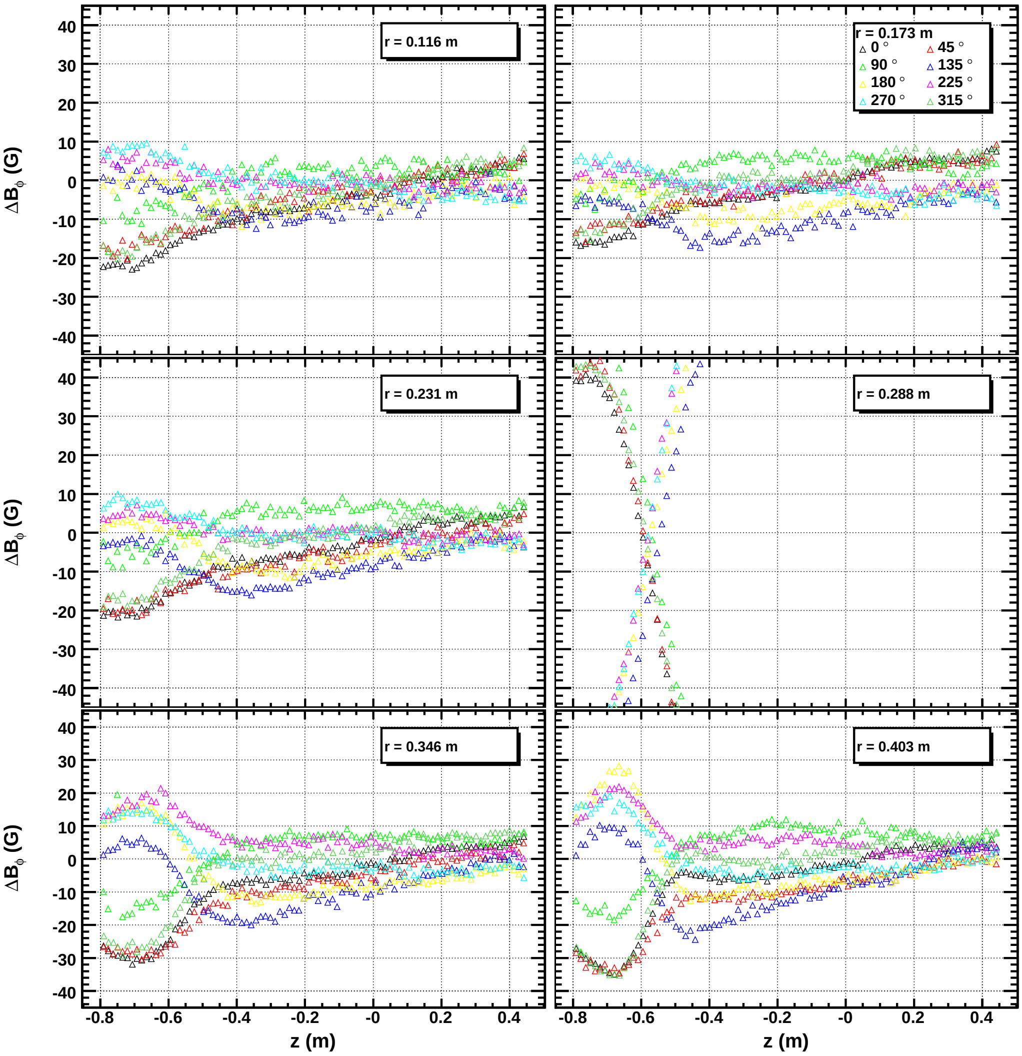

Figure D.17: Residuals for B_ϕ probes 1-6 and full coil model together with Hall sensor card rotations.

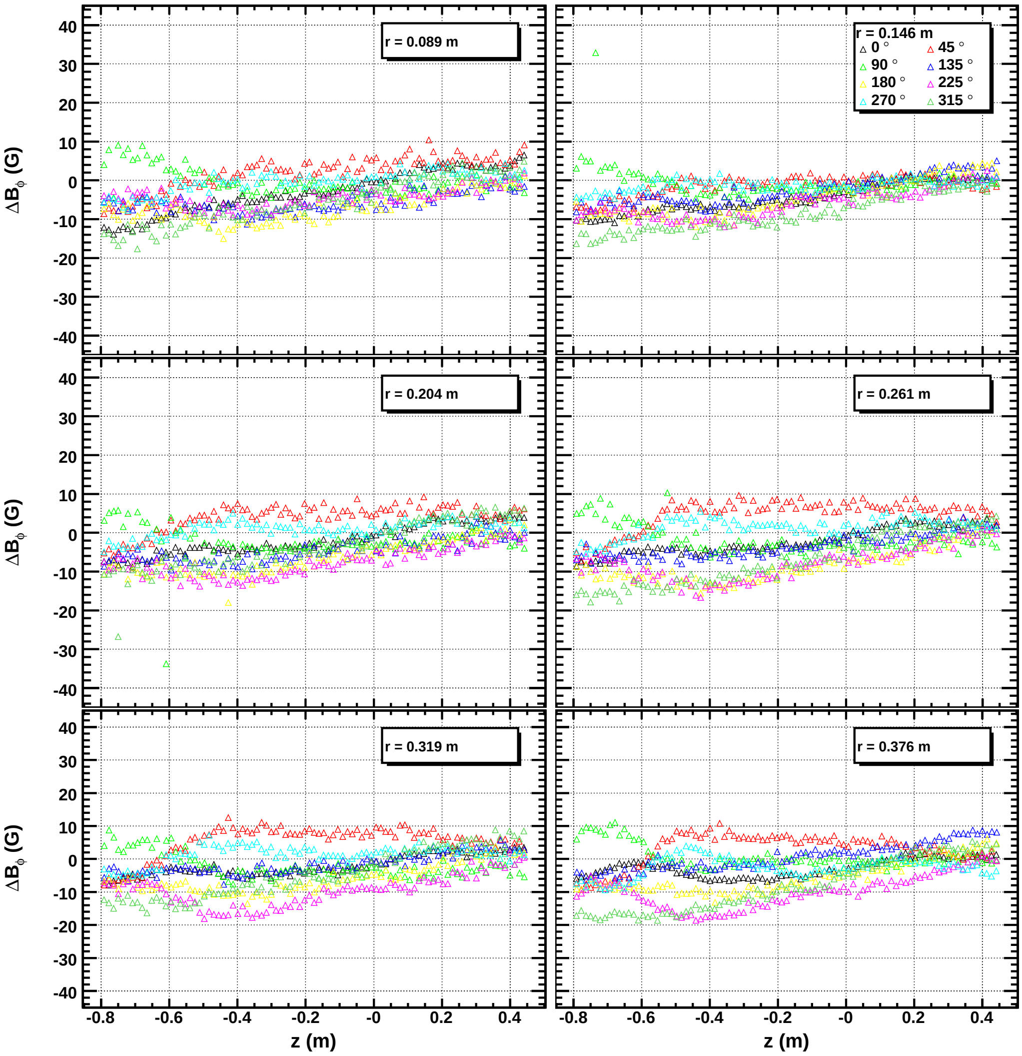

Figure D.18: Residuals for B_ϕ probes 7-12 and full coil model together with Hall sensor card rotations.

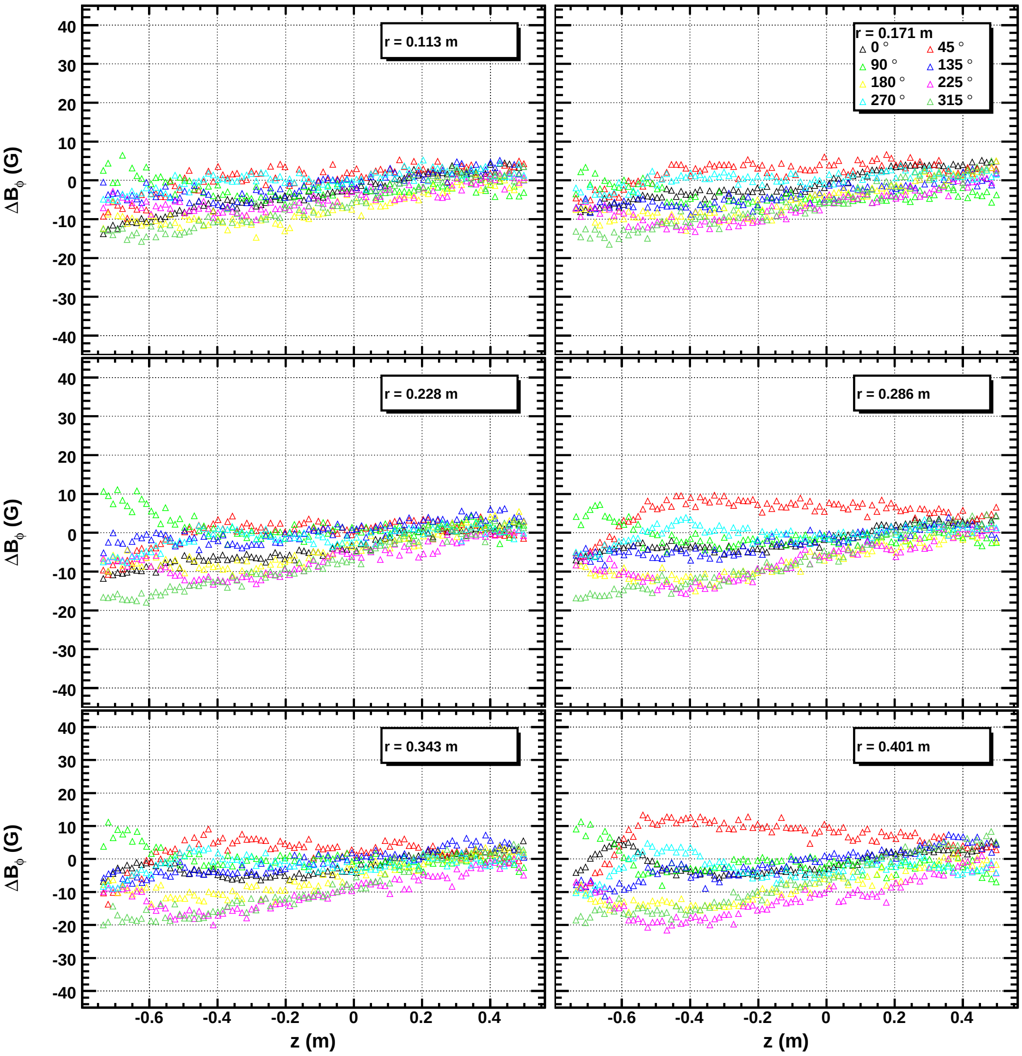

Figure D.19: Residuals for B_ϕ probes 13-18 and full coil model together with Hall sensor card rotations.

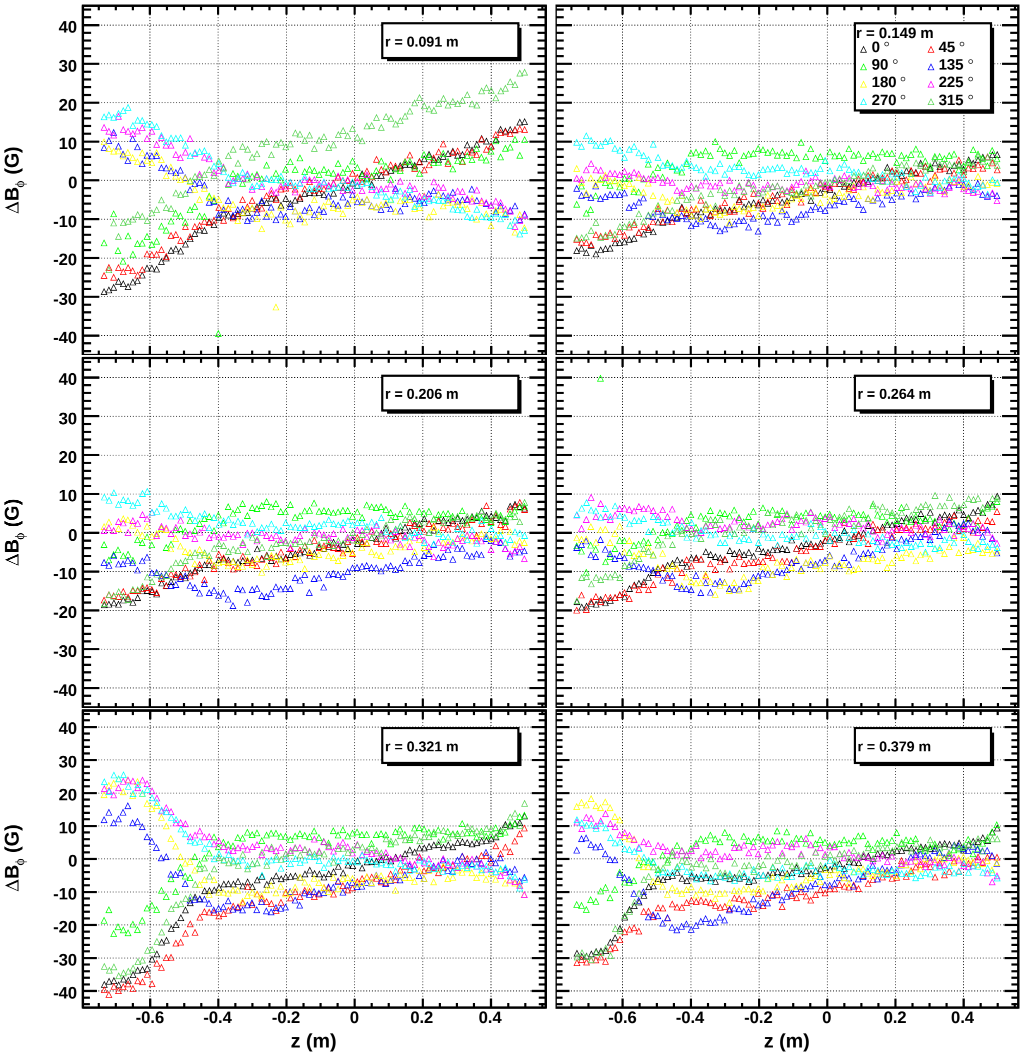

Figure D.20: Residuals for B_ϕ probes 19-24 and full coil model together with Hall sensor card rotations.

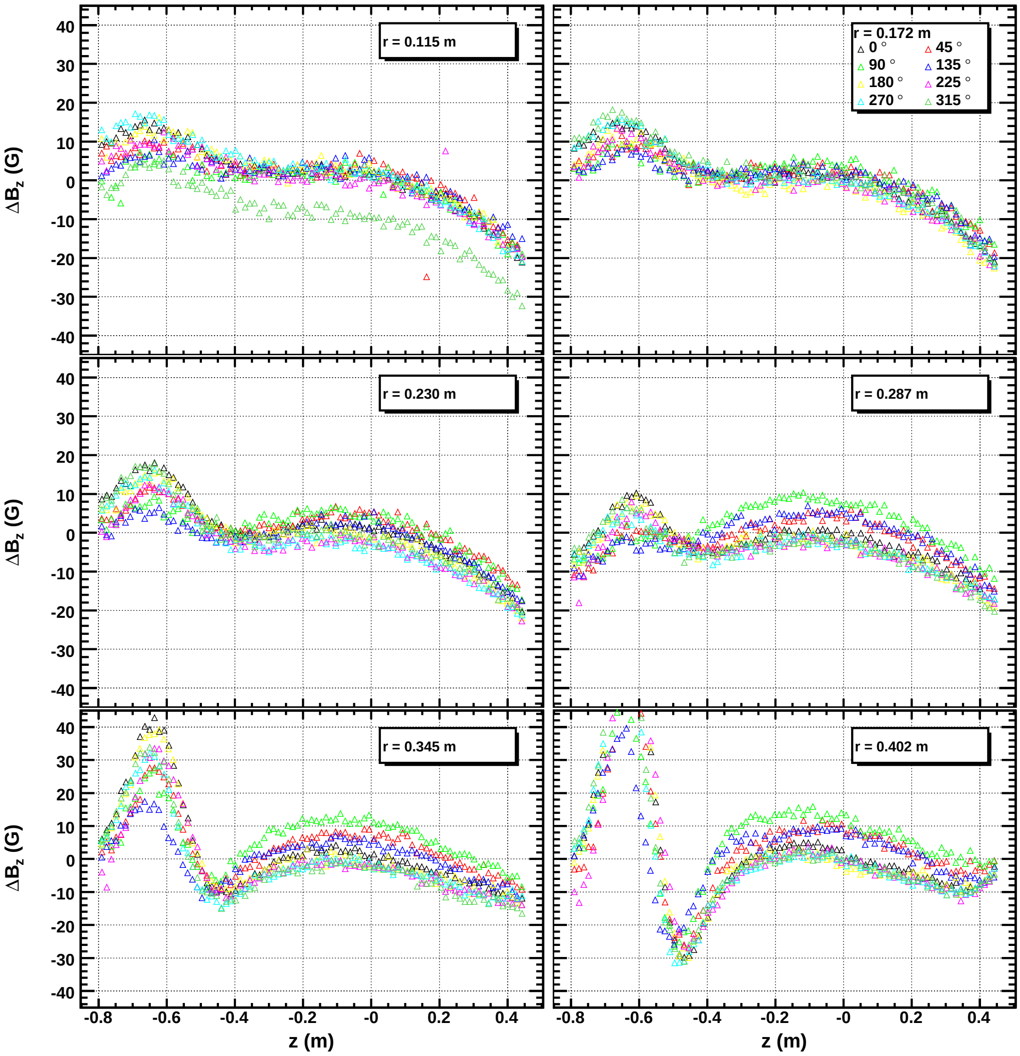

Figure D.21: Residuals for B_z probes 1-6 and full coil model together with Hall sensor card rotations.

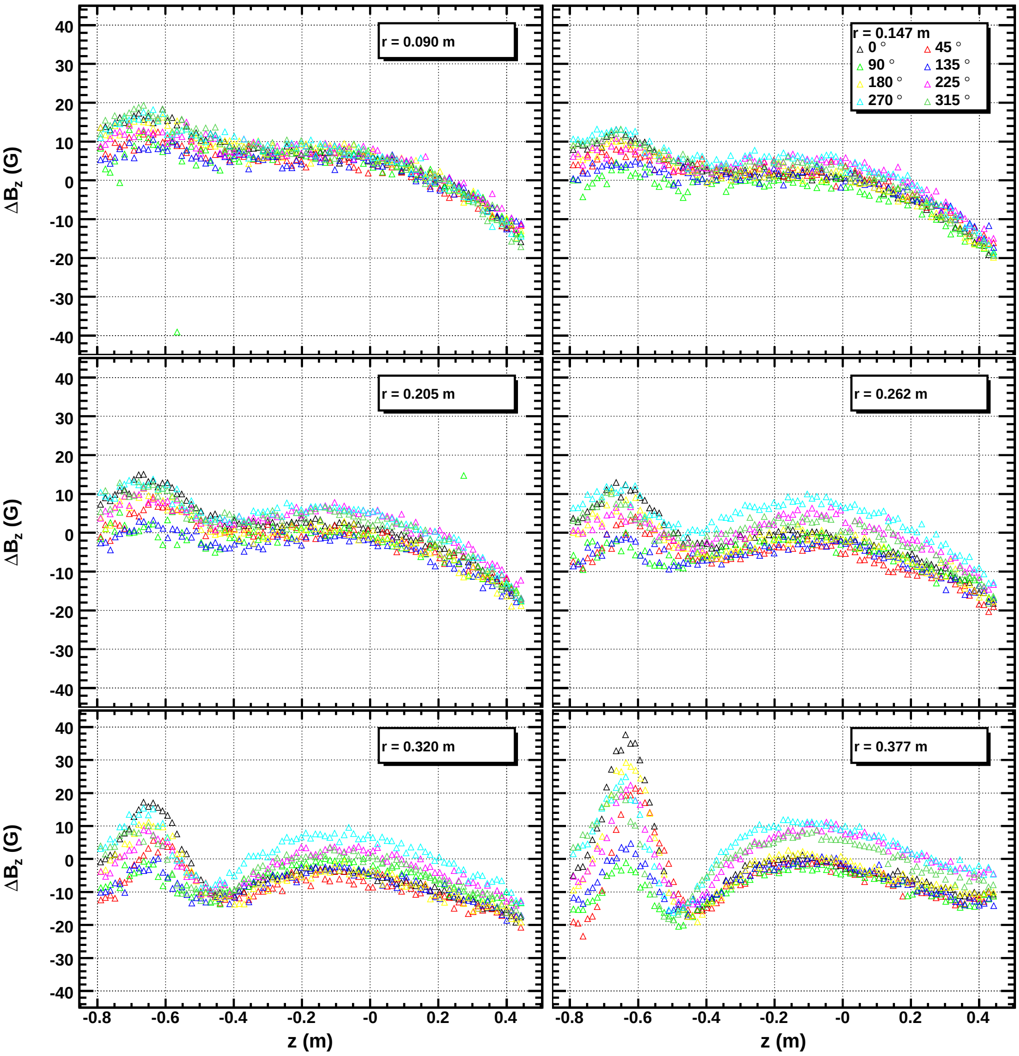

Figure D.22: Residuals for B_z probes 7-12 and full coil model together with Hall sensor card rotations.

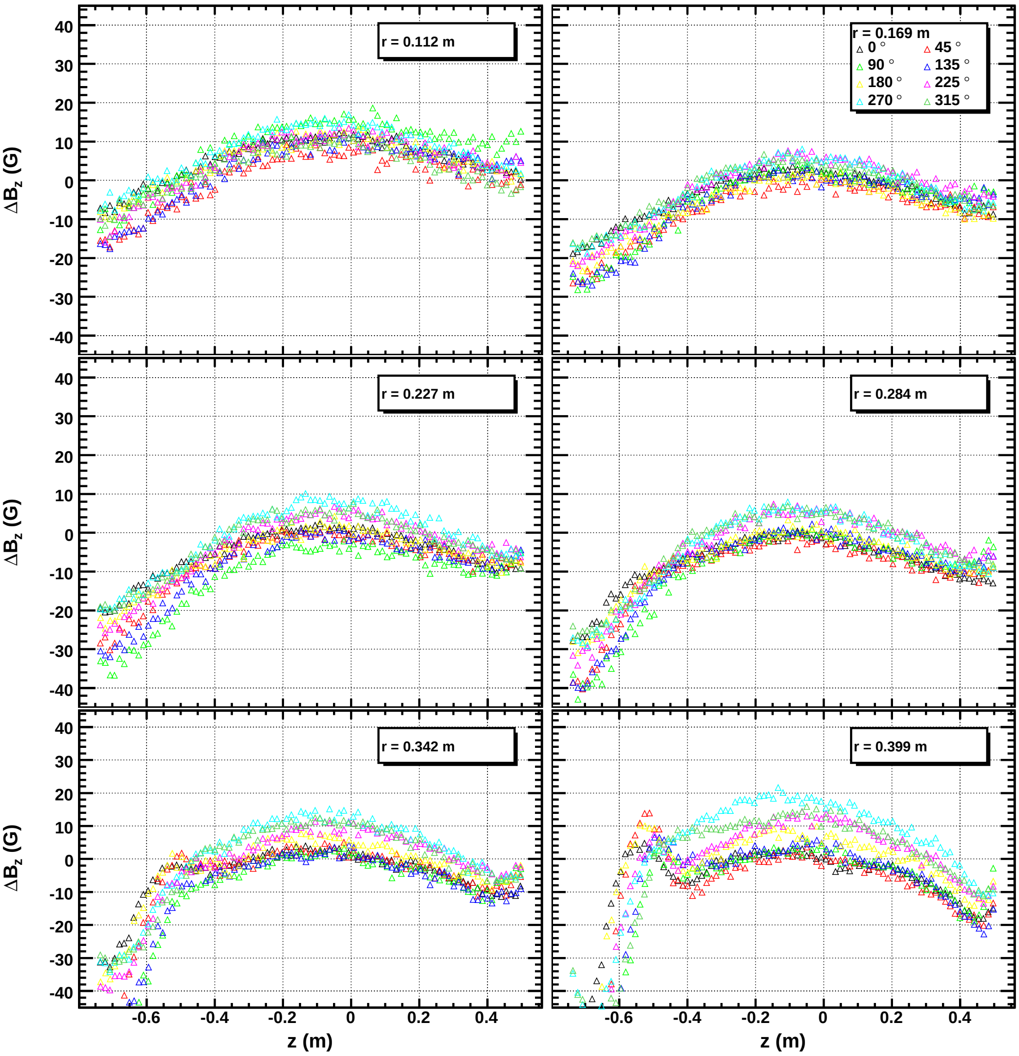

Figure D.23: Residuals for B_z probes 13-18 and full coil model together with Hall sensor card rotations.

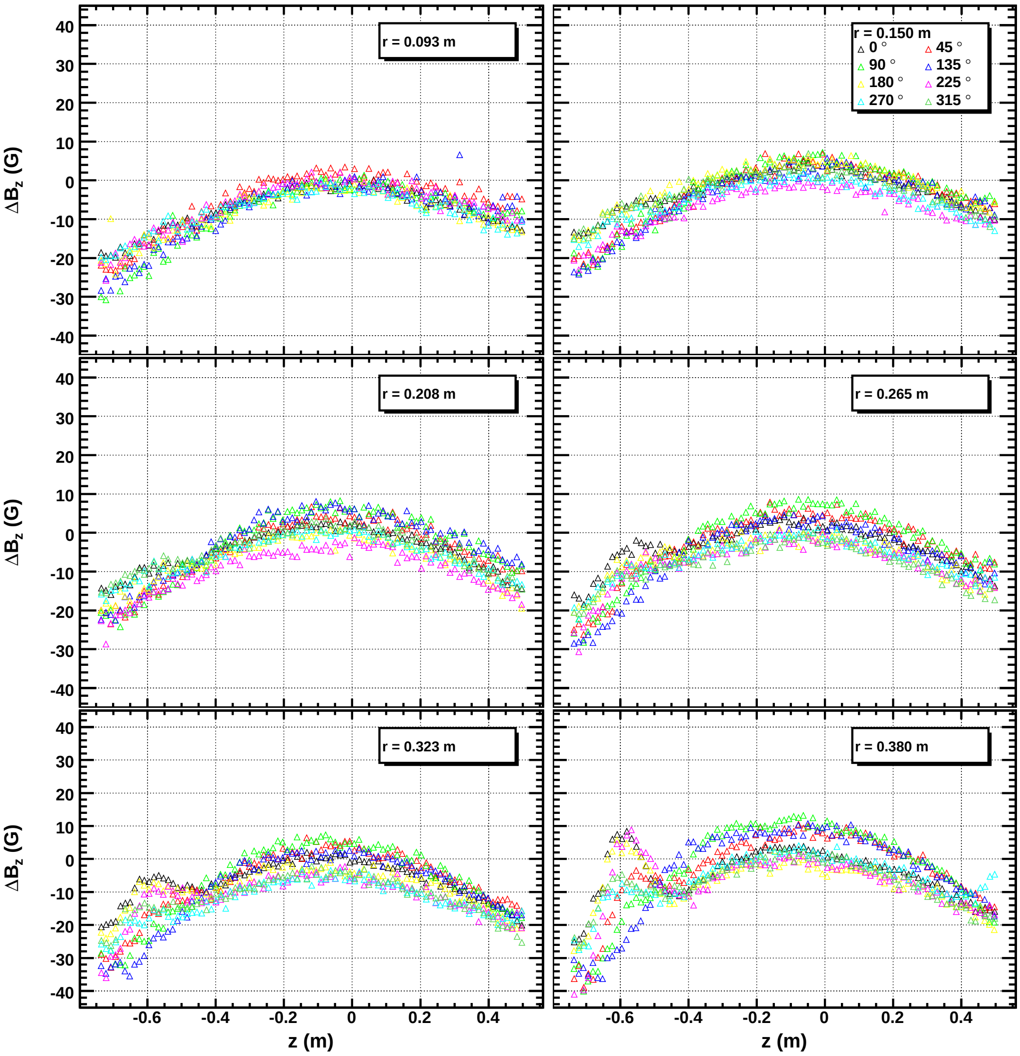

Figure D.24: Residuals for B_z probes 19-24 and full coil model together with Hall sensor card rotations.

D.3 Final Model

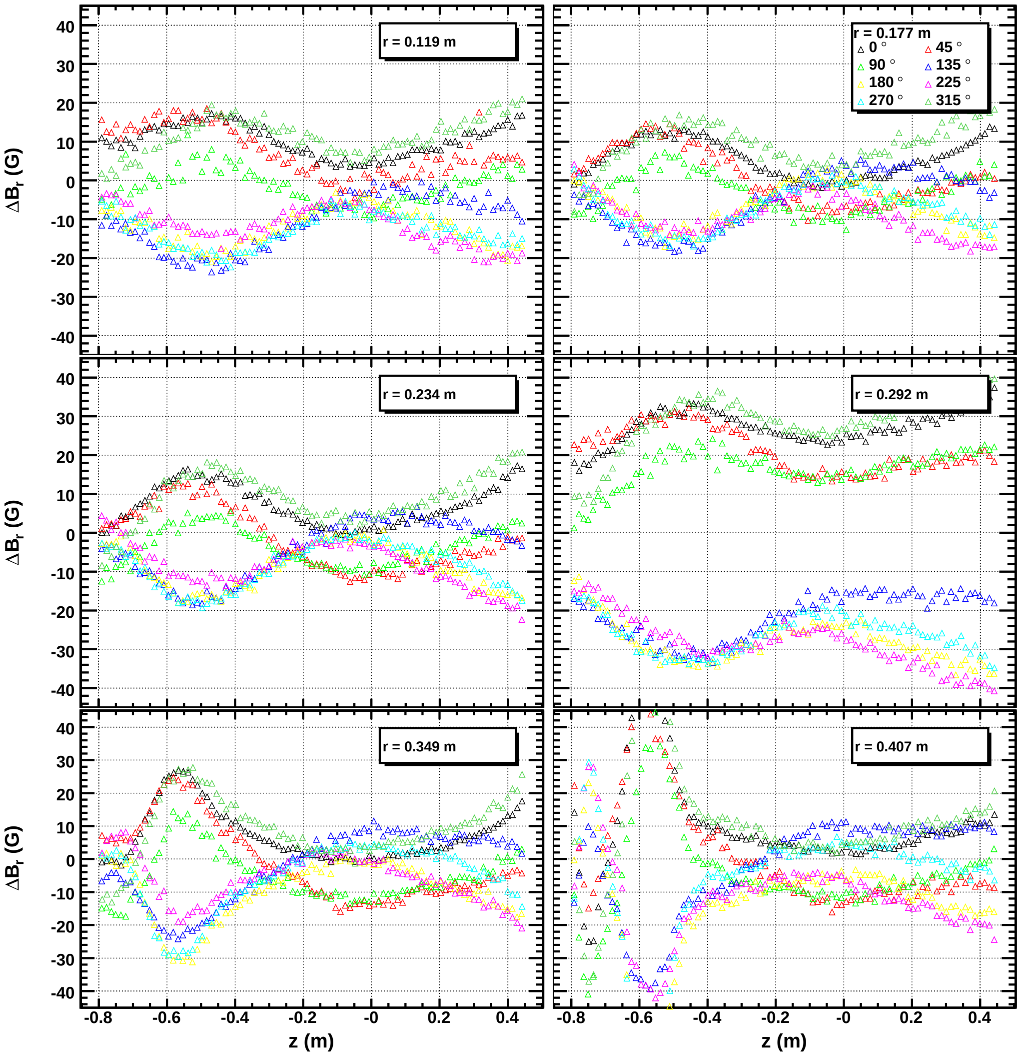

Figure D.25: Residuals for B_r probes 1-6 and final model.

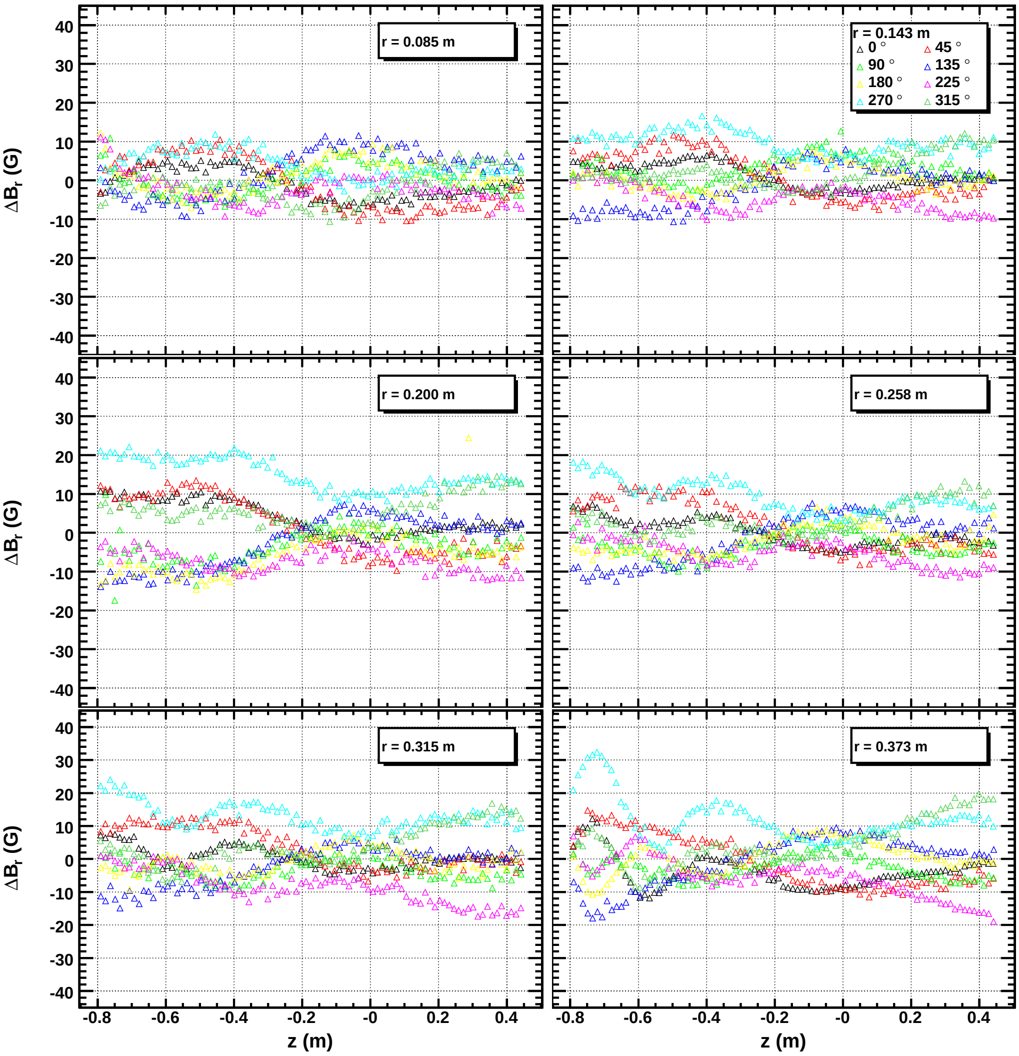

Figure D.26: Residuals for B_r probes 7-12 and final model.

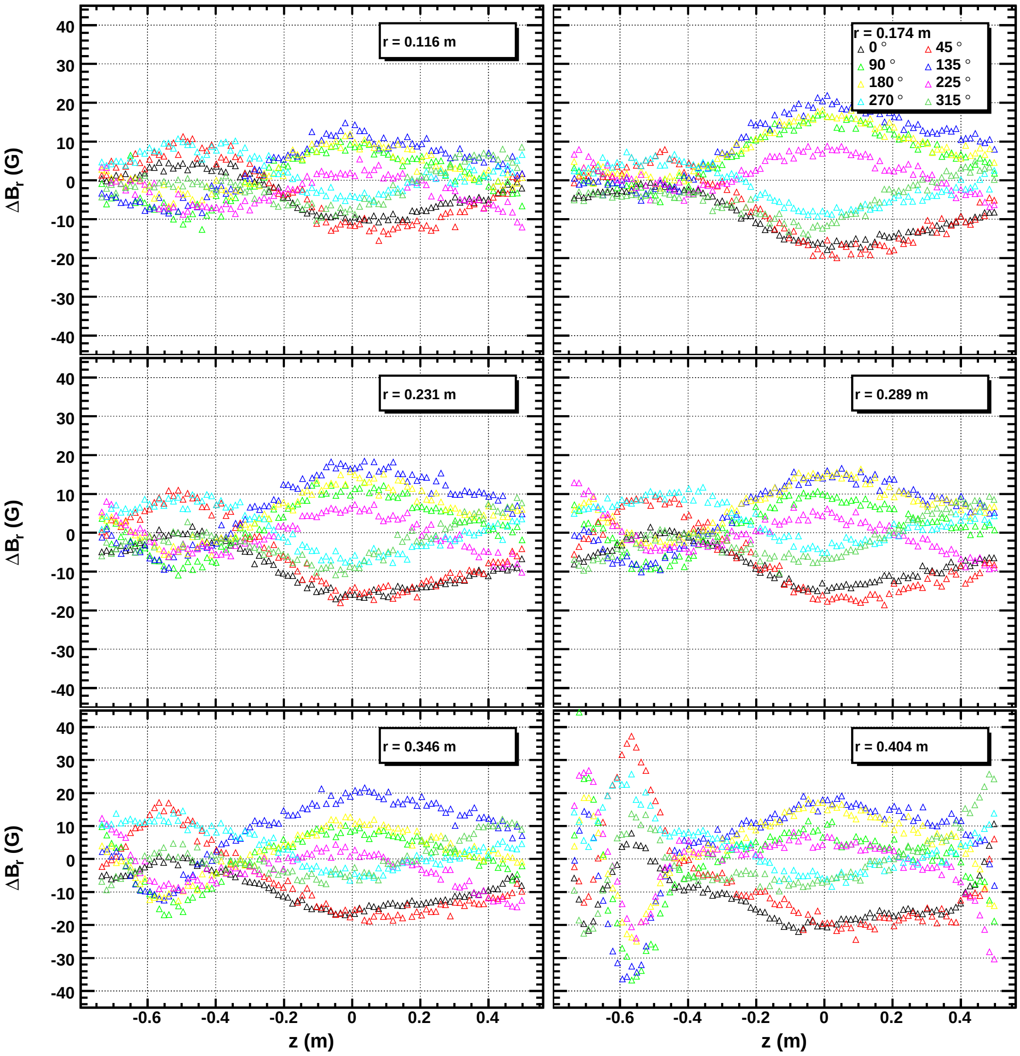

Figure D.27: Residuals for B_r probes 13-18 and final model.

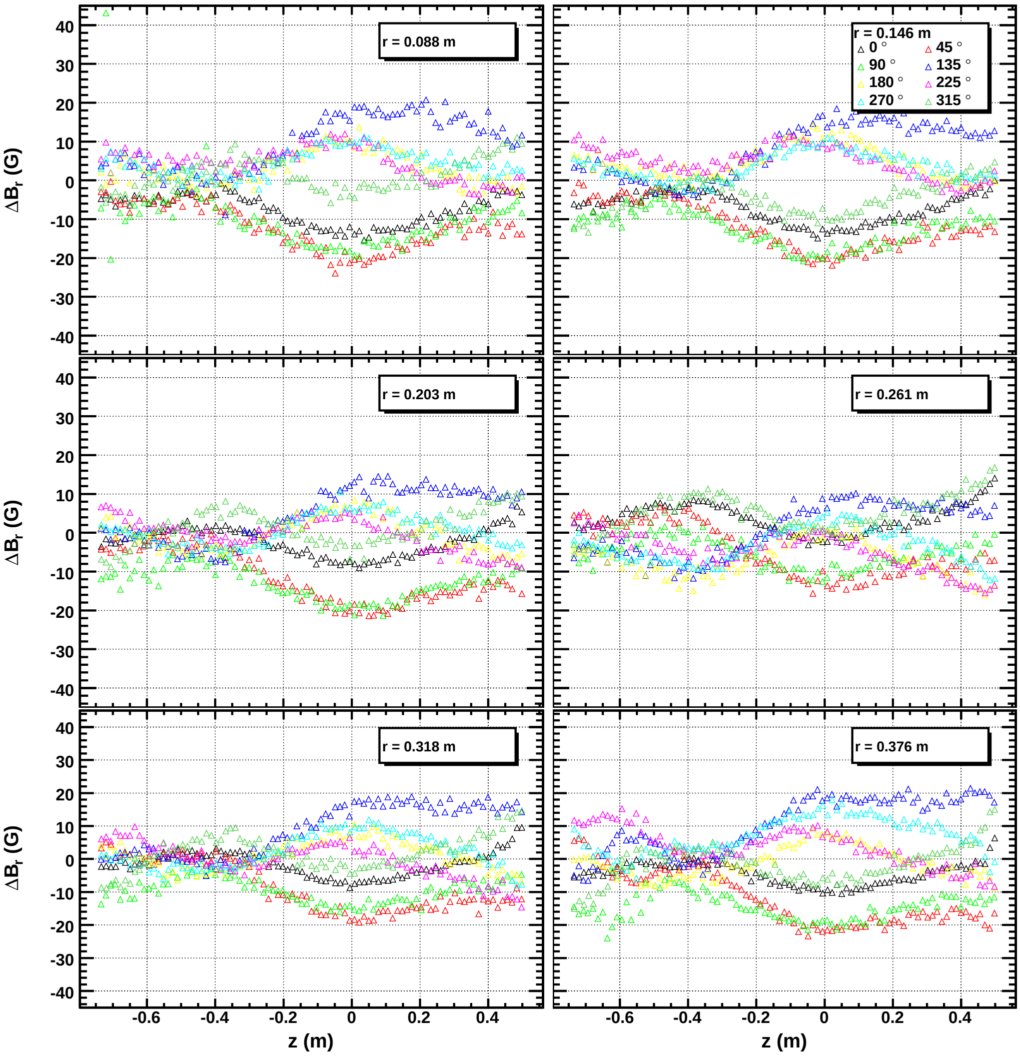

Figure D.28: Residuals for B_r probes 19-24 and final model.

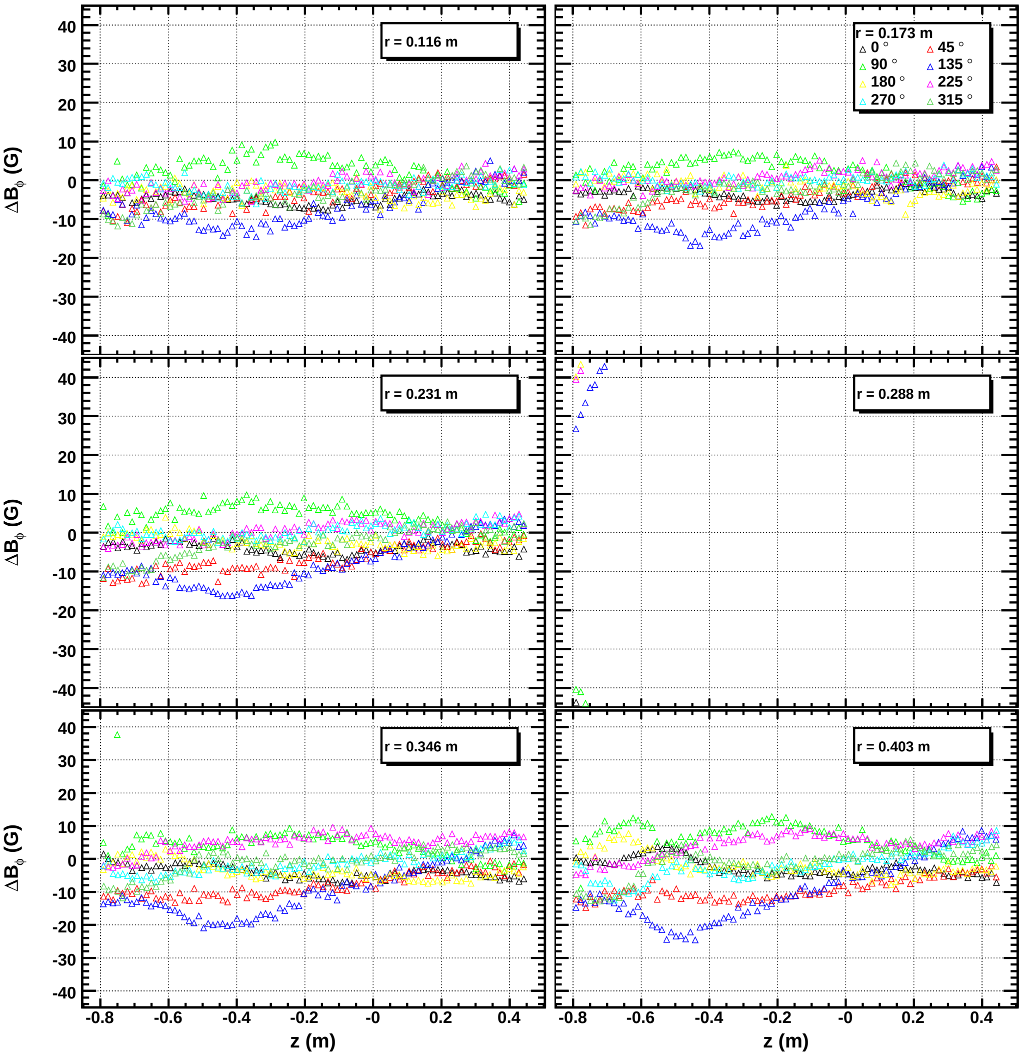

Figure D.29: Residuals for B_ϕ probes 1-6 and final model.

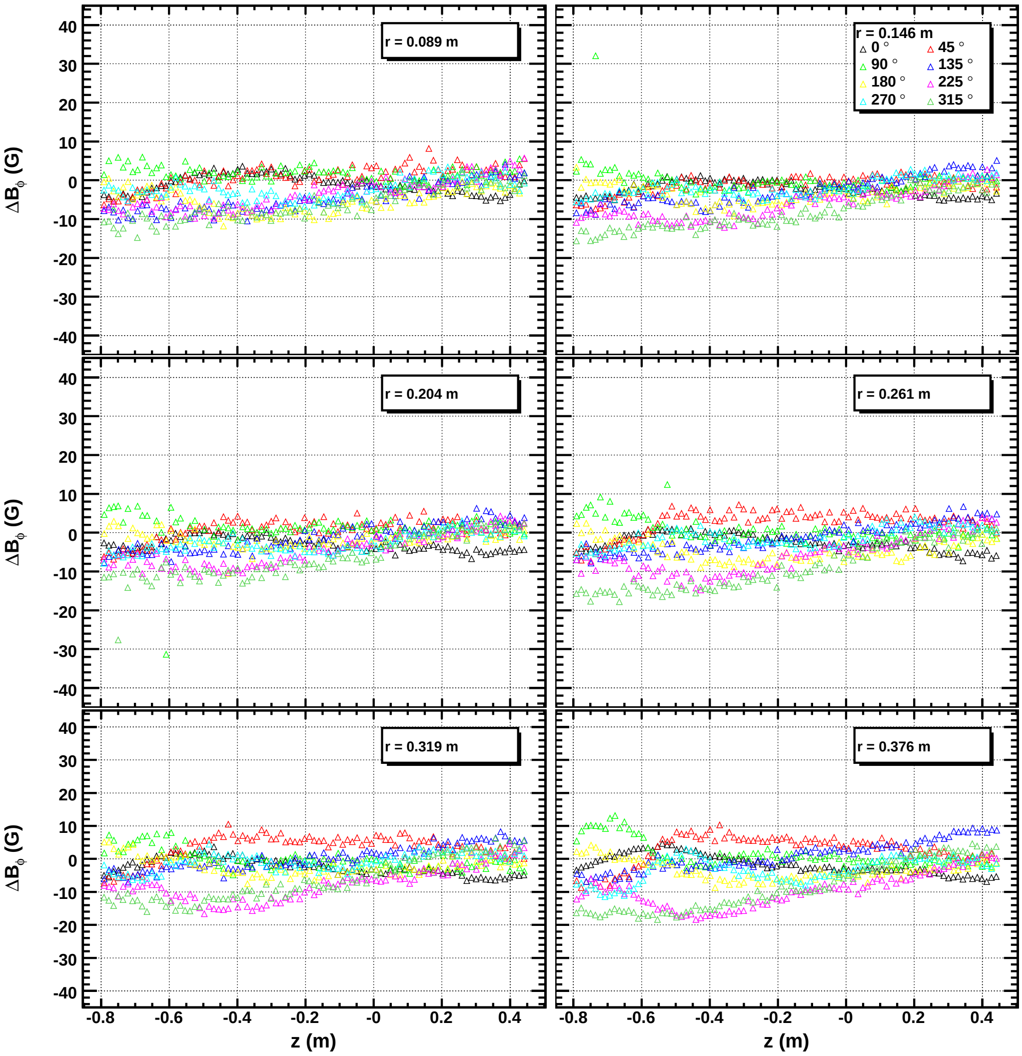

Figure D.30: Residuals for B_ϕ probes 7-12 and final model.

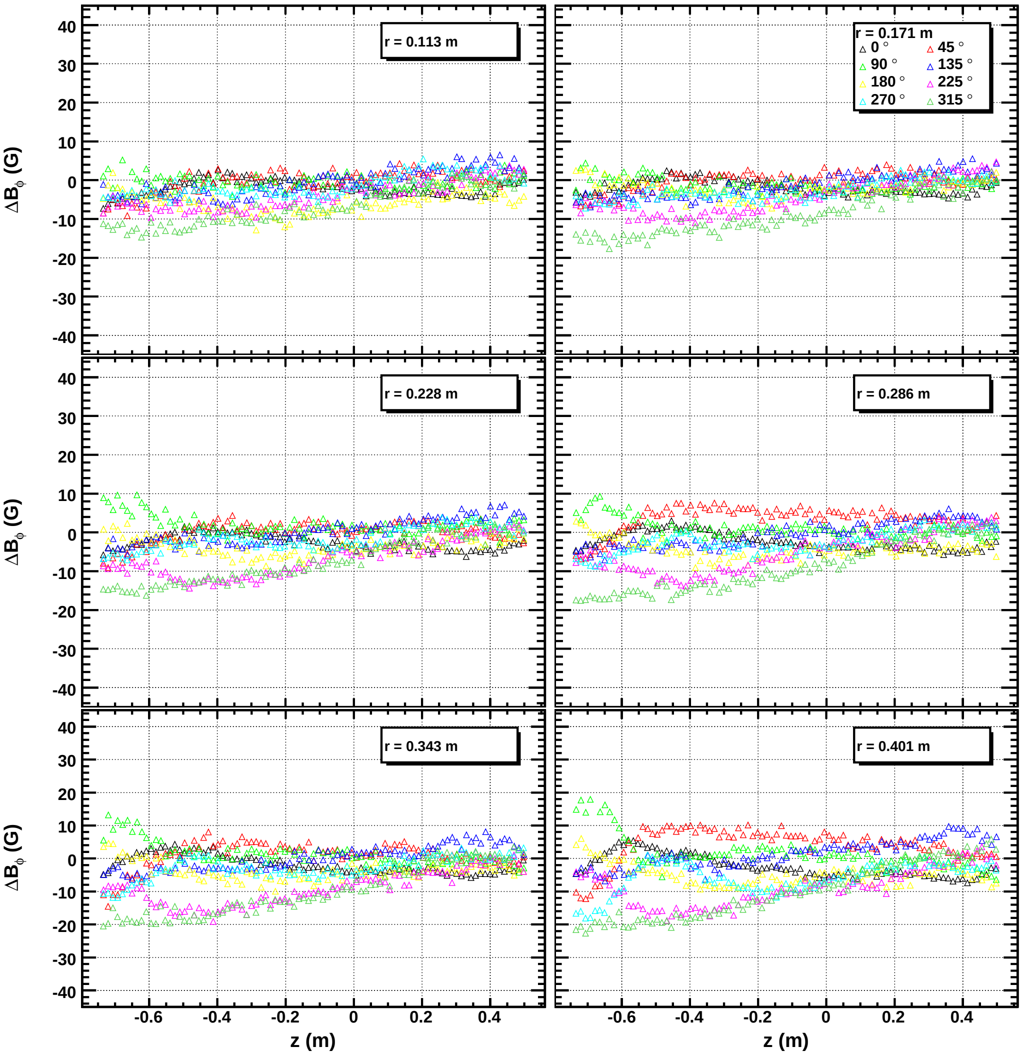

Figure D.31: Residuals for B_ϕ probes 13-18 and final model.

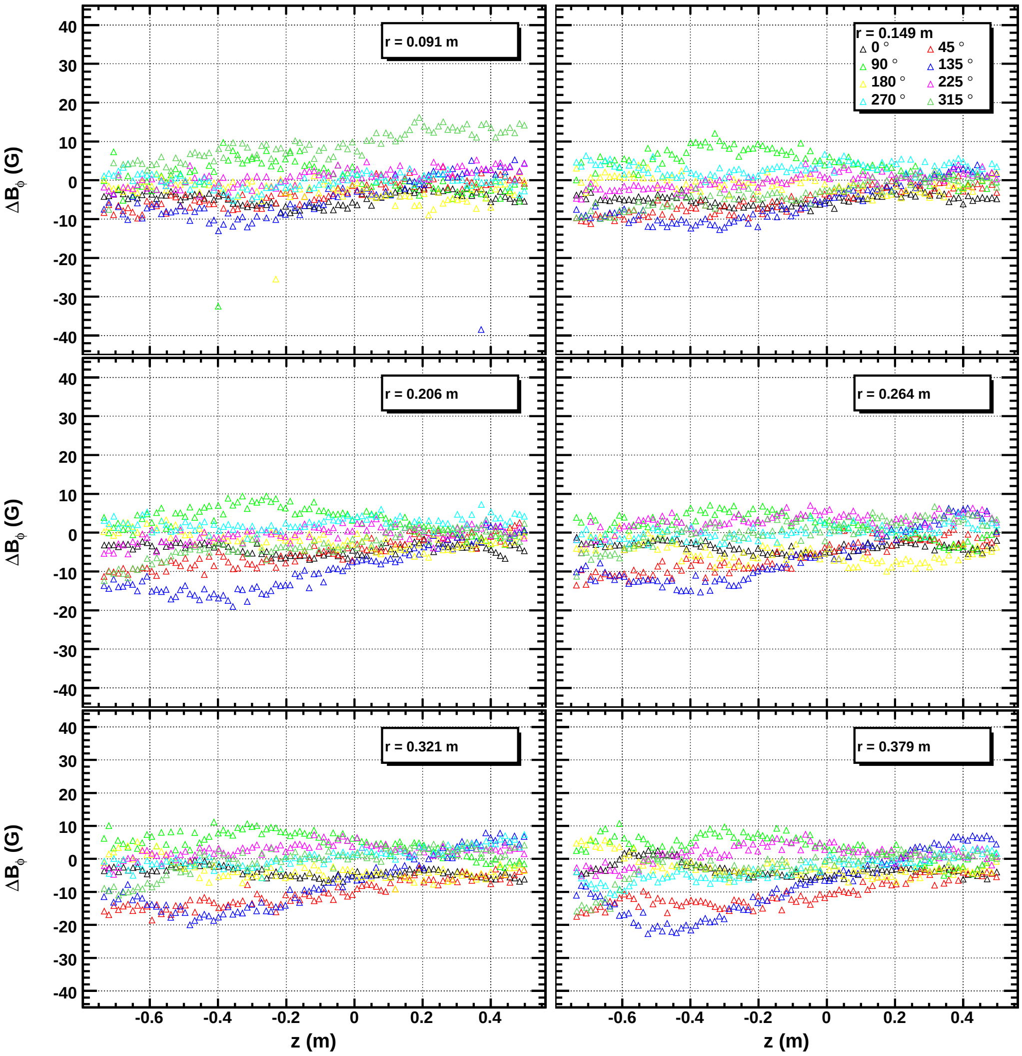

Figure D.32: Residuals for B_ϕ probes 19-24 and final model.

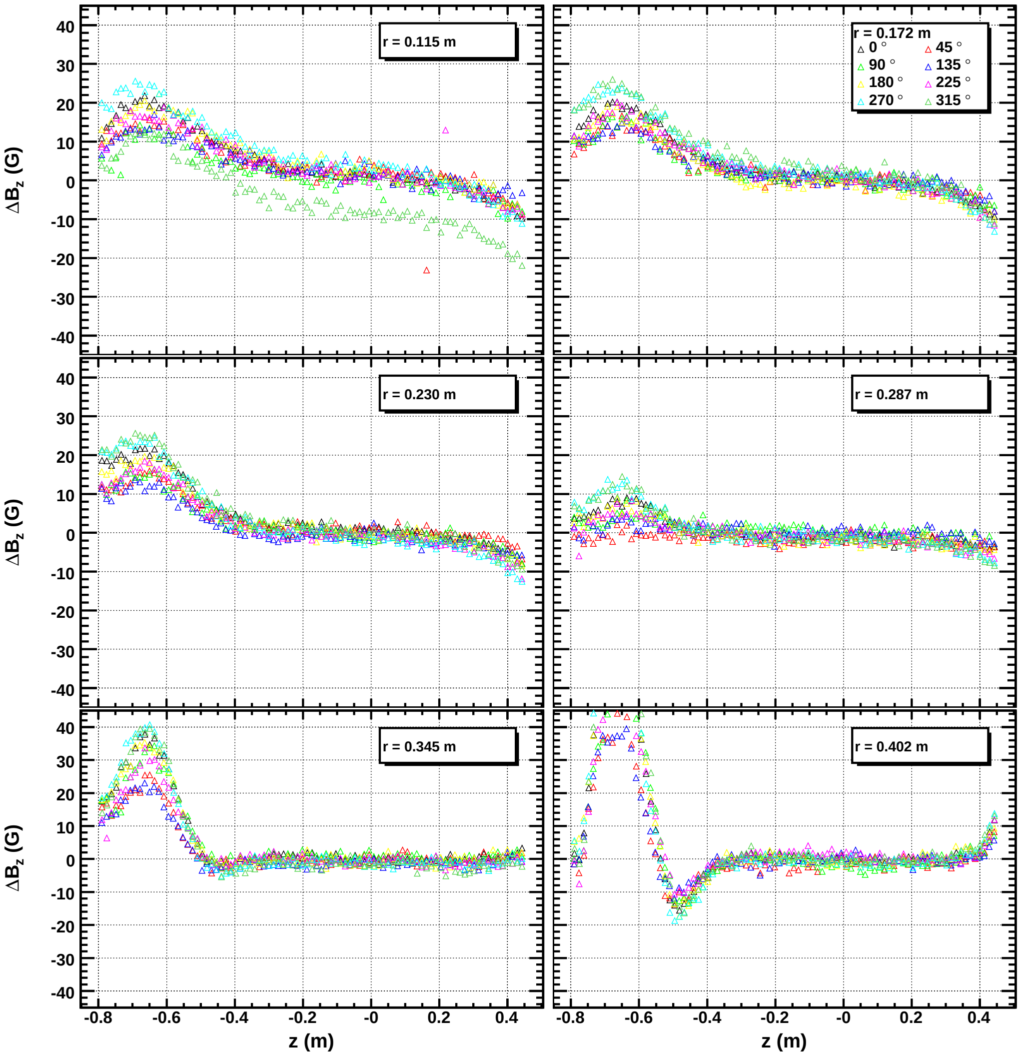

Figure D.33: Residuals for B_z probes 1-6 and final model.

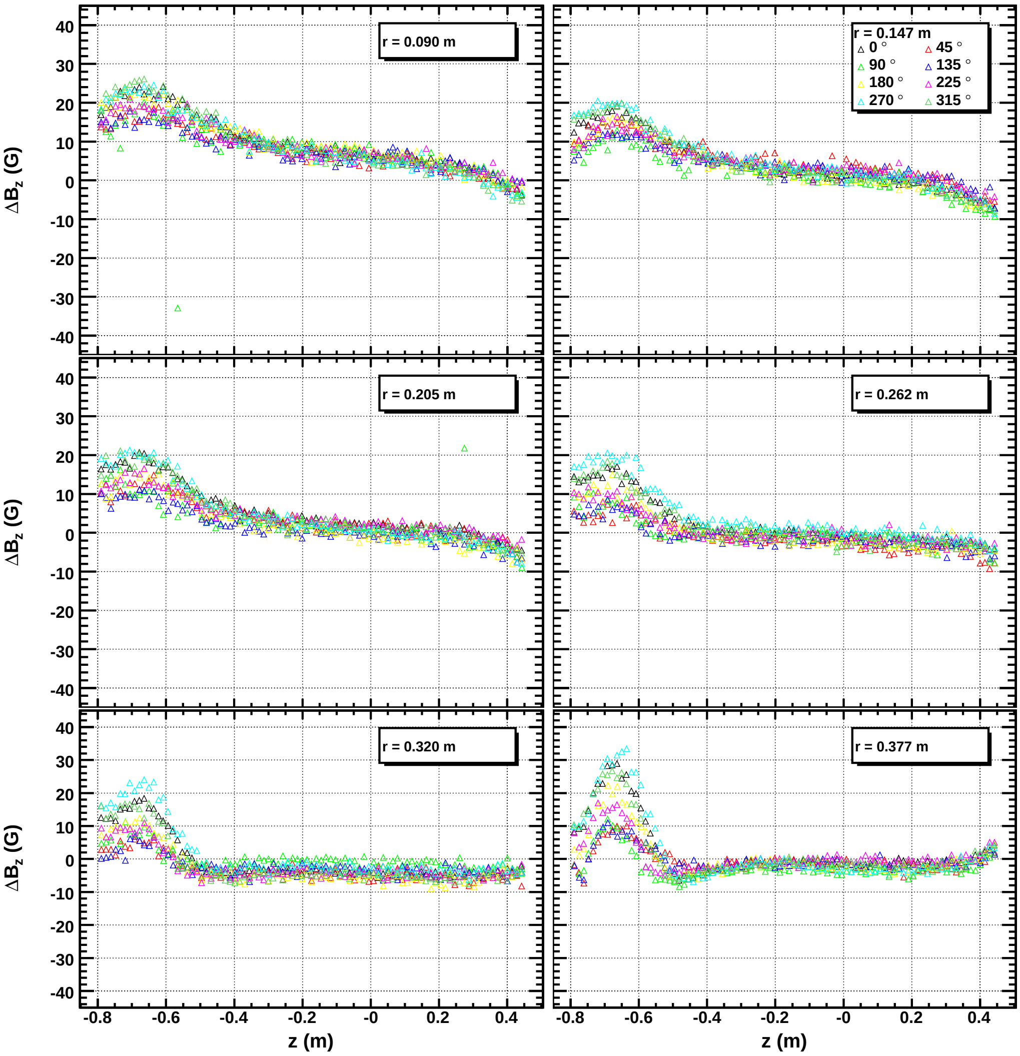

Figure D.34: Residuals for B_z probes 7-12 and final model.

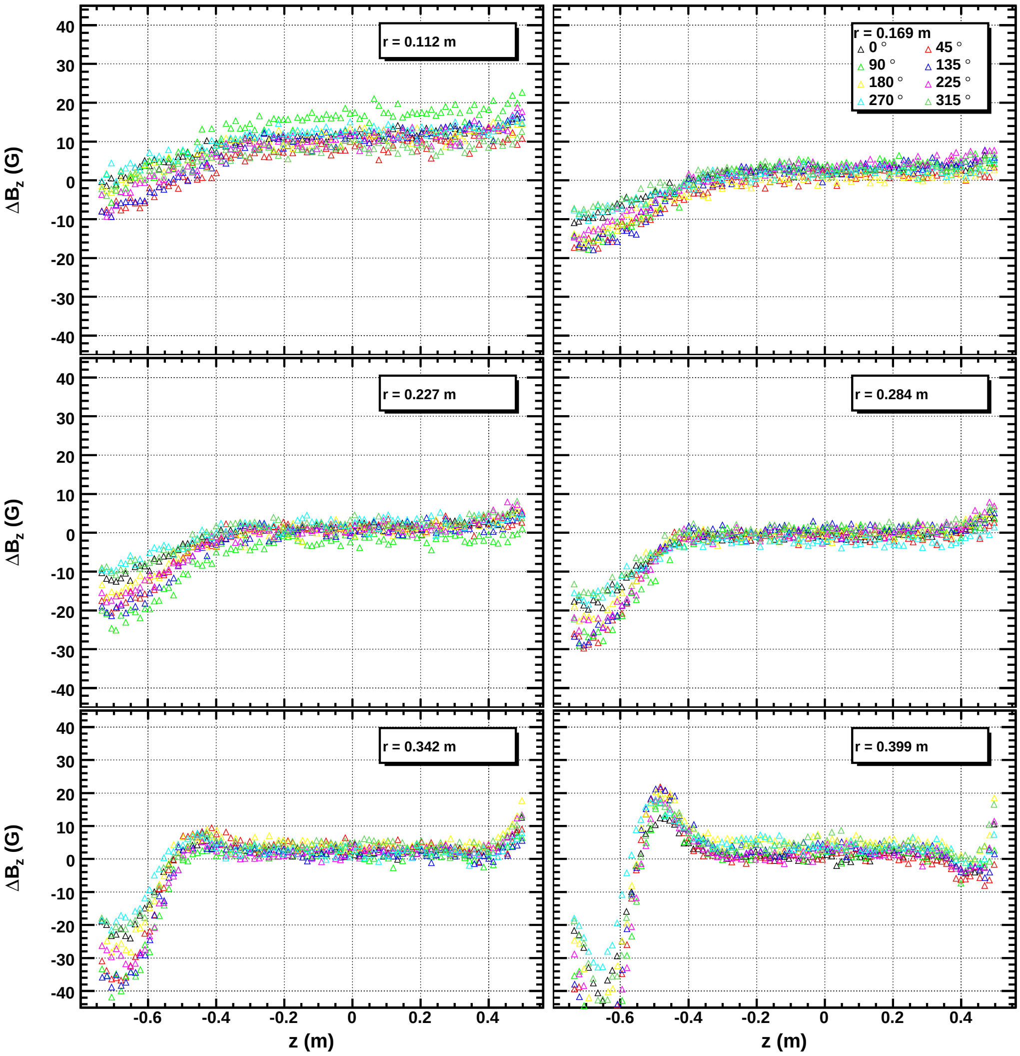

Figure D.35: Residuals for B_z probes 13-18 and final model.

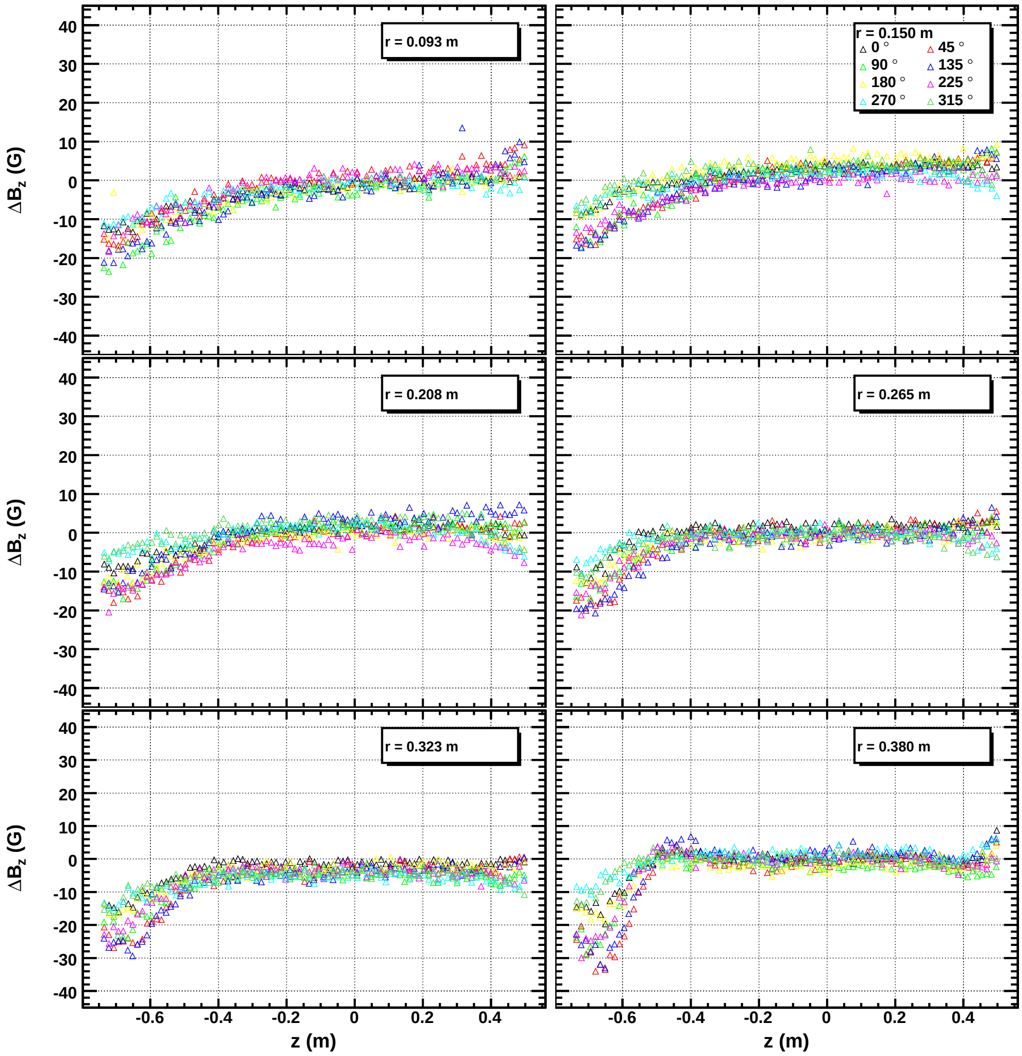

Figure D.36: Residuals for B_z probes 19-24 and final model.

Bibliography

[1] MINUIT reference manual, 1998. `http://wwwasdoc.web.cern.ch/wwwasdoc/minuit/minmain.html`.

[2] CERN-EUDET JRA1 documents page, 2008. `http://cern-eudet.web.cern.ch/cern-Eudet/JRA1-magnet.htm`.

[3] CERN Gas Detector Development group, 2008. `http://gdd.web.cern.ch/GDD/`.

[4] JACEE project page at the university of Washington. 2008. `http://marge.phys.washington.edu/jacee/`.

[5] LCCD homepage, 2008. `http://ilcsoft.desy.de/lccd/`.

[6] LCIO homepage, 2008. `http://lcio.desy.de/`.

[7] MarlinTPC homepage, 2008. `http://ilcsoft.desy.de/portal/software_packages/marlintpc`.

[8] The LEP Electroweak Working Group, 2008. `http://lepewwg.web.cern.ch/LEPEWWG/`.

[9] The Supernova Cosmology Project, 2008. `http://www-supernova.lbl.gov/`.

[10] M. Aleksa et al. Measurement of the solenoid magnetic field. ATL-MAGNET-PUB-2007-001.

[11] T. Behnke, C. Damerell, J. Jaros, and A. Miyamoto. ILC Reference Design Report, Vol. 4: Detectors, 2007.

[12] T. Behnke, R. Diener, L. Hallermann, and P. Schade. Status and Plans of the Large TPC Prototype for the ILC. EUDET-MEMO-2007-37.

[13] F. Bergsma. Progress on the 3D calibration of hall probes. 14^{th} International Magnetic Measurement Workshop, Geneva. 2005. `http://cern-eudet.web.cern.ch/cern-Eudet/JRA1/FelixIMWW14.ppt`.

[14] Gianfranco Bertone, Dan Hooper, and Joseph Silk. Particle dark matter: Evidence, candidates and constraints. *Phys. Rept.*, 405:279–390, 2005.

[15] R. Bouclier et al. The gas electron multiplier (GEM). *IEEE Trans. Nucl. Sci.*, 44:646–650, 1997.

[16] J. Brau, Y. Okada, and N. Walker. ILC Reference Design Report, Vol. 1: Executive Summary, 2007.

[17] R. Brinkmann et al. TESLA: The superconducting electron positron linear collider with an integrated X-ray laser laboratory. Technical design report. Pt. 2: The accelerator. DESY-01-011.

[18] Marcela S. Carena and Howard E. Haber. Higgs boson theory and phenomenology. *Prog. Part. Nucl. Phys.*, 50:63–152, 2003.

[19] G. Charpak, R. Bouclier, T. Bressani, J. Favier, and C. Zupancic. Some read-out systems for proportional multiwire chambers. *Nucl. Instrum. Meth.*, 65:217–220, 1968.

[20] A. Djouadi, J. Lykken, K. Mönig, Y. Okada, M. Oreglia, and S. Yamashita. ILC Reference Design Report, Vol. 2: Physics at the ILC, 2007.

[21] Y. Giomataris, P. Rebourgeard, J. P. Robert, and Georges Charpak. MICROMEGAS: A high-granularity position-sensitive gaseous detector for high particle-flux environments. *Nucl. Instrum. Meth.*, A376:29–35, 1996.

[22] J. C. Hart. Corrections to the solenoid field measurements. ATL-MAGNET-PUB-2007-002.

[23] J. D. Jackson. *Classical Electrodynamics.* John Wiley & Sons, 3^{rd} edition, 1998.

[24] D. I. Kazakov. Beyond the standard model (in search of supersymmetry). 2000.

[25] X. Llopart, R. Ballabriga, M. Campbell, L. Tlustos, and W. Wong. Timepix, a 65k programmable pixel readout chip for arrival time, energy and/or photon counting measurements. *Nuclear Instruments and Methods in Physics Research A*, 581:485–494, October 2007.

[26] E. Lohrmann. *Hochenergiephysik.* Teubner Studienbücher, 5^{th} edition, 2005.

[27] Stephen P. Martin. A supersymmetry primer. 1997.

[28] N. Phinney, N. Toge, and N. Walker. ILC Reference Design Report, Vol. 3: Accelerator, 2007.

[29] P. Schmüser. *Feynman-Graphen und Eichtheorien für Experimentalphysiker.* Springer, 2^{nd} edition, 1995.

[30] D. N. Spergel et al. Wilkinson Microwave Anisotropy Probe (WMAP) three year results: Implications for cosmology. *Astrophys. J. Suppl.*, 170:377, 2007.

[31] S. A. Thorn. An Attempt to Model the ALEPH Magnetic Field. ALEPH 94-162.

[32] W.-M. Yao et al. Review of Particle Physics. *Journal of Physics G*, 33:1+, 2006.

Acknowledgements

Finally i would like to express my gratitude to the numerous people who made this diploma thesis possible.

First of all, I want to thank Dr. Thies Behnke for giving me the opportunity of preparing this thesis in the FLC working group at DESY. Furthermore, I want to thank him for the opportunity to attend the annual EUDET meeting 2007 in Paris and the DPG spring meeting 2008 in Freiburg. I also want to thank JProf. Dr. Johannes Haller for taking over the part of the referee.

I want to thank the whole FLC working group at DESY for the great atmosphere, it was fun and a pleasure to work there. In particular, I want to thank Dr. Klaus Dehmelt for being my supervisor and for introducing me to the thesis with many valuable discussions. I also want to thank my office mate Dipl.-phys. Adrian Vogel for helping me out with numerous computer and programming problems and for some marvelous *Nussecken*.

Especially, I want to thank Dr. Lucie Linssen for giving me the opportunity of spending four month of this thesis at CERN and for being such a great supervisor during that time and also for introducing me to the world of skiing. I also want to thank Dr. Michael Hauschild for giving me a warm welcome at CERN and for a lot of helpfull discussions on the thesis.

I want to thank the team from CERN which prepared and carried out the magnetic field measurements, namely Dr. Felix Bergsma, Pierre-Ange Giudici, Dr. Antoine Kehrli and Dr. Marcello Losasso.

A special thanks goes to all my friends for the great times we have spent and we will hopefully spend in the future: Annika Dick, Fabian Gerwien, Carolin Hamann, Oliver Patz, Sascha Siedenburg, Henning Stein and all the others.

And last but definately not least I want to thank my parents and my brother Michael for all their support and for just being there.

Erklärung

Hiermit versichere ich, die vorliegende Arbeit selbständig und nur unter Verwendung der angegebenen Quellen und Hilfsmittel verfasst zu haben. Ich gestatte die Veröffentlichung dieser Arbeit.